

**Carnegie Mellon University**  
CARNEGIE INSTITUTE OF TECHNOLOGY

**THESIS**

SUBMITTED IN PARTIAL FULFILLMENT OF THE REQUIREMENTS

FOR THE DEGREE OF Doctor of Philosophy

**TITLE**      Predicting Phonon Properties and Thermal Conductivity Using  
Anharmonic Lattice Dynamics Calculations

**PRESENTED BY** Joseph E. Turney

**ACCEPTED BY THE DEPARTMENT OF**  
Mechanical Engineering

\_\_\_\_\_  
ADVISOR, MAJOR PROFESSOR      \_\_\_\_\_  
DATE

\_\_\_\_\_  
DEPARTMENT HEAD      \_\_\_\_\_  
DATE

**APPROVED BY THE COLLEGE COUNCIL**  
  
\_\_\_\_\_  
DEAN      \_\_\_\_\_  
DATE

# **Predicting Phonon Properties and Thermal Conductivity Using Anharmonic Lattice Dynamics Calculations**

Submitted in partial fulfillment of the requirements for

the degree of

Doctor of Philosophy

in

Mechanical Engineering

Joseph E. Turney

B.S., Mechanical Engineering, Youngstown State University

M.S., Mechanical Engineering, Carnegie Mellon University

Carnegie Mellon University  
Pittsburgh, Pennsylvania

December 2009



© Joseph E. Turney 2009  
All Rights Reserved



## ACKNOWLEDGEMENTS

I have spent more than four years as a graduate student at Carnegie Mellon University. The experience has been both rewarding and enjoyable, for which I am grateful to a number of people. In particular, I would like to thank my advisors Dr. Cristina Amon (committee chair) and Dr. Alan McGaughey for their guidance and support. Thanks also to Dr. Shi-Chune Yao and Dr. Kenneth Jordan for serving on my thesis committee and for their thoughtful comments, suggestions, and encouragement.

I would like to thank the members of the Nanoscale Transport Phenomena Laboratory for their input and camaraderie. Eric Landry and John Thomas deserve special thanks due to the many conversations we have had that have influenced my research and their willingness to setup and run molecular dynamics simulations to support my work.

The person who has had the largest impact on my life these past several years is my wife, Jackie. Jackie has been my constant companion since our undergraduate studies at Youngstown State University. I am grateful to my wife along with my parents and the rest of my family for their endless love and support.

Financial support for this work, provided by the Pennsylvania Infrastructure Technology Alliance, a partnership of Carnegie Mellon, Lehigh University, and the Commonwealth of Pennsylvania's Department of Community and Economic Development and Advanced Micro Devices is greatly appreciated.



## ABSTRACT

### Predicting Phonon Properties and Thermal Conductivity Using Anharmonic Lattice Dynamics Calculations

by

Joseph E. Turney

The ability to engineer materials on the nanoscale has given rise to the possibility of tailoring material properties such as the thermal conductivity. The alteration of the thermal properties is due to the interaction between the phonons and the geometry of these nano-structures. Phonons (*i.e.*, lattice vibrations) are the primary energy carriers in insulating crystals, such as argon, silicon, and germanium. A fundamental understanding of the physics of phonon transport in such nano-structured materials and a means of computing their thermal conductivity are required to efficiently design these materials. Current techniques used to examine the lattice thermal conductivity of crystals use major approximations or are computationally intensive.

One technique that can be used to perform an accurate analysis of lattice thermal conductivity is the anharmonic lattice dynamics method. Anharmonic lattice dynamics is the natural extension of harmonic lattice dynamics, which can be used to calculate phonon frequencies. Anharmonic lattice dynamics provides detailed information about the phonon modes, such as frequencies, group velocities, and scattering rates, that is not typically found through other methods. Thus, it is an ideal method



to use when predicting the thermal conductivity as the properties of the phonon modes provide additional insight into the physics of thermal transport.

In this work, the anharmonic lattice dynamics method is presented and the challenges associated with implementing the method are addressed. The methodology is used to predict the thermal conductivity of crystalline argon in bulk. These predictions are validated with results from molecular dynamics simulations. The phonon properties predicted by the lattice dynamics method are used to show that some common assumptions and approximations about phonon transport are not true for all materials.

The lattice dynamics calculations are then used to study thermal transport in nanostructures. The boundaries and interfaces in thin films and superlattices present a modeling challenge. For thin films, a mode-dependent boundary scattering relation is derived and used to predict the in-plane thermal conductivity of argon and silicon thin films. For short period, ideal superlattices it is shown that the interfaces do not act as scattering sites but do affect the phonon population. The unique phonon properties in graphene and carbon nanotubes are predicted with lattice dynamics and compared to molecular dynamics predictions.

Finally, the unique abilities of the lattice dynamics techniques are used to assess the validity of quantum correcting classically-predicted thermal conductivities, such as those determined by molecular dynamics simulation. A direct assessment of the commonly used quantum corrections is made by self-consistently predicting the thermal conductivity for a quantum system and for the same system in the classical limit. These quantum corrections are shown to be inaccurate and the phonon properties are used to show that only methods that include the proper quantum phonon distribution

in the prediction of the relaxation times can be used to predict a quantum thermal conductivity.

# TABLE OF CONTENTS

<b>ACKNOWLEDGEMENTS</b> . . . . .	<b>v</b>
<b>ABSTRACT</b> . . . . .	<b>vii</b>
<b>LIST OF TABLES</b> . . . . .	<b>xii</b>
<b>LIST OF FIGURES</b> . . . . .	<b>xiii</b>
<b>NOMENCLATURE</b> . . . . .	<b>xvi</b>
<b>CHAPTERS</b>	
<b>I. Introduction</b> . . . . .	<b>1</b>
1.1 Motivation . . . . .	1
1.2 Thermal conductivity at the carrier level . . . . .	3
1.3 Objectives and scope . . . . .	5
<b>II. Phonon transport models: Theory and practice</b> . . . . .	<b>7</b>
2.1 The Boltzmann transport equation . . . . .	7
2.2 Semi-empirical models . . . . .	11
2.3 Lattice dynamics calculation . . . . .	14
2.3.1 Harmonic lattice dynamics . . . . .	14
2.3.2 Anharmonic lattice dynamics . . . . .	17
2.4 Molecular dynamics simulation . . . . .	24
2.4.1 Overview . . . . .	24
2.4.2 Normal mode analysis . . . . .	26
2.4.3 Spectral energy density . . . . .	26
2.4.4 Direct method . . . . .	27
2.4.5 Green-Kubo method . . . . .	29
<b>III. Comparison of atomic level models: Phonon transport in bulk materials</b> .	<b>31</b>
3.1 Preliminaries . . . . .	31
3.2 Comparison and validation of the Boltzmann transport equation-based methods	34
3.3 Thermal conductivity predictions . . . . .	38
3.4 Mode-dependent thermal conductivity . . . . .	41
3.5 Conclusions . . . . .	43
<b>IV. Extending lattice dynamics to finite/heterogeneous structures: Thin films and superlattices</b> . . . . .	<b>46</b>
4.1 Introduction . . . . .	46

4.2	In-plane phonon transport in thin films . . . . .	48
4.2.1	Computational framework . . . . .	48
4.2.2	Atomic structure at the boundaries . . . . .	52
4.2.3	Results . . . . .	56
4.2.4	Insights from phonon properties . . . . .	61
4.3	In-plane and cross-plane phonon transport in superlattices . . . . .	63
4.3.1	Computational framework . . . . .	63
4.3.2	Results and discussion . . . . .	66
4.4	Conclusions . . . . .	69
<b>V. Transport in structures with reduced dimensionality: Graphene and carbon nanotubes . . . . .</b>		<b>72</b>
5.1	Introduction . . . . .	72
5.2	Structure and modeling . . . . .	73
5.3	Results . . . . .	74
5.4	Conclusions . . . . .	82
<b>VI. Quantum versus classical systems: Assessing the applicability of quantum corrections to classical thermal transport predictions . . . . .</b>		<b>84</b>
6.1	Introduction to quantum corrections . . . . .	84
6.2	Assessing the quantum corrections . . . . .	86
6.2.1	Quantum and classical thermal conductivity . . . . .	86
6.2.2	Quantum-corrected thermal conductivity . . . . .	90
6.2.3	Analyzing the quantum corrections . . . . .	92
6.2.4	Discussion . . . . .	96
6.3	Conclusions . . . . .	98
<b>VII. Conclusion and outlook . . . . .</b>		<b>100</b>
7.1	Overview . . . . .	100
7.2	Contribution . . . . .	103
7.3	Future work and outlook . . . . .	105
<b>BIBLIOGRAPHY . . . . .</b>		<b>108</b>
<b>APPENDICES</b>		
<b>A. Introduction to crystals and phonons . . . . .</b>		<b>120</b>
<b>B. Derivation of the lattice dynamics techniques . . . . .</b>		<b>133</b>
<b>C. Boundary scattering in thin films . . . . .</b>		<b>154</b>

## LIST OF TABLES

### Table

3.1	Root mean square displacements scaled by the nearest neighbor distance from the BTE-LD and BTE-MD methods. The data in the rightmost column are RMS displacements found directly from a time average of the atomic positions in MD simulations [89]. . . . .	34
3.2	Root mean square anharmonic frequency shifts and linewidths ( $\Gamma = 1/2\tau$ ) normalized by the quasi-harmonic frequencies from the BTE-LD and BTE-MD methods. .	37
3.3	Thermal conductivity values in W/m-K from the four prediction methods. The BTE-LD values computed using the quantum expressions for the occupation number and specific heat are included for reference. . . . .	40
4.1	Zero-temperature in-plane lattice parameter for LJ argon and SW silicon. . . . .	53
4.2	Predicted and/or measured bulk thermal conductivities for argon and silicon. The estimated uncertainty in all the LD predictions (due to the finite Brillouin zone resolution) is less than $\pm 5\%$ [71]. The uncertainty in the argon MD predictions is less than $\pm 5\%$ [39]. Based on typical predictions for SW silicon, the uncertainty in the silicon Green-Kubo MD result is estimated to be $\pm 20\%$ [13, 80, 81]. . . . .	55

## LIST OF FIGURES

### Figure

2.1	Schematic diagram of the simulation cell used in the direct MD thermal conductivity prediction method. . . . .	28
3.1	Linear extrapolation from LD-based predictions of $1/k$ versus $1/N_0$ at a temperature of 50 K. The line is fit to the four rightmost (filled) circles only. Reprinted with permission from [71]. Copyright <i>Physical Review B</i> 2009. . . . .	33
3.2	Frequency shift ( $\Delta$ ) and inverse of the lifetime ( $1/\tau$ ) at temperatures of 20 K and 50 K versus reduced wave vector for the longitudinal and transverse dispersion branches in the [100] direction. The MD data is found using (i) the full LJ potential, and (ii) the LJ potential truncated after the fourth-order term in the Taylor series expansion. While the results from the LD calculations are discrete, we plot the data as lines for clarity. Reprinted with permission from [71]. Copyright <i>Physical Review B</i> 2009. . . . .	36
3.3	Temperature dependence of the thermal conductivity predicted from the four methods. Using an isotropic approximation (Isotropic) rather than all the phonons in the full Brillouin zone (Full BZ) in the BTE-MD method causes the thermal conductivity to be under-predicted by a factor of about 1.5. Reprinted with permission from [71]. Copyright <i>Physical Review B</i> 2009. . . . .	39
3.4	Inverse relaxation time versus frequency as predicted by the BTE-LD method for temperatures of 20 and 50 K. . . . .	42
3.5	Dependence of the thermal conductivity and phonon DOS on $\omega_A/(\omega_A)_{max}$ at a temperature of 50 K. Reprinted with permission from [71]. Copyright <i>Physical Review B</i> 2009. . . . .	43
4.1	Schematic diagram of the thin film. The film is finite in the $z$ direction (terminating in free surfaces) and periodic in the $x$ and $y$ directions. . . . .	48
4.2	The scaling factors $F$ and $F_M$ [Eqs. (4.3) and (4.7)] plotted against $\delta$ for $p = 0$ and $p = 0.5$ . The ratio $(F - F_M)/F$ versus $\delta$ is shown in the inset for $p = 0$ . . . . .	51
4.3	Cross-plane argon lattice parameter versus $z/L_z$ for bulk 4, 8, and 32 atomic layers. . . . .	53
4.4	Surface atoms of thin film silicon in (a) bulk-like configuration and (b) relaxed configuration. . . . .	54
4.5	Thin film thermal conductivity as a fraction of the bulk thermal conductivity for LJ argon at a temperature of 20 K predicted from LD calculations and MD simulations using the Green-Kubo method. . . . .	56

4.6	Phonon DOS for 2.1 nm LJ argon thin films at a temperature of 0 K with free surfaces (Free) and embedded in bulk (Embedded). . . . .	57
4.7	Silicon thin film thermal conductivity normalized by the bulk thermal conductivity as found from (a) classical LD calculations and the Green-Kubo MD method at a temperature of 400 K and (b) quantum LD calculations and experiment at a temperature of 300 K. . . . .	59
4.8	Thin film thermal conductivity ratio ( $k_{\text{Film}}/k_{\text{Bulk}}$ ) versus $L_z/\Delta_{\text{Bulk}}$ for argon and silicon (300 K) thin films and estimations derived from theory. . . . .	60
4.9	Contribution to the phonon thermal conductivity versus frequency for SW silicon in bulk and 556 and 34.8 nm thin films at a temperature of 300 K. The area under each curve is proportional to the total thermal conductivity. . . . .	62
4.10	Schematic diagram of the superlattice. The superlattice is periodic in all three directions. The mass of material $B$ is two or five times that of material $A$ and $L_A = L_B = L/2$ . . . . .	63
4.11	In-plane (IP) and cross-plane (CP) thermal conductivities for (a) $m_B/m_A = 2$ and (b) $m_B/m_A = 5$ superlattices as a fraction of the thermal conductivity of bulk argon from LD and MD [85]. The prediction uncertainty is estimated to be $\pm 5\%$ for the LD method, due to the finite BZ resolution and $\pm 20\%$ for the Green-Kubo MD results [85]. . . . .	64
4.12	The (a) Phonon DOS and (b) in-plane and (c) cross-plane contributions to the thermal conductivity as a function of frequency for the $m_B/m_A = 2$ superlattices with $L = 0.537$ and $L = 4.30$ nm as well as bulk extents of materials $A$ and $B$ . The area under the phonon DOS curve is proportional to the number density of phonons (equal in all structures) while the area under the thermal conductivity contribution curves are proportional to the thermal conductivity of each structure. . . . .	65
5.1	Schematic diagram for graphene with carbon-carbon distance $d$ . The two and four atom unit cells are denoted by boxes. The four atom unit cell is used in this work. The two atom unit cell is the primitive cell. The primitive lattice vectors are given by $\mathbf{a}_1$ and $\mathbf{a}_2$ . The armchair CNTs are defined by the chiral vector $\mathbf{C}_h = l\mathbf{a}_1 + l\mathbf{a}_2$ , which gives the CNT's circumference (about the $x$ axis) and are denoted by $(l,l)$ . The unit cell used for the CNTs encloses the entire tube cross section and has a length ( $x$ extent) of $\sqrt{3}d$ ; the same as the four atom unit cell shown. . . . .	73
5.2	Dispersion curves in the $[100]$ direction and phonon DOS for graphene. . . . .	76
5.3	Dispersion curves and phonon DOS for the (5,5) CNT. . . . .	77
5.4	Dispersion curves and phonon DOS for the (10,10) CNT. . . . .	78
5.5	Thermal conductivity in graphene and armchair CNTs as predicted by the direct method and MD simulation [134]. . . . .	78
5.6	Spectral energy density around the lowest optical phonon mode at $\kappa_x = \frac{2\pi}{50a}$ in the (8,8) CNT [136]. . . . .	81

6.1	Thermal conductivity predictions for the quantum and classical systems and the quantum-corrected classical prediction using the ZP energy (QCs w/ ZP) and neglecting it (QCs w/o ZP). Reprinted with permission from [72]. Copyright <i>Physical Review B</i> 2009. . . . .	87
6.2	Phonon linewidths ( $\Gamma = \frac{1}{2\tau}$ ) plotted versus harmonic frequency for quantum and classical systems at a temperature of 100 K. Reprinted with permission from [72]. Copyright <i>Physical Review B</i> 2009. . . . .	89
6.3	Ratio of the quantum to classical phonon thermal conductivities plotted versus the relaxation time ratio for all phonon modes at a temperature of 100 K. Reprinted with permission from [72]. Copyright <i>Physical Review B</i> 2009. . . . .	89
6.4	Mapping between quantum and classical temperatures with and without the ZP energy and $dT^C/dT^Q$ as defined by Eqs. (6.2) and (6.3). Reprinted with permission from [72]. Copyright <i>Physical Review B</i> 2009. . . . .	91
6.5	Scaled contribution to the thermal conductivity as a function of frequency ratio. The classical results at all temperatures collapse to a single curve. Reprinted with permission from [72]. Copyright <i>Physical Review B</i> 2009. . . . .	93
6.6	Frequency-dependent quantum temperatures as determined by Eq. (6.5) for various classical temperatures. For temperatures less than 420 K, some of the high-frequency phonons cannot be mapped into any quantum system. Reprinted with permission from [72]. Copyright <i>Physical Review B</i> 2009. . . . .	95
A.1	Calculated (a) dispersion in the [100] direction and (b) phonon DOS for SW silicon. The longitudinal acoustic (LA), longitudinal optical (LO), transverse acoustic (TA), and transverse optical (TO) branches are labeled. The transverse branches are two-fold degenerate. . . . .	123
A.2	Dispersion curves in the [100] direction for argon using (a) the primitive unit cell and (b) the conventional unit cell. With the primitive (conventional) unit cell, the first BZ is defined by $-2\pi/a < \kappa \leq 2\pi/a$ ( $-\pi/a < \kappa \leq \pi/a$ ). For the conventional unit cell, the left ( $-2\pi/a < \kappa \leq -\pi/a$ ) and right ( $\pi/a < \kappa \leq 2\pi/a$ ) portions of the second BZ can be brought into the first BZ through translation by the reciprocal lattice vector, $2\pi/a$ . The phonon modes labeled $A$ and $B$ are able to combine to produce phonon mode $C$ . This 3-phonon interaction is a N-process in the primitive unit cell but an U-process in the conventional unit cell. In the U-process, phonon mode $C$ is brought back into the first BZ to the equivalent mode $C'$ through a translation by a reciprocal lattice. . . . .	126
A.3	Normalized displacements of the atoms along the [100] ( $x$ ) direction due to the LA and LO phonon modes at $\kappa = \pi/a$ in silicon as defined through the real part of $e\begin{pmatrix} \kappa & b \\ \nu & \alpha \end{pmatrix} \exp[i\kappa \cdot \mathbf{r}^{(l)}_b]$ . The shortest wavelengths that describe the displacements due to these LA and LO modes are $2a$ and $2a/3$ . . . . .	127



## NOMENCLATURE

$\mathbf{0}$	zero vector
$\hbar$	Plank's constant divided by $2\pi$ (1.054572E-34 J·s)
$\nabla$	gradient
$\mathbf{a}, a$	direct lattice translation vector, lattice parameter
$A, A^*$	creation operator, annihilation operator
$b$	index over atoms in unit cell
$c_{ph}$	volumetric specific heat
$C$	constant
$\underline{D}$	dynamical matrix
$\mathbf{e}, e, \tilde{e}$	polarization vector (mode shape, eigenvalue), component of polarization vector
$E$	total energy
$E_T$	transient energy
$f$	distribution function (occupation number)
$f'$	deviation of distribution function from equilibrium
$f_0$	equilibrium distribution function
$f_N$	equilibrium distribution function for N-processes
$F$	scale factor accounting for boundary scattering
$F_M$	scale factor accounting for boundary scattering when Matthiesen rule used

$\mathbf{F}_{ext}$	force vector from external source
$H$	Hamiltonian
$i$	imaginary number ( $\sqrt{-1}$ ), index
$\underline{I}$	identity matrix
$j$	integer
$\underline{k}, k$	thermal conductivity tensor, thermal conductivity
$k_B$	Boltzmann's constant (1.380650E-23 J/K)
$l$	index over unit cells, integer
$L$	superlattice period length
$L_z$	thin film thickness
$m$	mass
$n$	number of atoms in unit cell
$N, N_\alpha$	total number of unit cells, number of unit cells along direction $\alpha$
$\mathbf{p}$	momentum vector
$p$	specularity parameter
$\mathbf{q}$	heat flux vector
$q$	normal mode coordinate, heat flux component
$\dot{q}, \ddot{q}$	first and second time derivatives of the normal mode coordinate
$q_{ss}, q_T$	steady-state, transient part of the normal mode coordinate
$\mathbf{r}, r_\alpha$	position vector, position component along direction $\alpha$
$\mathbf{S}$	heat current vector
$t$	time
$T$	temperature
$u_\alpha, \dot{u}_\alpha$	component of displacement along direction $\alpha$ , time derivative of displacement comp

$\mathbf{v}$	velocity vector
$\mathbf{v}_g, v_{g,\alpha}$	group velocity vector, group velocity component along direction $\alpha$
$V$	volume

#### Greek symbols

$\alpha$	directional component
$\alpha, \beta, \eta, \zeta$	coefficients
$\Gamma$	linewidth
$\delta$	ratio of thin film thickness to cross-plane mean free path
$\Delta$	frequency shift
$\epsilon$	small, positive number, deviation of the distribution function from equilibrium
$\epsilon_{LJ}$	LJ energy scale
$\boldsymbol{\kappa}, \kappa_\alpha$	wave vector, wave vector component along direction $\alpha$
$\mathbf{K}$	reciprocal lattice vector
$\Lambda$	phonon mean free path
$\nu$	dispersion branch
$\xi$	energy flux
$\sigma_{LJ}$	LJ length scale
$\tau, \tau_M$	relaxation time (lifetime), effective relaxation time using Matthiessen rule
$\tau_0$	integration time, time constant
$\tau_N$	relaxation time for N-processes
$\tau_{p-p}, \tau_b$	phonon-phonon relaxation time, phonon-boundary relaxation time
$\phi$	energy
$\Phi$	potential energy, Fourier transformed potential energy, spectral energy density

$\chi$	$\frac{\hbar\omega}{k_B T}$
$\psi, \psi$	eigenfunction, eigenstate of Schrödinger equation
$\omega, \omega_0$	frequency
$\Omega$	frequency

#### Subscripts

$A$	anharmonic, material $A$
$B$	material $B$
$C$	denotes property of the crystal
max	denotes maximum value
$S$	denotes property of a subatomic particle
$x, y, z$	Cartesian component

#### Superscripts

$+, -$	denotes phonon traveling in positive or negative direction
$*$	denotes conjugate transpose
$C$	denotes classical value
$Q$	denotes quantum value

#### Abbreviations

BCC	body-centered cubic
BTE	Boltzmann transport equation
BZ	Brillouin zone

CNT	carbon nanotube
DFPT	density functional perturbation theory
DOS	density of states
FCC	face-centered cubic
LD	lattice dynamics
LJ	Lennard-Jones
MD	molecular dynamics
MFP	mean free path
N	normal (-process)
QC	quantum correction
RMS	root mean square
RTA	relaxation time approximation
SC	simple cubic
SW	Stillinger-Weber
U	Umklapp (-process)
ZP	zero-point

## Functions

$(\ )_p$	Cauchy principal value
$\delta(\ )$	Dirac delta function
$\delta_{\mathbf{K}}(\ )$	unity if argument is zero or a multiple of $\mathbf{K}$ , zero otherwise

## CHAPTER I

### Introduction

#### 1.1 Motivation

Many modern electronic devices such as microprocessors, solid-state memory, and semiconductor light-emitting diodes incorporate components with features that have dimensions on the nano-scale [1–4]. Due to the generation of waste heat in these small components, power densities are high and effective heat removal is critical to the operation and reliability of the device [2, 4–6]. Thus, thermal modeling and design of these devices is of great importance. Unfortunately, thermal modeling of these devices is hampered by the fact that continuum models of thermal transport, such as the Fourier law, are invalid at such small length scales. Continuum thermal models do not account for the complex interactions that exist between the energy carriers and closely spaced interfaces and boundaries.

A common approach to modeling sub-continuum thermal transport is to use continuum modes with thermal properties adjusted to account for the effective thermal transport. Such an approach can be used to model thermal transport across sub-continuum regimes but not within them. For example, applying the Fourier law to a thin film using an effective thermal conductivity can give the heat flux across the film but not the temperature gradient within the film.

The thermal conductivity is a particularly difficult thermal property to describe in a sub-continuum regime. The thermal conductivity is generally treated as a function of material and temperature; however, surfaces and interfaces in nano-structured materials can also give thermal conductivity a geometry dependence [2]. Geometry dependent thermal properties also leads to the possibility of selectively engineering, through nano-structuring, materials with desired thermal characteristics. An example of such a material is the superlattice, which is a layered structure consisting of thin films of two or more materials. Superlattices have potential application in thermoelectric energy conversion devices where a low thermal conductivity is needed to maximize efficiency [7–12]. A fundamental understanding of the mechanisms of thermal transport in nano-sized features and a means of computing the effective thermal conductivity of such features are necessary in order to fully exploit nano-structured devices.

The current, standard approach for characterizing the thermal conductivity is to measure it for each material at a series of temperatures. The added complication of the geometry dependence of the thermal properties of materials as well as the extremely small size makes this type of approach difficult and time intensive [1]. For this reason, investigators have turned to numerical studies to assist in both characterizing and designing nano-structured materials [2]. Examples of recent atomistic work include thermal conductivity predictions for silicon thin films [13–15] and nano-wires [15, 16], Si/Ge [9, 17–20] and Si/SiGe [10, 20] superlattices, and carbon nanotubes [21–23].

Despite all the effort invested in analyzing nano-structured materials, fundamental questions about the nature of thermal transport on the carrier level still exist. In thin films, for instance, it is unclear how much of the observed thermal conductivity reduction is due to changes in the carrier properties and how much is due to

carriers scattering with the boundary. Likewise, thermal transport through superlattices needs to be further examined by investigating how the carrier characteristics in the different regions affects their transport through the heterostructure [24]. This limited understanding of carrier-level thermal transport in nano-structures is exasperated by inadequate models of carrier transport in bulk materials, which rely on fitting parameters and major approximations [2, 15, 25].

## 1.2 Thermal conductivity at the carrier level

The Fourier law,

$$\mathbf{q} = -\underline{k}\nabla T, \quad (1.1)$$

which describes the conductive heat transfer in a solid or a quiescent fluid, states that the heat flux vector,  $\mathbf{q}$ , is proportional to the spatial gradient ( $\nabla$ ) of temperature,  $T$ . The proportionality constant,  $\underline{k}$ , is the thermal conductivity. The thermal conductivity is, in general, a second rank, symmetric tensor. Though formally defined by an empirical relation [Eq. (1.1)], the thermal conductivity is related to the properties of the sub-continuum energy carriers, specifically, the electrons and phonons. The thermal conductivity encompasses all the complexities of the dynamics and interactions of these carriers. Phonons and electrons interact in complex ways with themselves, each other, and with material boundaries and defects. These interactions, along with carrier heat capacities and velocities, give rise to the thermal conductivity [26].

Implicit in the Fourier law is the assumption that the energy carriers travel diffusively. Diffusive transport occurs when few or none of the carriers can traverse a material without scattering, making boundary scattering insignificant. When the carriers travel diffusively, the thermal conductivity depends upon the material and its temperature only. The opposite of diffusive transport is ballistic transport. In



ballistic transport, a large number of carriers originate at one boundary, transverse the material without scattering, then scatter at another material boundary. Boundary scattering is significant in the ballistic transport regime and the effective thermal conductivity depends on the geometry as well as material and temperature.

Due to the increasing prevalence of nano-structured devices and the desire to employ nano-structuring to selectively tune material properties, it is vital to develop a solid understanding of the physics of carrier transport in such devices and materials. Unfortunately, the current understanding of carrier-level transport is lacking, particularly for phonons, even in bulk materials. For example, which phonon modes dominate energy transport and the importance of interactions involving four or more phonons are typically unknown. The situation becomes more complicated in nano-structures where the energy carriers interact with surfaces and interfaces.

Thermal transport in insulators and semiconductors is dominated by phonons, while in metals, electrons are the primary carriers [27]. Because insulators and semiconductors are integral to many nano-structured devices, substantial effort has gone into developing adequate theories of phonon transport [7,28–37]. These efforts focused primarily on employing the Boltzmann transport equation to describe the statistical time evolution of individual phonon modes. However, due to the use of major approximations and assumptions, this work has been qualitative or semi-empirical in nature [25,38–40]. The thermal conductivity has also been predicted numerically with molecular dynamics (MD) simulations [13,41,42]. While these studies have been successful in predicting the thermal conductivity, they have done little to advance the understanding of the phonon-level interactions.

### 1.3 Objectives and scope

There are two major objectives for this work:

- ◊ To develop the tools and techniques necessary to perform an accurate prediction of the thermal conductivity.
- ◊ To apply these tools to study thermal transport in bulk systems and in technologically important systems with nano-sized features.

The first objective is achieved by introducing a numerical framework whereby the Boltzmann transport equation (BTE) is used to model phonon transport and the quasi-harmonic and anharmonic lattice dynamics (LD) calculation methods are used to compute the phonon properties. This framework is used to predict the lattice thermal conductivity and examine the characteristics of phonon transport in bulk crystals, nano-structures, and structures with reduced dimensionality.

In Chapter II, the BTE is presented and applied to a system of phonons driven by a temperature gradient. By combining the BTE with the Fourier law, a simple expression is derived which relates the thermal conductivity to the phonon properties. Several methods for determining the phonon properties are then presented. The commonly used models of Callaway and Holland, which use empirical data with scaling laws derived from theoretical arguments are presented first. Next, the quasi-harmonic and anharmonic LD calculation methods, which are used throughout this work, are discussed in detail. Finally, several methods that use MD simulation are discussed.

The LD calculation methods are used with the BTE in Chapter III to predict the thermal conductivity of bulk argon and silicon crystals modeled with interatomic potentials. The accuracy and limitations of the LD methods are rigorously assessed by comparing to results obtained from MD simulations. The phonon properties ob-

tained through LD calculations are then used to examine the characteristics of phonon transport through bulk argon and silicon crystals.

Chapters IV and V are dedicated to the analysis of materials with nano-sized features using the LD methodology. In Chapter IV, the LD methods are extended to model thermal transport in argon and silicon thin films and ideal superlattices. The changes in phonon transport characteristics due to reduced dimensionality in graphene and carbon-nanotubes (CNTs) are examined Chapter V. In all cases, the thermal conductivity predictions made using the LD techniques are compared to predictions made using MD simulations.

In Chapter VI the unique capabilities of the LD calculation methods are used to assess the validity of quantum corrections (QCs) commonly applied to thermal conductivity predictions obtained from MD simulations. It is determined that these QCs do not properly account for the differences between quantum and classical systems.

In Chapter VII, the prediction methodology using the LD calculation techniques and the BTE is summarized and discussed in the context of the previous Chapters. Directions for future research employing the LD techniques are also suggested.

## CHAPTER II

### Phonon transport models: Theory and practice

#### 2.1 The Boltzmann transport equation

The Boltzmann transport equation is a semi-classical treatment of particle dynamics. The equation was originally developed by Ludwig Boltzmann in 1872 to describe the dynamics of particles in a gas. It has since been adapted to fit a wide variety of problems including subatomic particles such as photons [43] and neutrinos [44] and has even been extended to model the dynamics of galaxies [45].

The success of the BTE is due to its generality. The equation is simply a means of tracking the statistical behavior of particles as they evolve over time,  $t$ , and through position,  $\mathbf{r}$ , and momentum,  $\mathbf{p}$ , space (phase space). In its general form, the BTE is

$$\left( \frac{\partial}{\partial t} + \mathbf{v} \cdot \nabla_{\mathbf{r}} + \mathbf{F}_{ext} \cdot \nabla_{\mathbf{p}} \right) f(\mathbf{r}, \mathbf{p}, t) = \left( \frac{\partial f}{\partial t} \right)_{coll}, \quad (2.1)$$

where  $\nabla_{\mathbf{r}}$  and  $\nabla_{\mathbf{p}}$  denote the gradient of the position and momentum vectors,  $\mathbf{v}$  is the particle velocity, and  $\mathbf{F}_{ext}$  is a vector describing the force on the particles due to an external influence. The term  $f(\mathbf{r}, \mathbf{p}, t)$  is the single particle distribution function which expresses how a particular type of particle is distributed throughout phase space at any given time. The operators acting on the distribution function describe the evolution of a group of particles that are noninteracting and obey Newtonian mechanics. The ability for particles to interact is included through the addition of

the collision term on the right hand side. Though it is conventionally expressed as  $(\frac{\partial f}{\partial t})_{coll}$ , the collision term is not a derivative of the distribution function. It is, in general, a complicated function that embodies all of the particle interactions.

The BTE can be used to solve for thermal transport in materials at the carrier level. Specifically, in using the BTE to predict the thermal conductivity, several simplifications can be made. The driving force behind thermal transport is a temperature gradient. It is therefore desirable to write the carrier distribution as a function of temperature only. It is assumed that there are no external forces acting on the carriers and that the system is at steady state. These two assumptions remove the time and momentum derivatives on the left hand side of Eq. (2.1). The reformulated BTE is written as

$$\mathbf{v} \cdot \nabla_{\mathbf{r}} T \frac{\partial f}{\partial T} = \left( \frac{\partial f}{\partial t} \right)_{coll}. \quad (2.2)$$

Despite the seemingly simple form of Eq. (2.2), it is generally very difficult to solve. The main difficulty comes from the collision term. The collision term is, in general, quite complicated and dependent upon both the specific system and particle type. One popular approximation used for the BTE is the relaxation time approximation (RTA).

For a system of particles in non-equilibrium, the collision term in the Boltzmann transport equation will tend to drive the particle distributions toward their equilibrium values. For systems initially at equilibrium, the collision term will cause the distribution functions to fluctuate about their equilibrium values. This fluctuation motivates the RTA, under which the collision term is replaced with a fluctuating distribution and an associated time constant.

In making the RTA, the distribution function is written as the sum of the equilibrium distribution function,  $f_0$  and the fluctuation about equilibrium,  $f'$ . The fluc-

tuation in the carrier distribution arises solely from carrier interaction through the collision term. Generally the fluctuations will be much smaller than the equilibrium distribution. Assuming the fluctuations to be independent of temperature allows one to make the approximation  $\frac{\partial f}{\partial T} \approx \frac{\partial f_0}{\partial T}$ . The final step is to make the substitution  $(\frac{\partial f}{\partial t})_{coll} = \frac{-f'}{\tau}$  where  $\tau$  is called the relaxation time [46]. The relaxation time is interpreted as the expected time between scattering events for a carrier type. By making the appropriate substitutions, (2.2) can be solved to give

$$f'(\boldsymbol{\kappa}) = -\tau(\boldsymbol{\kappa}) \mathbf{v}_g(\boldsymbol{\kappa}) \cdot \nabla_{\mathbf{r}} T \frac{\partial f_0(\boldsymbol{\kappa})}{\partial T}, \quad (2.3)$$

where the dependence on the phonon mode denoted by wave vector,  $\boldsymbol{\kappa}$ , and dispersion branch,  $\nu$ , is explicitly written. The relevant velocity is the group velocity defined as

$$\mathbf{v}_g(\boldsymbol{\kappa}) = \frac{\partial \omega(\boldsymbol{\kappa})}{\partial \boldsymbol{\kappa}}, \quad (2.4)$$

where  $\omega$  is the frequency of the phonon.

The relaxation time, like the collision term, is difficult to determine. The advantage of the relaxation time approximation though, is that it allows the collision term to be decomposed into a fluctuation in the population of carriers and an associated time constant. If the relaxation times of the energy carriers can be determined through some external means, Eq. (2.3) provides a simple expression for the mean fluctuations about the equilibrium distributions.

Knowledge of the fluctuations is useful in computing the thermal conductivity. The heat flux due to phonons can be expressed as [47]

$$\mathbf{q} = \sum_{\boldsymbol{\kappa}} \sum_{\nu} \hbar \omega \mathbf{v}_g f', \quad (2.5)$$

where  $\hbar$  is Planck's constant divided by  $2\pi$ . Equations (1.1), (2.3), and (2.5) can be combined to give an expression for the thermal conductivity tensor under the RTA

as

$$\underline{k} = \sum_{\nu} \sum_{\kappa} c_{ph} \mathbf{v}_{g(\nu)}^* \mathbf{v}_{g(\nu)} \tau(\kappa), \quad (2.6)$$

where  $c_{ph}$  is the phonon specific heat. Phonons are bosons, which follow the Bose-Einstein distribution. This distribution and the associated specific heat are

$$f = [\exp(\hbar\omega/k_B T) - 1]^{-1} \quad (2.7)$$

and

$$c_{ph} = \frac{\hbar\omega}{V} \frac{\partial f}{\partial T} = \frac{k_B \chi^2 e^\chi}{(e^\chi - 1)^2}. \quad (2.8)$$

where  $\chi = \frac{\hbar\omega}{k_B T}$ . The thermal conductivity in the classical (*i.e.*, high-temperature) limit can be obtained by using the classical expressions, denoted by a C superscript, for the phonon distribution,

$$f^C = \frac{1}{\chi}, \quad (2.9)$$

and specific heat,

$$c_{ph}^C = \frac{k_B}{V}, \quad (2.10)$$

in place of the quantum expressions.

If the crystal is cubically symmetric, the diagonal elements of the thermal conductivity tensor are equal. In this case, the thermal conductivity can be completely defined by the scalar

$$k = \sum_{\kappa} \sum_{\nu} c_{ph}(\kappa) v_{g,x}^2(\nu) \tau(\kappa), \quad (2.11)$$

where  $v_{g,x}$  is the  $x$ -component of the phonon group velocity (*i.e.*, along the [100] direction). Equation (2.11) is used directly throughout this work. The difficult term to evaluate in Eq. (2.6) or Eq. (2.11) is the relaxation time. Much of the effort to develop theoretical models of lattice thermal conductivity has been in developing expressions for the relaxation time.

The Boltzmann transport equation under the relaxation time approximation provides a way of computing the lattice thermal conductivity provided that the relaxation times are known. This requirement is not easy to fulfill. The phonon relaxation times are dependent upon complex interactions between phonons and boundaries, defects, isotopes, electrons, and other phonons. Semi-empirical theories, presented in Section 2.2, have been suggested that provide functional forms for the relaxation times of individual scattering events but rely upon unrealistic approximations and fits to experimental data. Methodologies that use atomic level calculations improve upon the limitations of the semi-empirical models and are presented in Sections 2.3 and 2.4.

## 2.2 Semi-empirical models

Phonons scatter through a variety of ways, each giving rise to a relaxation time. The phonon thermal conductivity will generally rely upon the phonon scattering rates from boundaries, defects, isotopes, electrons, and other phonons. If these scattering events are independent of each other the effective relaxation time  $\tau_M$  can be obtained by the Matthiessen rule and written as

$$\frac{1}{\tau_M} = \sum_i \frac{1}{\tau_i}, \quad (2.12)$$

where the sum is over all independent scattering events for a given phonon mode. Several notable attempts have been made to specify the relaxation times for these scattering mechanisms from theoretical arguments. Some of the early pioneers were Debye and Peierls [19, 28], who developed much of the basis for later theory, and Klemens [46], who developed some relaxation time dependencies based upon intuitive arguments.

For phonon-phonon scattering, usually only interactions involving three phonons are considered. Four- and higher-order phonon interactions are typically considered



to be too rare to contribute significantly to the thermal resistance. Three phonons can interact in two ways. A single phonon can decay into two phonons, in a type I interaction, or two phonons can combine to form a third, in a type II interaction. The other two possibilities where three phonons spontaneously appear or disappear cannot occur in a crystal since they would violate conservation of energy. In addition to energy, phonon interactions must conserve quasi-momentum (crystal momentum) up to a reciprocal lattice vector. The conditions that need to be satisfied for a phonon-phonon interaction to occur can be written as

$$\hbar\omega(\boldsymbol{\kappa}) = \hbar\omega(\boldsymbol{\kappa}') + \hbar\omega(\boldsymbol{\kappa}'') \quad \hbar\boldsymbol{\kappa} = \hbar\boldsymbol{\kappa}' + \hbar\boldsymbol{\kappa}'' + j\hbar\mathbf{K} \quad \textit{Type I} \quad (2.13a)$$

$$\hbar\omega(\boldsymbol{\kappa}) + \hbar\omega(\boldsymbol{\kappa}') = \hbar\omega(\boldsymbol{\kappa}'') \quad \hbar\boldsymbol{\kappa} + \hbar\boldsymbol{\kappa}' = \hbar\boldsymbol{\kappa}'' + j\hbar\mathbf{K} \quad \textit{Type II}, \quad (2.13b)$$

where  $\mathbf{K}$  is any reciprocal lattice vector and  $j$  is an integer. Interactions where  $j$  is zero are called Normal (N) processes while for Umklapp (U) processes  $j$  is nonzero. The distinction is made between the two processes because it is generally thought that N-processes by themselves cannot contribute to thermal resistance [27, 46]. However, in Appendix A, this thinking is shown to be incorrect; N-processes do contribute to thermal resistance and are indistinguishable from U-processes.

Two of the more famous semi-empirical thermal conductivity models are due to the works of Callaway and Holland [30, 31]. Callaway's contribution to the theory of thermal conductivity is notable because the theory has been used to successfully describe the experimental conductivity trends of bulk insulating crystals, silicon and germanium in particular [30, 31]. Callaway espoused the importance of N-processes on the thermal conductivity, stating that while they may not directly contribute to thermal resistance, they redistribute energy among the different phonon modes. Since this effect due to N-processes is indirect, their contribution cannot simply be added

to the effective relaxation time. In the Callaway model it is assumed that the collision term can be written as

$$\left(\frac{\partial f}{\partial t}\right)_{coll} = \frac{f_N - f}{\tau_N} + \frac{-f'}{\tau_{eff}}, \quad (2.14)$$

where  $f_N$  is the equilibrium distribution for N-processes (this is different from the total equilibrium distribution,  $f_0$ ) and  $\tau_N$  is the relaxation time for N-processes. Callaway used this expression in the BTE to derive an expression for the lattice thermal conductivity based on the Debye approximations and several parameters fit to experimental data.

Holland extended Callaway's method by separating the longitudinal and transverse acoustic phonons. In doing so Holland uses more information about the phonons than does Callaway. The additional information combined with a new functional form of the relaxation time for transverse phonons scattering by U-processes allows the Holland model to provide a much better fit to silicon and germanium thermal conductivity data, especially at high temperatures [31]. Though developed in the 1960s, the Holland model is widely used today [15, 33, 36, 48, 49] because it is still one of the most sophisticated of the semi-empirical models of phonon transport.

These semi-empirical models are important because they were an attempt to reduce the phonon relaxation times, which involve complex interactions between multiple phonons, to simple expressions based on the phonon frequencies. These models necessarily employ multiple approximations and parameters fit to experimental data. Hence, their usefulness is inherently limited. The treatment of the N-processes in the Callaway model (which is the basis of the popular Holland model) illustrates the limitations of these semi-empirical methods. In Appendix A, it is shown that N- and U-processes are indistinguishable, however, in the Callaway model, these processes are treated with separate theories as distinct processes with dissimilar characteristics.

This inconsistency is obscured by the approximations and fitting parameters used in the method [15,25]. For these reasons, a more rigorous and self-consistent method of calculating the phonon relaxation times is needed.

## **2.3 Lattice dynamics calculation**

### **2.3.1 Harmonic lattice dynamics**

Many of the limitations of the semi-empirical models can be overcome by using harmonic and anharmonic LD calculations to determine the phonon properties needed to evaluate Eq. (2.6). The LD techniques are an approximate analytical solution of the dynamics of the atoms in a crystal and are formally derived in Appendix B.

Harmonic LD is a means of computing the vibrational frequencies and modes available in a crystal lattice. These vibrations are the phonons. Harmonic LD is a well established technique [50] and is included in most texts on solid state physics because of its usefulness in computing many thermodynamic properties of crystals [47,51,52]. Using the method, the phonon dispersion curves and density of states (DOS) can be directly computed.

The main approximation used in harmonic LD is the harmonic approximation. In the harmonic approximation, the atoms in a crystal are assumed to sit at their zero temperature equilibrium positions and are also assumed to interact through Hooke's law. In other words, the crystal is modeled as a system of masses and linear springs. This approximation is only valid if the atomic motion is small in comparison to the spacing between neighboring atoms. The spring constants, also termed force constants, can be found by twice differentiating the potential energy,  $\Phi$ , with respect to the average atomic positions at zero temperature. For a three dimensional crystal with  $N$  lattice sites and  $n$  atoms in the unit cell, this model results in  $3nN$  coupled

differential equations that describe the atomic motion. The number of equations can be reduced to  $3n$  by introducing the wave vector,  $\boldsymbol{\kappa}$ , and using the translational symmetry inherent in crystal lattices. These equations of motion can be solved as an eigenvalue problem:

$$[\underline{D}(\boldsymbol{\kappa}) - \underline{I}\omega^2(\nu)] \mathbf{e}(\nu) = \mathbf{0}, \quad (2.15)$$

where  $\nu$  indexes over the  $3n$  solutions (dispersion branches) at each of the  $N$  allowed wave vectors in the first Brillouin zone. The identity matrix,  $\underline{I}$ , and the dynamical matrix,  $\underline{D}(\boldsymbol{\kappa})$ , have dimension  $3n \times 3n$ . The elements of the dynamical matrix are defined by [53, 54]

$$D_{3(b-1)+\alpha, 3(b'-1)+\alpha'}(\boldsymbol{\kappa}) = \frac{1}{\sqrt{m_b m_{b'}}} \sum_{l'}^N \frac{\partial^2 \Phi}{\partial r_{\alpha(b)}^{(0)} \partial r_{\alpha'(b')}^{(l')}} \bigg|_o \exp \left\{ i\boldsymbol{\kappa} \cdot [\mathbf{r}_{(b')}^{(l')} - \mathbf{r}_{(b)}^{(0)}] \right\}, \quad (2.16)$$

where  $\mathbf{r}_{(b)}^{(l)}$  is the average position vector for the  $b^{\text{th}}$  atom in the  $l^{\text{th}}$  unit cell with  $r_{\alpha}^{(l)}$  its  $\alpha$ -component, and  $m_b$  is the atomic mass of atom  $b$ . The eigenvalues are the squares of the phonon frequencies,  $\omega$ , and the eigenvectors,  $\mathbf{e}$ , are the mode shapes of the vibrations.

The harmonic approximation is useful in that it simplifies the equations of motion permitting an analytical solution of the system dynamics. Using the phonon frequencies given by Eq. (2.15), the Hamiltonian can be written in terms of non-interacting phonon mode coordinates,  $q(\nu)$ , as

$$H = \frac{1}{2} \sum_{\boldsymbol{\kappa}, \nu}^{N, 3n} \dot{q}^*(\nu) \dot{q}(\nu) + \frac{1}{2} \sum_{\boldsymbol{\kappa}, \nu}^{N, 3n} \omega^2(\nu) q^*(\nu) q(\nu), \quad (2.17)$$

where the asterisk (\*) superscript denotes the complex conjugate. The normal mode coordinate and its time derivative are

$$q(\nu) = \sum_{\alpha, b, l}^{3, n, N} \sqrt{\frac{m_b}{N}} u_{\alpha(b)}^{(l)} e^*(\nu)_{\alpha} \exp[-i\boldsymbol{\kappa} \cdot \mathbf{r}_{(b)}^{(l)}], \quad (2.18)$$

and

$$\dot{q}_{(\nu)}^{(\kappa)} = \sum_{\alpha, b, l}^{3, n, N} \sqrt{\frac{m_b}{N}} \dot{u}_{\alpha}^{(l)}(b) e_{(\nu)}^{*(\kappa, b)}_{\alpha} \exp[-i\kappa \cdot \mathbf{r}_{(b)}^{(l)}], \quad (2.19)$$

where  $u_{\alpha}^{(l)}(b)$  and  $\dot{u}_{\alpha}^{(l)}(b)$  are the displacement from equilibrium and velocity for the  $\alpha$ -direction of the  $b^{\text{th}}$  atom in the  $l^{\text{th}}$  unit cell and  $e_{(\nu)}^{*(\kappa, b)}_{\alpha}$  is the component of the mode shape associated with atom  $b$  and direction  $\alpha$ . The equations of motion for each phonon mode that satisfy the Hamiltonian are

$$\ddot{q}_{(\nu)}^{(\kappa)} = -\frac{\partial H}{\partial q_{(\nu)}^{(\kappa)}} = -\omega_{(\nu)}^2(\kappa) q_{(\nu)}^{(\kappa)}. \quad (2.20)$$

These equations have solutions of the form

$$q_{(\nu)}^{(\kappa)} = C_1(\kappa) \exp[i\omega_{(\nu)}(\kappa) t] + C_2(\kappa) \exp[-i\omega_{(\nu)}(\kappa) t], \quad (2.21)$$

where  $C_1(\kappa)$  and  $C_2(\kappa)$  are real constants. From Eq. (2.21) it is clear that the normal mode coordinates describe traveling waves.

The harmonic approximation is exact in the limit of zero atomic motion. This condition is satisfied in a classical system only at zero temperature and is never exactly fulfilled in a quantum system (due to zero-point motion). As the atomic motion increases, along with temperature, two issues arise. The first issue is due to thermal expansion/contraction. The spacing between the average positions of the atoms in a crystal can change with temperature. This issue is solved by using quasi-harmonic LD. The only difference between quasi-harmonic and harmonic LD is that in quasi-harmonic LD, the derivatives of the potential energy is taken with respect to the average, finite-temperature atomic positions. This extension of harmonic LD accounts for the effects of thermal expansion/contraction on the phonon frequencies but still neglects the effects of finite atomic motion. This second issue is accounted for by using anharmonic LD calculations.

### 2.3.2 Anharmonic lattice dynamics

#### Overview

Anharmonic LD is the natural extension of quasi-harmonic lattice dynamics. Only the second-order derivatives of the potential energy are considered in quasi-harmonic LD. In anharmonic LD, higher (usually third- and fourth-) order derivatives are included as a perturbation to the quasi-harmonic frequencies. The anharmonic LD method, to second-order in the perturbation, is derived in Appendix B. The end result of the derivation are expressions for the frequency shift,  $\Delta$ , and linewidth,  $\Gamma$ , for each phonon mode due to anharmonic interactions with other phonons.

The frequency shifts and linewidths, accurate to second order in the anharmonic perturbation, are given by

$$\begin{aligned}
\Delta(\kappa_\nu) = & \frac{\hbar}{16N} \sum_{\kappa', \nu'}^{N, 3n} \sum_{\kappa'', \nu''}^{N, 3n} |\Phi(\kappa_\nu \kappa' \kappa'')|^2 \left\{ [f_0(\kappa'_\nu) + f_0(\kappa''_{\nu''}) + 1] \left[ (\omega(\kappa_\nu) - \omega(\kappa'_\nu) - \omega(\kappa''_{\nu''}))_p^{-1} - (\omega(\kappa_\nu) + \omega(\kappa'_\nu) + \omega(\kappa''_{\nu''}))_p^{-1} \right] \right. \\
& + [f_0(\kappa'_\nu) - f_0(\kappa''_{\nu''})] \left[ (\omega(\kappa_\nu) + \omega(\kappa'_\nu) - \omega(\kappa''_{\nu''}))_p^{-1} - (\omega(\kappa_\nu) - \omega(\kappa'_\nu) + \omega(\kappa''_{\nu''}))_p^{-1} \right] \Big\} \\
& + \frac{\hbar}{8N} \sum_{\kappa', \nu'}^{N, 3n} \sum_{\nu''}^{3n} \Phi(\kappa_\nu - \kappa' \mathbf{0}_{\nu''}) \Phi(\kappa'_\nu - \kappa' \mathbf{0}_{\nu''}) [2f_0(\kappa'_\nu) + 1] (\omega(\mathbf{0}_{\nu''}))_p^{-1} \\
& + \frac{\hbar}{8N} \sum_{\kappa', \nu'}^{N, 3n} \Phi(\kappa_\nu \kappa' - \kappa' \kappa'_\nu) [2f_0(\kappa'_\nu) + 1] \quad (2.22)
\end{aligned}$$

$$\begin{aligned}
\Gamma(\kappa_\nu) = & \frac{\pi \hbar}{16N} \sum_{\kappa', \nu'}^{N, 3n} \sum_{\kappa'', \nu''}^{N, 3n} |\Phi(\kappa_\nu \kappa' \kappa'')|^2 \left\{ [f_0(\kappa'_\nu) + f_0(\kappa''_{\nu''}) + 1] [\delta(\omega(\kappa_\nu) - \omega(\kappa'_\nu) - \omega(\kappa''_{\nu''})) - \delta(\omega(\kappa_\nu) + \omega(\kappa'_\nu) + \omega(\kappa''_{\nu''}))] \right. \\
& + [f_0(\kappa'_\nu) - f_0(\kappa''_{\nu''})] [\delta(\omega(\kappa_\nu) + \omega(\kappa'_\nu) - \omega(\kappa''_{\nu''})) - \delta(\omega(\kappa_\nu) - \omega(\kappa'_\nu) + \omega(\kappa''_{\nu''}))] \Big\} \\
& + \frac{\pi \hbar}{8N} \sum_{\kappa', \nu'}^{N, 3n} \sum_{\nu''}^{3n} \Phi(\kappa_\nu - \kappa' \mathbf{0}_{\nu''}) \Phi(\kappa'_\nu - \kappa' \mathbf{0}_{\nu''}) [2f_0(\kappa'_\nu) + 1] \delta(\omega(\mathbf{0}_{\nu''})) \quad (2.23)
\end{aligned}$$

In these two equations,

$$\begin{aligned} \Phi(\kappa_1 \kappa_2 \dots \kappa_i) = & \sum_{\alpha_1, b_1}^{3,n} \sum_{\alpha_2, b_2, l_2}^{3,n,N} \dots \sum_{\alpha_i, b_i, l_i}^{3,n,N} \delta_{\mathbf{K}}(\kappa_1 + \kappa_2 + \dots + \kappa_i) \frac{\partial^i \Phi}{\partial r_{\alpha_1}^{(0)} \partial r_{\alpha_2}^{(l_2)} \dots \partial \mathbf{r}_{\alpha_i}^{(l_i)}} \Big|_o \\ & \times \frac{\tilde{e}(\kappa_1 \ b_1)}{\sqrt{m_{b_1} \omega(\kappa_1)}} \tilde{e}(\kappa_2 \ b_2) \dots \tilde{e}(\kappa_i \ b_i)}{\sqrt{m_{b_2} \omega(\kappa_2)} \dots m_{b_i} \omega(\kappa_i)} \exp[i\kappa_2 \cdot \mathbf{r}_{(0)}^{(l_2)}] \dots \exp[i\kappa_i \cdot \mathbf{r}_{(0)}^{(l_i)}], \end{aligned} \quad (2.24)$$

where

$$\tilde{e}(\kappa \ b) = e(\kappa \ b) \exp[i\kappa \cdot \mathbf{r}_{(b)}^{(0)}]. \quad (2.25)$$

The Kronecker delta,  $\delta_{(\kappa_1 + \kappa_2 + \dots + \kappa_i), \mathbf{K}}$ , is one if the sum of the wave vectors is a reciprocal lattice vector,  $\mathbf{K}$ , and zero otherwise. Equations (2.22) and (2.23) can be computed in the classical limit by letting  $f_0 + 1/2 = f_0^C$ .

The anharmonic corrections to the quasi-harmonic frequencies include contributions from three- and four-phonon processes, which depend upon the third- and fourth-order derivatives of the potential energy. The delta functions in Eq. (2.23) impose energy conservation and can be interpreted as decay channels whereby the phonon of interest splits into two phonons in a Type I interaction  $[\delta(\omega(\kappa_\nu) - \omega(\kappa'_\nu) - \omega(\kappa''_\nu))]$  or combines with another phonon to produce a third as in a Type II interaction  $[\delta(\omega(\kappa_\nu) \pm \omega(\kappa'_\nu) \mp \omega(\kappa''_\nu))]$ . The Kronecker delta in Eq. (2.24) enforces conservation of quasi-momentum, exactly for N-processes and up to a reciprocal lattice vector for U-processes.

Using the anharmonic corrections, the normal mode coordinates become

$$q_A(\kappa_\nu) = q_{SS}(\kappa_\nu) + q_T(\kappa_\nu), \quad (2.26)$$

where the steady-state (equilibrium) and transient parts are

$$q_{SS}(\kappa_\nu) = C_1(\kappa_\nu) \exp[i(\omega(\kappa_\nu) + \Delta(\kappa_\nu))t] + C_2(\kappa_\nu) \exp[-i(\omega(\kappa_\nu) + \Delta(\kappa_\nu))t] \quad (2.27)$$

and

$$q_T(\boldsymbol{\kappa}) = \exp[-\Gamma(\boldsymbol{\kappa}) t] \{ C_3(\boldsymbol{\kappa}) \exp[i(\omega(\boldsymbol{\kappa}) + \Delta(\boldsymbol{\kappa}))t] + C_4(\boldsymbol{\kappa}) \exp[-i(\omega(\boldsymbol{\kappa}) + \Delta(\boldsymbol{\kappa}))t] \}. \quad (2.28)$$

Equation (2.26) describes the return to the equilibrium state [Eq. (2.27)] through the decay ( $C_3 + C_4 > 0$ ) and creation ( $C_3 + C_4 < 0$ ) of phonons that are in non-equilibrium states [Eq. (2.28)] at  $t = 0$ . From these equations, one can see that the frequency shift is the anharmonic correction to the quasi-harmonic frequencies. Thus, the anharmonic frequency is

$$\omega_A(\boldsymbol{\kappa}) = \omega(\boldsymbol{\kappa}) + \Delta(\boldsymbol{\kappa}). \quad (2.29)$$

The linewidths are the rates at which perturbed phonon modes return to the equilibrium distribution. The linewidth is related to the relaxation time by

$$\Gamma(\boldsymbol{\kappa}) = \frac{1}{2\tau(\boldsymbol{\kappa})}. \quad (2.30)$$

With these relations, the phonon frequencies computed from quasi-harmonic LD, and the expression for the thermal conductivity derived from the Boltzmann transport equation [Eq. (2.6)] a direct calculation of the lattice thermal conductivity can be made.

## History

Much of the credit for the development of the anharmonic LD theory is given to Maradudin [55]. Prior to this work, the basics of the anharmonic LD theory had already been developed [56, 57]. Kokkedee had derived, by summing ring diagrams, the same equations as Maradudin and had published them less than a year prior [58]. What Maradudin did that was unique at the time was to both present a rigorous derivation of the method and apply it to compute properties of anharmonic crystals,



such as the phonon linewidths [55] and the Debye-Waller factor [59] in lead. Since this early work the frequency shift and linewidth due to anharmonic phonon-phonon interactions have been derived by various methods including Green’s functions [46,60], Zwanzig-Mori projection [46], and operator-renormalization [61]. This last method is presented in Appendix B.

Some early investigations of the anharmonic frequency shifts and linewidths were conducted by Koehler and Gillis [62,63] and Glyde and coworkers [64–66]. Koehler and Gillis used an interatomic potential model to obtain the third- and fourth-order derivatives of the crystal energy. They carried out calculations of the frequency shift and linewidth over a range of temperatures for several symmetry directions in aluminum and compared their results to data from neutron scattering experiments. Reasonable agreement between the calculated and experimental data was found at low temperature. Glyde and coworkers performed similar calculations for sodium, argon, and cesium with mixed results. Instead of using quasi-harmonic LD though, Glyde used a similar method known as self-consistent phonon theory to compute the normal mode vibrational frequencies. The goal of much of this early work was to test the validity of the interatomic potentials rather than investigate the effects of anharmonicity on phonons.

More recently the lifetimes of specific phonons in materials have been investigated with anharmonic LD theory and electronic structure calculations [67]. This so called density functional perturbation theory (DFPT) uses density-functional theory to compute the second- and third-order derivatives (the fourth-order derivatives are not easily found from DFPT) of the potential energy. Then the harmonic frequencies and anharmonic linewidths can be found via standard LD theory. The focus of these calculations is on semiconductors due to their technological importance and

well studied properties [68, 69]. Due to the high computational cost associated with electronic structure calculations, these studies have mostly been limited to phonon modes at  $\kappa = \mathbf{0}$ .

The first known attempt at computing the thermal conductivity from phonon lifetimes obtained with the anharmonic LD method was by Ladd [70]. Ladd used an inverse-twelfth power potential to compute the lifetimes of phonons in a generic face-centered cubic crystal. The thermal conductivity was computed with Eq. (2.11) using the classical value of the specific heat [Eq. (2.10)]. The low temperature results were found to agree well with thermal conductivity results from the Green-Kubo MD method, which is described in Section 2.4.5.

Other than the work presented here [71–73], there have been no other thermal conductivity calculations made based on the relaxation time approximation and anharmonic LD since Ladd’s study. A few thermal conductivity calculations have been performed by a similar method developed by Omini and Sparavigna [74, 75]. The method is based on an iterative solution to the linearized BTE. This different approach is taken because the RTA is better suited for elastic scattering than inelastic scattering [46], which three phonon processes are. The method requires knowledge of the phonon scattering probabilities which are typically computed with Fermi’s golden rule [27, 46, 76]. The main drawback of the iterative method is the huge computational effort required [75]. Also, those studying thermal conductivity typically rely on relaxation time arguments to explain results and develop theories of phonon transport. By bypassing the RTA, Omini and Sparavigna have developed a method that is not intuitive for those who study lattice thermal conductivity.

Omini and Sparavigna have used the iterative method to compute the thermal conductivity of argon and krypton [75] as well as silicon and germanium [77]. Broido and

coworkers have extended the method to study bulk silicon [76] and silicon/germanium superlattices [19]. Broido *et al.* have used the iterative method to compute the thermal conductivity of bulk silicon and germanium completely from first principles by obtaining all required second- and third-order force constants from DFPT calculations. These thermal conductivity predictions agree very well with experimental results between temperatures of 100 and 300 K. The LD techniques also possesses this ability to use results from DFPT as input.

### Implementation

There are two major challenges associated with implementing Eqs. (2.22) and (2.23). The first challenge is evaluating the Cauchy principal value,  $\frac{1}{(\omega)_p}$ , and Dirac delta function,  $\delta(\omega)$ . These functions are defined in terms of integrals [see Eqs. (B.61) and (B.59)], but the equations for the frequency shift and linewidth involve summations over a discrete set of wave vectors. One common way to address this challenge is to approximate the principal value and delta function by [55, 62, 64, 70]

$$\frac{1}{(\omega)_p} \approx \frac{\omega}{\omega^2 + \epsilon^2} \quad (2.31)$$

and

$$\delta(\omega) \approx \frac{1}{\pi} \frac{\epsilon}{\omega^2 + \epsilon^2}, \quad (2.32)$$

where  $\epsilon$  is a small, positive number that removes the discontinuity from the principal value and broadens the delta function. These expressions for the principal value and delta function are motivated by Eq. (B.62). The proper choice of  $\epsilon$  is important. If  $\epsilon$  is too large, the details of the phonon-phonon interactions will be washed out. If  $\epsilon$  is too small, there will not be enough interacting phonons to yield meaningful results.

In this work Eqs. (2.31) and (2.32) are used in the anharmonic LD calculations with

$$\epsilon = \Gamma(\kappa_{\nu}) + \Gamma(\kappa'_{\nu'}) + \Gamma(\kappa''_{\nu''}) \quad (2.33)$$

for all three-phonon processes. Equation (2.33) is arrived at by using the corrected phonon frequencies ( $\omega_A \pm i\Gamma$ ) in place of the quasi-harmonic frequencies ( $\omega$ ) in Eqs. (2.22), (2.23), and (2.24). This substitution couples the frequency shift and linewidth equations for all the phonon modes. These equations are solved by providing an initial guess for the frequency shift and linewidth and iterating until self-consistency is achieved. Typically, fewer than five iterations are needed to achieve a thermal conductivity prediction that changes by less than 1% upon subsequent iterations. This convergence criteria is used throughout this work.

The second challenge associated with the anharmonic LD calculations is the effect of the Brillouin zone resolution (*i.e.*,  $N$ , the number of unit cells considered). For some systems, the frequency shift and linewidth are found to be weakly dependent upon the choice of the wave vector grid. Increasing the BZ resolution to the point where this dependence is negligible is not practical for all systems. An extrapolation technique works well for removing the predicted thermal conductivity's dependence upon the wave vector grid. Lattices where  $N_1 = N_2 = N_3 = N_0$  are used to plot  $1/k$  versus  $1/N_0$ . A linear fit to the data yields the inverse of the thermal conductivity as the vertical intercept. In all cases in which this extrapolation procedure is used, the extrapolated thermal conductivity is found to be insensitive number of data points used for the linear fit.

## 2.4 Molecular dynamics simulation

### 2.4.1 Overview

The MD method is a powerful tool for examining thermal conductivity and material properties in general [78]. Molecular dynamics usually implies classical MD, as it does here. The classical MD method is based on simulating the interaction between atoms in order to extract relevant statistics about the behavior of the materials on the atomic scale. The classical MD method is dependent upon the availability of a good interatomic potential. If such an interatomic potential is known for a material, the method can yield predictions in reasonable agreement with experimental data. Given an interatomic potential, the net forces acting on an atom in a solid can be computed. Newton's laws are used to write the equations of motion for each atom, then are numerically integrated over time. The results of classical MD simulations are only valid when quantum effects can be neglected, which for thermal conductivity predictions means temperatures above about one tenth of the Debye temperature [79],  $T_{\text{Debye}}$ . In addition to classical MD there is also quantum MD. Quantum MD is essentially classical MD with an extra *ab initio* calculation to compute the energy of interaction from the electronic structure of the material instead of an interatomic potential. For this reason, quantum MD is much more computationally expensive and accurate than classical MD. Quantum MD simulation is still a classical method, however, since the nuclei obey Newtonian mechanics.

Aside from the need for a good interatomic potential, the main disadvantage of classical MD simulation is that it is computationally demanding. Though the equations of motion are deterministic, MD simulation is a statistical method. The dynamics are averaged over hundreds of thousands or millions of time steps and several different initial configurations of the atomic positions and momenta are required to give a good

statistical description of the atomic behavior. Simulating a large number of atoms over enough time steps to achieve statistically meaningful results can be difficult or even impossible depending on the computational resources available. The major advantages of the MD simulation method are that no assumptions or approximations typically need to be made (other than the interatomic potential) and the method is intuitive.

The MD method does not explicitly consider the energy carriers. Instead, phonons arise from correlated atomic motion and electrons are omitted. Determining the properties of phonons from a MD simulation requires extensive post-processing procedures. Two such procedures, normal mode analysis and the spectral energy method, are outlined in Sections 2.4.2 and 2.4.3. Both of these procedures map the atomic motion onto phonon mode coordinates, which are then used to determine the phonon properties. The thermal conductivity can then be predicted using Eq. (2.11).

Two other MD methods that are commonly employed to predict the lattice thermal conductivity are the direct and the Green-Kubo methods [80]. Neither of these methods finds the phonon properties directly. In the direct method, described in Section 2.4.4, a temperature gradient or a heat flux is imposed on a sample and the conductivity is found by Fourier's law. The Green-Kubo method, described in Section 2.4.5, relies upon the fluctuation dissipation theorem and correlation relations to determine the thermal conductivity purely through energy fluxes in a system at equilibrium and a uniform temperature. If used properly, the direct and Green-Kubo methods have been shown to produce equivalent results [80,81] so either method can be used when most appropriate.

### 2.4.2 Normal mode analysis

The first step in the MD normal mode analysis is to determine the non-interacting phonon frequencies and polarization vectors from a quasi-harmonic LD calculation (see Section 2.3.1). Molecular dynamics simulations are then used to calculate the time-dependent normal mode coordinates from Eq. (2.18). Next, the time-dependent energy of each quasi-harmonic oscillator is found from

$$E_{\kappa,\nu}(t) = \frac{\omega^2(\nu) q^*(\nu) q(\nu)}{2} + \frac{\dot{q}^*(\nu) \dot{q}(\nu)}{2}, \quad (2.34)$$

where the first and second terms on the right hand side are the potential and kinetic energies.

The autocorrelation of the phonon energy can be shown to be related to the phonon relaxation time through [70]

$$\exp[-t/\tau(\nu)] = \frac{\langle E_{\kappa,\nu}(t) E_{\kappa,\nu}(0) \rangle}{\langle E_{\kappa,\nu}(0) E_{\kappa,\nu}(0) \rangle}, \quad (2.35)$$

where the angle brackets denote an ensemble average, which for an ergodic system is equivalent to a time average. An exponential decay is fit to the normalized energy autocorrelation to extract the relaxation time. The anharmonic frequencies are determined from the autocorrelation of the phonon potential energy which gives a decaying function that oscillates with a period that is  $\pi$  divided by the anharmonic phonon frequency.

### 2.4.3 Spectral energy density

The spectral energy density method is similar to normal mode analysis in that the motion of the atoms is mapped onto the phonon mode coordinates. Unlike in the normal mode analysis, however, the phonon frequencies and polarization vectors do not need to be known *a priori*. The spectral energy density,  $\Phi(\kappa, \omega_0)$ , is defined

as [82, 83]

$$\Phi(\boldsymbol{\kappa}, \omega_0) = \frac{1}{4\pi\tau_0 N} \sum_b m_b \sum_\alpha \left| \int_0^{\tau_0} \sum_l \dot{u}_\alpha^{(l)} \exp[i\boldsymbol{\kappa} \cdot \mathbf{r}_b^{(l)} - i\omega_0 t] dt \right|^2, \quad (2.36)$$

where the atomic displacements,  $\dot{\mathbf{u}}$ , are time dependent but the, equilibrium atomic positions,  $\mathbf{r}$ , are not.

It can be shown that the spectral energy density is a highly peaked function [83]. These peaks are centered at values of  $\boldsymbol{\kappa}$  and  $\omega_0$  at which phonons exist. If the weakly interacting phonon picture is valid (*i.e.*, weak anharmonicity), the peaks are Lorentzian in form and

$$\Phi(\boldsymbol{\kappa}, \omega_0) = \frac{C}{(\omega - \omega_0)^2 + (2\tau)^{-2}}, \quad (2.37)$$

where  $C$  is a constant defining the height of the peak. The phonon frequency,  $\omega$ , and relaxation time,  $\tau$ , determined through the spectral energy density naturally incorporate the full anharmonicities of the material.

In practice, the wave vectors for the phonon modes are known based on the crystal structure. Thus, the spectral energy density is computed for a range of frequencies at the known wave vectors. Then Lorentzian functions are fit to the spectral energy density at each wave vector and the phonon frequencies and relaxation times are extracted. For complicated unit cells, where many phonons exist at each wave vector, harmonic LD calculations may be needed to identify the degenerate or closely spaced phonon modes [82].

#### 2.4.4 Direct method

The direct MD method is a non-equilibrium method that invokes the definition of the thermal conductivity in an intuitive way in order to predict it. From the Fourier law, there are two possible ways of determining the thermal conductivity. One is to



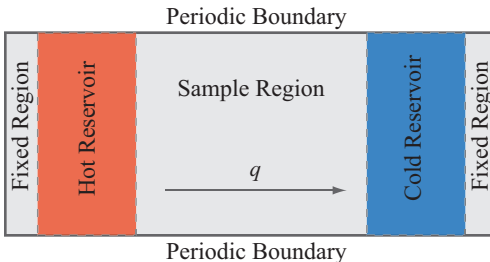


Figure 2.1: Schematic diagram of the simulation cell used in the direct MD thermal conductivity prediction method.

apply a temperature gradient to a sample and measure the resulting heat flux. The other option is the converse; apply a heat flux and measure the resulting temperature drop. These are the ways that thermal conductivity is measured experimentally. The difference in the MD simulation is that the sample size is generally much smaller in the simulation than it is in the experiment.

When computing the thermal conductivity with the direct MD method, a simulation cell is setup, as indicated in Fig. 2.1, such that its length is much larger than its width and height. Periodic boundary conditions are imposed along the directions of the width and height [41, 80, 84, 85]. The cell is then divided along its length into several regions. Two of the regions are heat/energy reservoirs. Energy is added to the “hot” reservoir and subtracted from the “cold” reservoir so that a net amount of energy flows from the “hot” region to the “cold” region through the center region. The resulting heat flux and temperature gradient can be measured and used to determine the thermal conductivity using the Fourier law. Two additional regions of fixed atoms on either side of the simulation domain prevent sublimation of atoms from the ends of the reservoirs.

The direct MD method has the advantage of using the definition of the thermal conductivity in an intuitive way in order to calculate it. Another advantage of the

direct method is that it can be used without modification to study the heat flux across boundaries such as crystal grains or material interfaces. Disadvantages include nonlinear temperature gradients near the hot and cold regions and nonphysically large heat fluxes due to the small size of the system. Also, eliminating size effects in the direct method often requires a prohibitively large simulation domain. Therefore, the bulk thermal conductivity for a macroscopic crystal has to be extrapolated from a series of simulations with manageable domains [80, 84]. However, Sellan *et al.* [81] have shown that this extrapolation technique can be inaccurate for systems much shorter than the effective phonon mean free path.

#### 2.4.5 Green-Kubo method

The Green-Kubo method uses fluctuations in the heat current to compute the thermal conductivity. The basis of the Green-Kubo method is the Green-Kubo formula [80],

$$\underline{k} = \frac{1}{Vk_B T^2} \lim_{\tau_0 \rightarrow \infty} \int_0^{\tau_0} \langle \mathbf{S}^*(t) \mathbf{S}(0) \rangle dt, \quad (2.38)$$

where  $V$  is the volume,  $k_B$  is Boltzmann's constant, and  $*$  denotes the transpose. The time dependent heat current is given by

$$\mathbf{S}(t) = \frac{d}{dt} \sum_i \mathbf{r}_i(t) \phi_i(t), \quad (2.39)$$

for the position,  $\mathbf{r}$ , and energy,  $\phi$ , of the  $i^{\text{th}}$  atom. The brackets denote the ensemble average. In this case the ensemble average is the heat current autocorrelation function [78],

$$\langle \mathbf{S}^*(t) \mathbf{S}(0) \rangle = \int_0^t \mathbf{S}^*(t_0) \mathbf{S}(t_0 + t) dt_0. \quad (2.40)$$

Information from equilibrium MD simulations can be used to evaluate these expressions.

The advantages of predicting the thermal conductivity with MD and the Green-Kubo method are that it is an equilibrium method and size effects are not as pronounced as they are in the direct method. By measuring fluctuations there is no need to prescribe a special geometry or interfere with the dynamics of the particles in any way. With periodic boundary conditions, domain sizes can generally be made large enough that size effects are small [86]. The main drawback of the Green-Kubo method is the large amount of averaging required to obtain meaningful results. Insufficient data averaging leads to large errors due to numerical noise [85].

## CHAPTER III

### Comparison of atomic level models: Phonon transport in bulk materials

#### 3.1 Preliminaries

In this Chapter, quasi-harmonic and anharmonic LD calculations and normal mode analysis from MD simulations are used to predict the phonon properties of crystalline argon. A detailed comparison is made of the phonon properties predicted by these two methods and the validity of the low temperature approximations made in the LD calculations is discussed. The phonon properties are then used in the BTE to compute the thermal conductivity due to phonon transport. These thermal conductivity predictions are compared to predictions made using MD simulations and the Green-Kubo and direct methods. In addition to presenting the thermal conductivities predicted by each method, the phonon properties obtained by the LD calculations are used to identify which phonons dominate thermal transport. For brevity, these four prediction methods will be referred to as the BTE-LD, BTE-MD, GK-MD, and direct-MD methods.

The argon system is examined at temperatures ranging from 20 K to 80 K at 10 K increments. Argon is an insulating, face-centered cubic crystal up to its experimentally-observed melting temperature of 84 K [87]. The interactions between the argon atoms

are modeled with the 12-6 Lennard-Jones (LJ) potential, which gives the energy between a pair of atoms  $i$  and  $j$  as

$$\phi_{ij}(r_{ij}) = 4\epsilon_{\text{LJ}} \left[ \left( \frac{\sigma_{\text{LJ}}}{r_{ij}} \right)^{12} - \left( \frac{\sigma_{\text{LJ}}}{r_{ij}} \right)^6 \right], \quad (3.1)$$

where  $r_{ij}$  is the distance between the two atoms and the energy and length scales for argon are  $\epsilon_{\text{LJ}} = 1.67 \times 10^{-21}$  J and  $\sigma_{\text{LJ}} = 3.40 \times 10^{-10}$  m [47]. Argon is chosen as a test material because it is extensively studied and can be modeled with a simple two-body interatomic potential [39, 41, 42, 88]. The methodologies presented herein can also be applied to more complex, technologically relevant insulators and semiconductors provided that a suitable interatomic potential is available.

To best compare with the results of the MD prediction methods, the BTE-LD thermal conductivity predictions and all other calculations presented in this Chapter are made in the classical limit unless otherwise noted. The four-atom conventional unit cell is considered so that a simple cubic lattice may be used. The temperature-dependent lattice parameters,  $a$ , used are those from MD simulations reported by McGaughey [89] and the cutoff radius is set to  $2.5\sigma_{\text{LJ}}$  for the quasi-harmonic calculations and  $1.5\sigma_{\text{LJ}}$  (nearest neighbors) for the anharmonic LD calculations. Using the smaller cutoff in the anharmonic calculation changes the calculated frequency shifts and linewidths by less than 7% and the thermal conductivity by less than 2%, while reducing the computational effort by one third. The BTE-LD thermal conductivity values are found from the extrapolation procedure described in Section 2.3.2 using  $N_0 \times N_0 \times N_0$  lattices with  $N_0=6, 8, 10$ , and 12. The extrapolation to the thermal conductivity value at a temperature of 50 K is shown in Fig. 3.1. Performing the extrapolation with any four of the points shown in Fig. 3.1 changes the thermal conductivity by at most  $\pm 1.5\%$ .

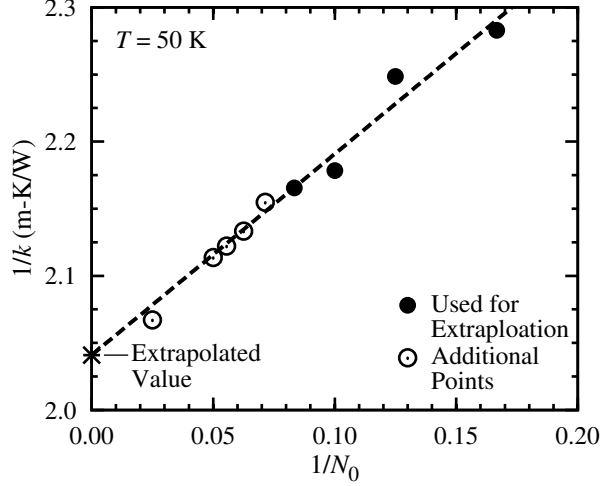


Figure 3.1: Linear extrapolation from LD-based predictions of  $1/k$  versus  $1/N_0$  at a temperature of 50 K. The line is fit to the four rightmost (filled) circles only. Reprinted with permission from [71]. Copyright *Physical Review B* 2009.

For the BTE-MD method, the MD simulations are performed using the velocity Verlet integration algorithm with a time step of 4.3 fs and a radius of  $2.5\sigma_{\text{LJ}}$  is used for the interatomic potential cutoff. The system is equilibrated for a period of  $10^5$  time steps after which the normal mode coordinates and their derivatives are computed every fifth time step for an additional  $2 \times 10^6$  time steps. The anharmonic frequency and lifetime are determined for every phonon in the irreducible Brillouin zone [46] and averaged over five independent simulations. Like in the BTE-LD method, the thermal conductivity predicted from the BTE-MD method is found to depend on the number of wave vectors. In the same manner as the BTE-LD method, this dependence is removed by extrapolating to an infinite number of wave vectors using  $N_0 \times N_0 \times N_0$  lattices with  $N_0=4, 6, 8$ , and 10.

Table 3.1: Root mean square displacements scaled by the nearest neighbor distance from the BTE-LD and BTE-MD methods. The data in the rightmost column are RMS displacements found directly from a time average of the atomic positions in MD simulations [89].

T (K)	$\frac{\langle u_{LD}^2 \rangle^{1/2}}{a/\sqrt{2}}$	$\frac{\langle u_{MD}^2 \rangle^{1/2}}{a/\sqrt{2}}$	$\frac{\langle u^2(\mathbf{r}) \rangle^{1/2}}{a/\sqrt{2}}$
20	0.047	0.048	0.048
30	0.059	0.060	0.065
40	0.070	0.072	0.081
50	0.080	0.083	0.10
60	0.091	0.096	0.12
70	0.10	0.11	0.15
80	0.11	0.13	0.18

### 3.2 Comparison and validation of the Boltzmann transport equation-based methods

As noted in Section 2.3, for the quasi-harmonic and anharmonic LD calculations to be valid: (i) the atomic displacements must be small compared to the atomic spacing, and (ii) the frequency shift and linewidth must be small compared to the quasi-harmonic frequencies. The first condition affects both the BTE-LD and BTE-MD methods since they both rely on quasi-harmonic LD calculations. The second condition also applies to both methods as the BTE-LD method uses anharmonic LD calculations directly and the BTE-MD method requires the phonon modes to be well described by Eq. (2.18). The BTE-MD method is expected to be more accurate than the BTE-LD method at all temperatures because the MD simulations include the full anharmonicity of the interatomic potential while the anharmonic LD calculation only considers up to four-phonon interactions. The BTE-based methods should converge at low temperature where the approximations made in the LD techniques are accurate.

Table 3.1 contains the classical BTE-LD- and BTE-MD-predicted root mean square (RMS) displacements [90],

$$\langle u^2 \rangle^{1/2} = \left[ \frac{\hbar}{nN} \sum_{\alpha,b}^{3,n} \sum_{\kappa,\nu}^{N,3n} f(\kappa_\nu) \frac{e(\kappa_\nu b) e^*(\kappa_\nu b)}{m_b \omega_A(\kappa_\nu)} \right]^{1/2}, \quad (3.2)$$

scaled by the nearest-neighbor distance,  $a/\sqrt{2}$ . Also tabulated in Table 3.1 are the scaled RMS displacements,  $\langle u^2(\mathbf{r}) \rangle^{1/2}/(a/\sqrt{2})$ , found directly from the time average of the atomic positions in MD simulations [89]. At a temperature of 20 K the atomic displacements from the BTE-based methods are in excellent agreement with the formally exact value obtained from MD simulation. At a temperature of 40 K the BTE-LD-predicted RMS displacement is 14% smaller than the value obtained directly from MD and becomes increasingly inaccurate at higher temperatures. The RMS displacements calculated from the BTE-MD method are more accurate than the BTE-LD-predicted values but also lose accuracy at higher temperatures.

The frequency shifts and inverse lifetimes at temperatures of 20 K and 50 K are plotted versus wave vector in the [100] direction in Figs. 3.2(a)-3.2(d). For the BTE-MD method, predictions are made using (i) the full LJ potential, and (ii) a Taylor series expansion of the LJ potential truncated after the fourth-order term. The frequency shifts [Figs. 3.2(a) and 3.2(b)] and inverse lifetimes [Figs. 3.2(c) and 3.2(d)] computed with the BTE-LD method and the BTE-MD method (using the full and truncated LJ potential) are in good agreement at a temperature of 20 K where the low-temperature approximations are valid (see Table 3.1). The results from the BTE-MD method using the full LJ potential at both temperatures are in good agreement with the frequency shifts and relaxation times found by McGaughey and Kaviani [39,91].

At a temperature of 50 K the fifth- and higher-order terms in the potential energy expansion become important. The effect of these terms is evident in the clear



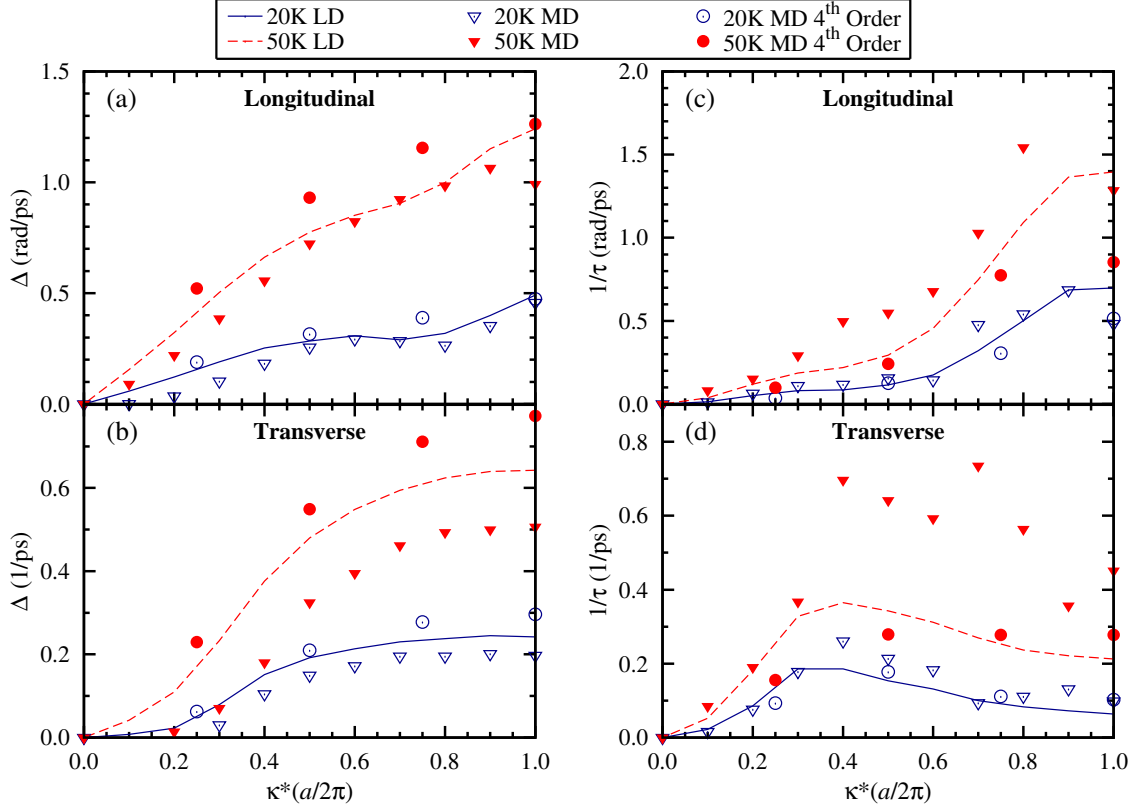


Figure 3.2: Frequency shift ( $\Delta$ ) and inverse of the lifetime ( $1/\tau$ ) at temperatures of 20 K and 50 K versus reduced wave vector for the longitudinal and transverse dispersion branches in the [100] direction. The MD data is found using (i) the full LJ potential, and (ii) the LJ potential truncated after the fourth-order term in the Taylor series expansion. While the results from the LD calculations are discrete, we plot the data as lines for clarity. Reprinted with permission from [71]. Copyright *Physical Review B* 2009.

Table 3.2: Root mean square anharmonic frequency shifts and linewidths ( $\Gamma = 1/2\tau$ ) normalized by the quasi-harmonic frequencies from the BTE-LD and BTE-MD methods.

T (K)	$\langle \frac{\Delta_{LD}^2}{\omega^2} \rangle^{1/2}$	$\langle \frac{\Delta_{MD}^2}{\omega^2} \rangle^{1/2}$	$\langle \frac{\Gamma_{LD}^2}{\omega^2} \rangle^{1/2}$	$\langle \frac{\Gamma_{MD}^2}{\omega^2} \rangle^{1/2}$
20	0.029	0.023	0.013	0.014
30	0.048	0.039	0.020	0.025
40	0.069	0.056	0.028	0.037
50	0.094	0.074	0.035	0.054
60	0.13	0.096	0.043	0.078
70	0.16	0.12	0.051	0.11
80	0.22	0.15	0.059	0.16

differences between the results from the BTE-MD calculations using the full LJ potential and the truncated potential (circles and triangles). The frequency shifts and lifetimes calculated using the BTE-MD method with the full LJ potential are the most accurate. The truncated potential is less anharmonic than the full potential, resulting in longer phonon lifetimes. The results from the BTE-LD method (in which the potential energy is truncated after the fourth-order term) are generally in good agreement with the results from the BTE-MD method using the truncated potential. The discrepancies between these two methods can be attributed to the fact that the anharmonic LD equations [Eqs. (2.22) and (2.23)] include only first- and second-order perturbations. Using a constant value for  $\epsilon$  in the anharmonic LD calculations (as is done by others [55, 70]) instead of the iterative procedure described in Section 2.3.2 yields frequency shifts and linewidths that are in poor qualitative agreement with those computed with MD, particularly at the higher temperatures.

Listed in Table 3.2 are the RMS frequency shift and linewidth normalized by the quasi-harmonic frequencies over the entire Brillouin zone,  $\langle (\Delta/\omega)^2 \rangle^{1/2}$  and  $\langle (\Gamma/\omega)^2 \rangle^{1/2}$ . At a temperature of 20 K, the normalized anharmonic frequency shifts, as calculated with the BTE-LD and BTE-MD methods, are in reasonable agreement with

each other. The linewidths calculated with the two methods are also in agreement. At this temperature, these anharmonic corrections are small compared to the quasi-harmonic frequencies, but grow with increasing temperature. Above a temperature of 50 K, the anharmonic corrections become significant compared to the quasi-harmonic frequencies and the BTE-based methods may no longer be accurate. At all temperatures considered, the linewidths predicted in the BTE-MD method are larger than those predicted in the BTE-LD method. This result is expected since fifth- and higher-order anharmonic terms are neglected in the BTE-LD method but not in the BTE-MD method.

### 3.3 Thermal conductivity predictions

The predicted thermal conductivities from the four methods are plotted against temperature in Fig. 3.3 and listed in Table 3.3. Unlike the BTE-LD and BTE-MD prediction methods, there are no major assumptions inherent to the GK-MD and direct-MD methods other than the choice of the interatomic potential, which is consistent here. Thus, the GK-MD and direct-MD thermal conductivity predictions are taken to be the most accurate and are used to assess the range of applicability of the BTE-LD and BTE-MD methods. The predicted thermal conductivity values from the GK-MD and direct-MD methods are in good agreement, generally within 10% (except at temperatures of 20 K and 60 K where the predictions are within 15%). Others have also found that GK-MD and direct-MD thermal conductivity predictions are consistent [80,81,85]. The thermal conductivities predicted with the BTE-LD and BTE-MD methods are within 15% of both the GK-MD and direct-MD values at a temperature of 20 K. As the temperature increases, the BTE-MD method begins to under-predict the thermal conductivity by an increasing amount. This loss

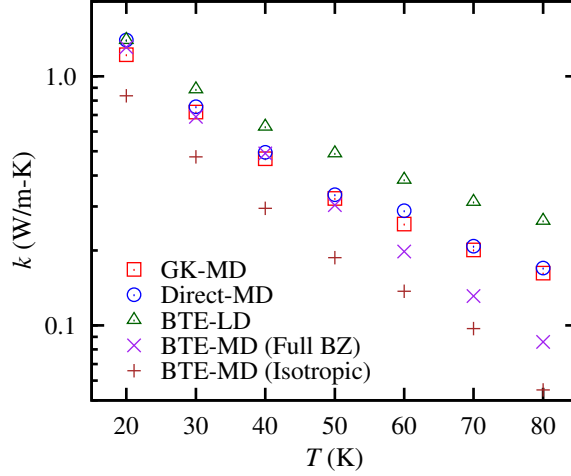


Figure 3.3: Temperature dependence of the thermal conductivity predicted from the four methods. Using an isotropic approximation (Isotropic) rather than all the phonons in the full Brillouin zone (Full BZ) in the BTE-MD method causes the thermal conductivity to be under-predicted by a factor of about 1.5. Reprinted with permission from [71]. Copyright *Physical Review B* 2009.

of accuracy is due to error introduced by mapping the atomic positions and velocities onto the quasi-harmonic normal mode coordinates, which become less representative of the real system as the temperature increases. As the temperature increases above 20 K, the BTE-LD method begins to over-predict the thermal conductivity by an increasing amount. This over-prediction can be attributed to the exclusion of higher-order phonon processes resulting in reduced anharmonicity of the argon crystal (see Fig. 3.2). The BTE-LD thermal conductivity value at a temperature of 40 K is about 30% higher than the GK-MD and direct-MD predictions.

The thermal conductivity predictions using the BTE-LD method with the quantum mechanical expressions for the phonon distribution, specific heats, frequency shifts, and linewidth are also given in Table 3.3. While not shown here (see Chapter VI), the full quantum mechanical treatment correctly captures the expected thermal conductivity trends at very low temperatures, including the experimentally-observed maximum in the thermal conductivity and the decrease to zero at zero temperature.

Table 3.3: Thermal conductivity values in W/m-K from the four prediction methods. The BTE-LD values computed using the quantum expressions for the occupation number and specific heat are included for reference.

T (K)	GK-MD [89]	Direct-MD	BTE-MD	BTE-LD	Quantum BTE-LD
20	1.2	1.4	1.3	1.4	1.5
30	0.72	0.76	0.69	0.89	0.93
40	0.47	0.50	0.49	0.63	0.66
50	0.32	0.34	0.30	0.49	0.51
60	0.26	0.29	0.20	0.38	0.40
70	0.20	0.21	0.13	0.31	0.32
80	0.16	0.17	0.086	0.26	0.27

These low-temperature predictions cannot be made using MD because it is a classical method. As expected, above the maximum in the thermal conductivity, the quantum predictions closely agree with the classical BTE-LD predictions. These quantum BTE-LD thermal conductivity results agree to within 15% of the BTE-based quantum predictions made by Omini and Sparavigna for argon at temperatures of 20 K (1.66 W/m-K) and 80 K (0.236 W/m-K) [75].

Based on the thermal conductivity results in this section and the analysis in section 3.2, it is suggested that, for LJ argon, reasonable quantitative predictions of the thermal conductivity can be made up to half the Debye temperature (40 K) with the BTE-LD method and up to 70% of the Debye temperature with the BTE-MD method. From these thermal conductivity results and the BTE-LD thermal conductivity predictions of Stillinger-Weber silicon in Chapter VI, it is proposed that, as a general rule, the BTE-LD predictions are accurate up to one-half of the Debye temperature.

The computational cost of each of the prediction methods is a major concern. For the test argon system, the GK-MD and direct-MD prediction methods require

similar computational resources ( $\approx 10$ -20 processor hours for each temperature). The computation time required for the BTE-LD method is an order of magnitude less ( $\approx 1$  processor hour for each temperature) while the BTE-MD method is extremely demanding ( $\approx 25$  processor days for each temperature). Efficient MD codes scale linearly with the number of atoms in the computational domain; thus, so do the GK-MD and direct-MD methods. The BTE-MD method scales as the square of the number of atoms  $[(Nn)^2]$ . The computational cost of the BTE-LD method is proportional to  $N^2n^4$ . This poor scaling makes the BTE-LD method computationally expensive for materials with a large number of atoms in the unit cell.

For the BTE-LD method, it is possible to make several approximations that will reduce the computational cost required without sacrificing much accuracy. One such approximation is used here when the interactions beyond nearest neighbors are neglected in the anharmonic LD calculations. Other possible approximations include neglecting high frequency phonons, which make little contribution to the thermal conductivity, (*i.e.*, do not calculate  $\Delta$  or  $\Gamma$  for frequencies greater than some cutoff) or by using a single, coarse, wave vector grid to compute the thermal conductivity (*i.e.*, do not perform the extrapolation). Using a  $6 \times 6 \times 6$  grid of wave vectors gives thermal conductivity values that are at most 15% lower than the extrapolated values but with 2% of the computational cost ( $\approx 1.5$  minutes).

### 3.4 Mode-dependent thermal conductivity

Using the BTE-MD method and an isotropic approximation (similar to the method described by McGaughey and Kaviani [39] and Henry and Chen [92]), the thermal conductivities for LJ argon are predicted. These predictions are about a factor of 1.5 lower than the predictions using the full BZ (see Fig. 3.3). This discrepancy is a

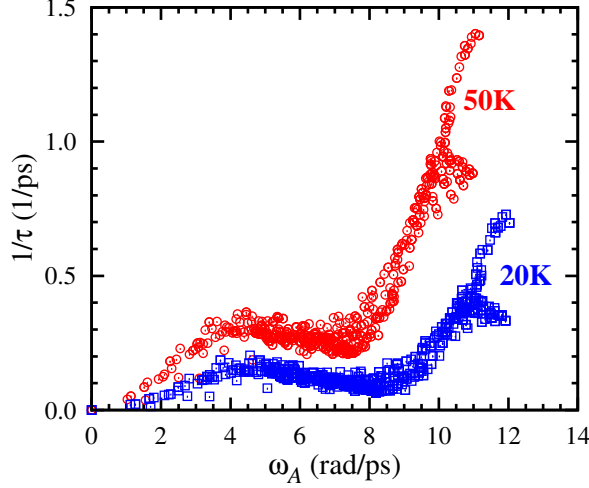


Figure 3.4: Inverse relaxation time versus frequency as predicted by the BTE-LD method for temperatures of 20 and 50 K.

result of the inaccuracy of the isotropic approximation for LJ argon. The inverse of the relaxation times predicted by the BTE-LD method are plotted against frequency in Fig. 3.4 at temperatures of 20 and 50 K. At each temperature, the relaxation times cluster along a single, frequency dependent path. The relaxation time predictions of the BTE-MD method show a similar frequency dependence. Thus, the relaxation times can be treated isotropically (*i.e.*, as a function of only frequency and temperature). It is found, however, that the distribution of phonons and the group velocities in the [100] direction are not representative of the entire BZ.

The contribution to the thermal conductivity as a function of the phonon frequency divided by the maximum phonon frequency,  $\omega_A/(\omega_A)_{max}$ , is plotted in Fig. 3.5 from the phonon information obtained from the BTE-LD method. For this classical system, temperature changes the maximum frequency but has no effect on the curves in Fig. 3.5. The largest contribution to the thermal conductivity comes from the phonons around half of the maximum frequency. This large contribution is due to the large number of phonons near that frequency (see the density of states curve in Fig. 3.5).

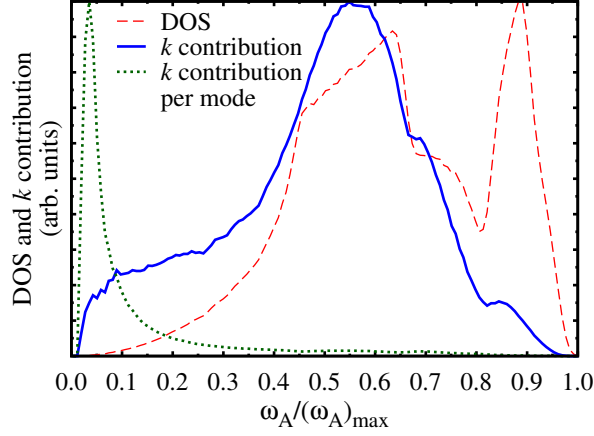


Figure 3.5: Dependence of the thermal conductivity and phonon DOS on  $\omega_A/(\omega_A)_{max}$  at a temperature of 50 K. Reprinted with permission from [71]. Copyright *Physical Review B* 2009.

Dividing the thermal conductivity contribution by the density of states gives the average contribution per mode ( $c_{ph}v_{g,x}^2\tau$ ) as a function of frequency ratio. On average, each low frequency mode contributes much more than individual phonons at the higher frequencies (the downturn near zero frequency is due to the finite number of unit cells considered). This fact leads to a common assumption that low-frequency phonons dominate thermal transport. However, this assumption is clearly not valid for LJ argon.

### 3.5 Conclusions

The thermal conductivity predictions made with the BTE-based methods were compared to predictions made using the GK-MD and direct-MD methods. All of the prediction methods give thermal conductivity values for LJ argon that agree at low temperature (20 K). As the temperature is increased, the BTE-LD and BTE-MD predictions diverge from the GK-MD and direct-MD predictions (see Fig. 3.3) due to reduced validity of the low-temperature approximations made in the LD calculations. By analyzing the phonon velocities, frequencies, and lifetimes, it is found that the



isotropic approximation is invalid for argon. Further analysis reveals that on a per mode basis the low frequency phonons contribute the most to the thermal conductivity. However, as shown in Fig. 3.5, by considering the phonon density of states, phonons with a frequency of half the maximum frequency are found to dominate thermal transport. Such information will be valuable in designing nano-structures with tailored thermal properties.

By considering the RMS displacements, frequency shifts, and linewidths, it is suggested that the LD calculations for LJ argon are reasonably accurate up to a temperature of 50 K (see Section 3.2). At this temperature, the BTE-MD predicted thermal conductivity value is about 10% lower than the GK-MD and direct-MD values. For the BTE-LD method, neglecting fifth- and higher-order potential energy terms causes the thermal conductivity predictions to become inaccurate above a temperature of 40 K. At this temperature, the BTE-LD thermal conductivity prediction is about 30% higher than the GK-MD and direct-MD predictions. For other insulators and semiconductors, it is suggested that half the Debye temperature is the maximum temperature at which the BTE-LD method provides accurate thermal conductivity predictions while the BTE-MD method is accurate up to 70% of the Debye temperature. Above these temperatures the approximations made in the BTE-based methods become inaccurate and the GK-MD and direct-MD prediction methods are more appropriate to use.

To make the thermal conductivity predictions the BTE-LD method requires an order of magnitude less computing effort than the GK-MD and direct-MD methods. Additionally, several approximations can be made within the LD framework that allow the thermal conductivity to be estimated using the BTE-LD method in a matter of minutes. For designing materials with tailored thermal transport properties, the

ability to rapidly estimate the thermal conductivity will be a useful way to screen for promising designs that deserve more in-depth study.

## CHAPTER IV

### Extending lattice dynamics to finite/heterogeneous structures: Thin films and superlattices

#### 4.1 Introduction

The thermal transport properties of micro- and nano-structures can be significantly different than those of the corresponding bulk material. Two such structures are thin films and superlattices. Thin films are thin ( $\sim 100$  nm or less) layers of a material, typically deposited on a substrate. Superlattices are essentially multiple thin films of different materials deposited one atop another to form a periodic, layered structure. Thin films are commonly used in semiconductor laser [93], solar energy conversion [94,95], and solid state lighting devices [96]. The main thermal application for superlattices is in thermoelectric energy conversion devices [3,12,97]. Experimental measurements show that the in-plane thermal conductivities of sub-micron thin films and cross-plane thermal conductivities in superlattices can be several factors lower than the thermal conductivity of the corresponding bulk materials [2,6,98]. This reduction can be problematic in devices where efficient heat removal is key to reliability (*e.g.*, lasers), but beneficial when a low thermal conductivity is desired, such as in a thermoelectric energy conversion device.

The thermal conductivity reduction in a thin film or a superlattice is caused by phonon scattering at the boundaries and interfaces. For very thin films and short period superlattices (*i.e.*, thin individual layers), the phonon populations are also affected, leading to phonon DOS that differ from the bulk DOS [6,14,99]. Analytical, carrier-level models, typically based on the Holland phonon relaxation time model and the Boltzmann transport equation, have been developed to try to understand the experimentally-observed relationship between film thickness and thermal conductivity [33–36] or period length and thermal conductivity [99,100]. These models, however, obscure the underlying phonon physics because they rely on fitting parameters and assume isotropic phonon properties. Studies of thin films and superlattices using MD simulation [13,14,20,85,101,102], while confirming the thermal conductivity reduction, have not been able to elucidate the underlying phonon-level mechanisms. While MD simulations can be used to predict phonon transport properties in bulk materials [39,70,71,92,103], it is unclear how the available techniques can be applied to systems with interfaces or boundaries.

In this Chapter, procedures for predicting the in-plane phonon thermal conductivity of thin films and the in-plane and cross-plane thermal conductivities of superlattices using LD calculations are presented. These procedures use the properties of all the phonons in the Brillouin zone and do not rely upon fitting parameters. In Section 4.2 the in-plane thermal conductivities of thin films of LJ argon [47] and Stillinger-Weber (SW) silicon [104] are predicted and found to agree with MD-based predictions and experimental results. It is also found that the average of the bulk phonon mean free path cannot be used in simple models to predict the thermal conductivity reduction in thin films, as suggested by others [105,106]. Mode-dependent phonon properties, as used in this work, are required. Section 4.3 is devoted to pre-

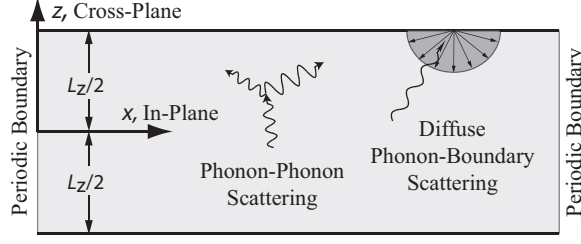


Figure 4.1: Schematic diagram of the thin film. The film is finite in the  $z$  direction (terminating in free surfaces) and periodic in the  $x$  and  $y$  directions.

dicting the in-plane and cross-plane thermal conductivities of ideal LJ superlattices. The in-plane and cross-plane thermal conductivities for short period superlattices are adequately modeled using the LD model. However, the cross-plane thermal transport in long period superlattices is not modeled properly with LD because LD treats the entire superlattice as a single material and enforces coherent phonon transport across the material layers.

## 4.2 In-plane phonon transport in thin films

### 4.2.1 Computational framework

Consider a thin film oriented such that the cross-plane direction is along the  $z$ -axis, as shown in Fig. 4.1. Here, thin films of LJ [47] argon with thicknesses ranging from 4.3 to 540 nm and SW [104] silicon with thicknesses ranging from 17.4 to 71,200 nm are considered. The films are oriented with the cross-plane direction parallel to the [001] crystallographic direction. The in-plane phonon thermal conductivity (*i.e.*, the thermal conductivity in the  $x$  or  $y$  direction) is predicted for the LJ argon thin films at a temperature of 20 K and for the SW silicon thin films at temperatures of 400 K, where predictions from classical MD simulations are available for comparison. Stillinger-Weber silicon thin films are also modeled at a temperature of 300 K, for which experimental data is available.

The in-plane phonon thermal conductivity,  $k$ , can be predicted from Eq. (2.11). However, because a thin film has a finite thickness, LD calculations will only predict the existence of standing waves in the cross-plane direction. These standing waves do not transport energy (*i.e.*, they are non-propagating phonons). The scenario where no phonons propagate in the cross-plane direction is non-physical. For very thick films, the phonon properties should approach those in a bulk crystal, where phonons propagate in all directions. Due to this issue, LD calculations cannot be used to predict the phonon properties of a thin film directly.

To predict the thermal conductivity of a thin film, LD calculations are first used to predict bulk phonon properties. For argon films, a lattice constant,  $a$ , of 5.32 Å is used [39], while 5.43 Å is used for silicon [103]. For both materials, the bulk phonon properties are determined using  $32 \times 32 \times 32$  conventional unit cells and periodic boundaries applied in all three Cartesian directions. This Brillouin zone resolution is fine enough that increasing it does not appreciably change the bulk thermal conductivity predictions.

The effect of the boundaries are included by: (i) only considering phonons with wavelengths that fit within the film, and (ii) adjusting the relaxation times to account for boundary scattering. The constraint on the wavelength, which is inversely proportional to the wave vector magnitude, is expressed in terms of the cross-plane component of the wave vector,  $\kappa_z$ . This constraint can be written as

$$\kappa_z = \frac{2\pi l_z}{aN_z}, \quad (4.1)$$

where  $N_z$  is the number of unit cells in the cross-plane direction and  $l_z$  is an integer whose magnitude is less than  $N_z/2$ . The thickness of the film,  $L_z$ , is equal to  $aN_z$ . Equation (4.1) also gives the valid wave vectors in the bulk system, where  $N_z = 32$ .

In the thin films,  $N_z$  must be a factor or multiple of  $N_z$  in the bulk calculation. Otherwise, Eq. (4.1) gives wave vectors that are not found in the bulk system. Here, films with  $N_z = 2^j$  are considered, where  $j$  is a non-negative integer. Thus using this model, the bulk phonon properties ( $c_{ph}$ ,  $v_{g,x}$ ,  $\tau_{p-p}$ ) only need to be computed once for each combination of material and temperature.

Boundary scattering is accounted for by setting

$$\tau(\boldsymbol{\kappa}) = F(\boldsymbol{\kappa}) \tau_{p-p}(\boldsymbol{\kappa}), \quad (4.2)$$

where  $F$  is a mode-dependent scaling factor given by

$$F(\boldsymbol{\kappa}) = 1 - \frac{1 - p(\boldsymbol{\kappa})}{\delta(\boldsymbol{\kappa})} \frac{1 - \exp[-\delta(\boldsymbol{\kappa})]}{1 - p(\boldsymbol{\kappa}) \exp[-\delta(\boldsymbol{\kappa})]}. \quad (4.3)$$

Here,  $p(\boldsymbol{\kappa})$  is the specular parameter and  $\delta(\boldsymbol{\kappa}) \equiv L_z / (|v_{g,z}(\boldsymbol{\kappa})| \tau_{p-p}(\boldsymbol{\kappa}))$ , with  $v_{g,z}$  being the cross-plane ( $z$ ) component of the phonon group velocity. Note that  $\delta(\boldsymbol{\kappa})$  is the ratio of the film thicknesses to the  $z$  component of the phonon mean free path in bulk. The specular parameter is the probability that a particular phonon mode will reflect off the boundary. It ranges from zero for completely diffuse scattering to unity for completely specular scattering. In Appendix C, Eqs. (4.2) and (4.3) are derived from the Boltzmann transport equation under the relaxation time approximation.

Under the additional assumption that the boundary scattering is independent of the phonon-phonon scattering, the Matthiessen rule can be used to write [27, 46]

$$\frac{1}{\tau_M(\boldsymbol{\kappa})} = \frac{1}{\tau_{p-p}(\boldsymbol{\kappa})} + \frac{1}{\tau_b(\boldsymbol{\kappa})}, \quad (4.4)$$

where  $\tau_M$  is the effective relaxation time and the boundary scattering relaxation time is given by

$$\tau_b(\boldsymbol{\kappa}) = \frac{1 + p(\boldsymbol{\kappa})}{1 - p(\boldsymbol{\kappa})} \frac{L_z}{2|v_{g,z}(\boldsymbol{\kappa})|}. \quad (4.5)$$

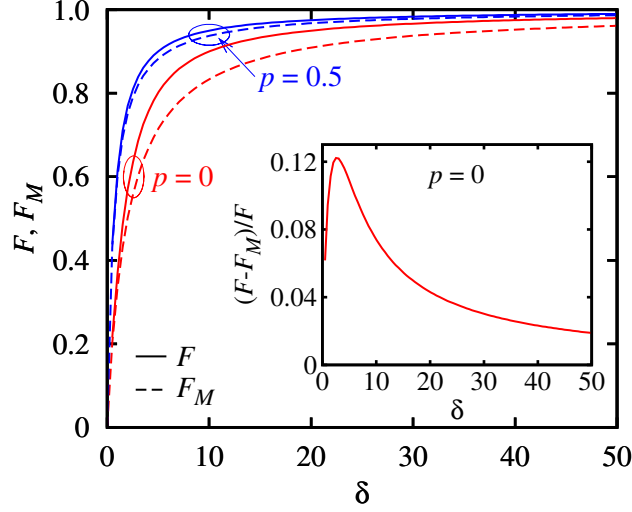


Figure 4.2: The scaling factors  $F$  and  $F_M$  [Eqs. (4.3) and (4.7)] plotted against  $\delta$  for  $p = 0$  and  $p = 0.5$ . The ratio  $(F - F_M)/F$  versus  $\delta$  is shown in the inset for  $p = 0$ .

The Matthiessen rule is commonly used to combine phonon scattering mechanisms, but, to the Author's knowledge, its accuracy has never been directly tested. Rewriting Eqs. (4.4) and (4.5) in the spirit of Eqs. (4.2) and (4.3), one finds

$$\tau_M(\boldsymbol{\kappa}) = F_M(\boldsymbol{\kappa}) \tau_{p-p}(\boldsymbol{\kappa}), \quad (4.6)$$

where

$$F_M(\boldsymbol{\kappa}) = \frac{\delta(\boldsymbol{\kappa}) [1 + p(\boldsymbol{\kappa})]}{2[1 - p(\boldsymbol{\kappa})] + \delta(\boldsymbol{\kappa}) [1 + p(\boldsymbol{\kappa})]}. \quad (4.7)$$

In Fig. 4.2,  $F$  and  $F_M$  are plotted against  $\delta$  for  $p = 0$  and  $p = 0.5$ . Both  $F$  and  $F_M$  increase monotonically with  $p$  from a minimum at  $p = 0$  to a maximum at  $p = 1$ , where  $F = F_M = 1$  for all values of  $\delta$ . The Matthiessen rule over-predicts the effect of boundary scattering ( $F_M \leq F$  for all  $p$  and  $\delta$ ). This over-prediction is greatest when  $p = 0$  and monotonically decreases as  $p$  increases. Plotted in the inset of Fig. 4.2 is the ratio  $(F - F_M)/F$  for  $p = 0$ . From the plot, it is seen that  $F_M$  deviates from  $F$  by at most 12%. Thus, using the Matthiessen rule will result in an under-prediction of the in-plane thermal conductivity by at most 12%. In the thin film LD model used



here, there is no cost advantage of using one boundary scattering expression over the other. Therefore, the more accurate expressions, Eqs. (4.2) and (4.3), are employed to compute the effective relaxation times used in Eq. (2.1).

Boundary scattering is commonly modeled using expressions similar to Eqs. (4.2) and (4.3) [33, 35, 36, 48, 107, 108] or Eqs. (4.4) and (4.5) [15, 31, 109]. In contrast to previous work, however, Eqs. (4.3) and (4.5) do not use the isotropic approximation. They instead use the ability of LD to compute the properties of all phonons in the Brillouin zone to differentiate between the in-plane and cross-plane motion of each phonon mode. The LD framework does not, however, indicate the value of the specular parameter, which, in general, depends upon the phonon mode and the atomic structure at the boundary.

#### 4.2.2 Atomic structure at the boundaries

Since the specular parameter depends upon the atomic structure at the boundaries of the thin film, knowledge of this structure can give insight into appropriate values for  $p$ . The atomic structure at the boundaries of the argon and silicon thin films are determined by performing MD simulations. The velocity Verlet algorithm is used to integrate the equations of motion using a time step of 4.3 fs for argon and 0.38 fs for silicon. The bulk equilibrium positions are used as the initial positions of the atoms in the films. In the in-plane (*i.e.*,  $x$  and  $y$ ) directions,  $4\times 4$  and  $2\times 2$  conventional unit cells are used for the argon and silicon films along with periodic boundary conditions to simulate an infinite plane. The volume of the simulation domain is allowed to change so that the structure remains unstressed. The temperature of the system is reduced from a finite temperature (50 K for argon and 300 K for silicon) to zero by removing a small amount of kinetic energy at each time step. The

Table 4.1: Zero-temperature in-plane lattice parameter for LJ argon and SW silicon.

Number of Layers	Argon $a$ (Å)	Silicon $a$ (Å)
4	5.256	5.347
8	5.263	5.370
16	5.270	5.416
32	5.270	—
64	5.273	5.433
128	5.273	—
Bulk	5.270	5.438

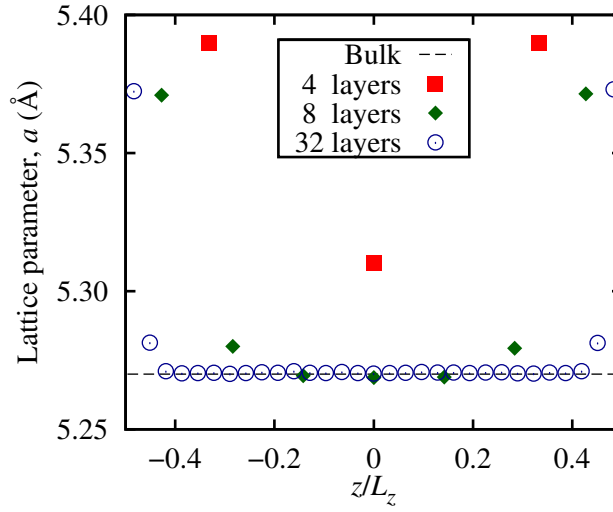


Figure 4.3: Cross-plane argon lattice parameter versus  $z/L_z$  for bulk 4, 8, and 32 atomic layers.

zero temperature equilibrium positions are taken as the final atomic positions. This quenching process is performed over two to three million time steps.

Several thicknesses of argon thin films are examined. The smallest film considered is four atomic layers ( $\sim 0.8\text{nm}$ ) thick. Thinner films did not form stable structures. The lattice parameters for bulk and the in-plane direction for the relaxed argon films are shown in Table 4.1. The thinnest film considered has an in-plane lattice parameter that is only 0.26% less than bulk. As the film thickness increases, the bulk parameter is recovered. The out-of-plane lattice parameter is plotted versus reduced atomic position ( $z/L_z$ ) for the relaxed argon films in Fig. 4.3. The plot shows that the

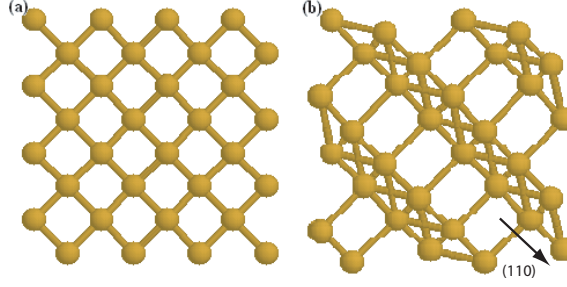


Figure 4.4: Surface atoms of thin film silicon in (a) bulk-like configuration and (b) relaxed configuration.

atomic layers near the film surface are further apart than the interior atoms. The first two layers on either surface of the films show a significant increase in lattice parameter as compared to bulk. By the third layer, though, the out-of-plane spacing returns to the bulk value.

The in-plane lattice parameters predicted for silicon thin films are given in Table 4.1. As seen for the argon thin films, the in-plane lattice parameters for silicon films are smaller than the bulk value for very thin films but approach the bulk value as the film thickness is increased. A noticeable restructuring occurs at the surface of the silicon films, however. The atoms form dimers, as shown in Fig. 4.4, consistent with experiments, *ab initio* calculations, and molecular dynamics simulations [110–112]. The surface atoms in argon films do not form dimers because the atoms are bonded through van der Waals forces, while in silicon the bonds are covalent. Like in argon films, however, the surface relaxation in silicon thin films only penetrates to the second atomic layer.

Based on this structural analysis of argon and silicon thin films, it is suspected that the phonon-boundary scattering is mostly diffuse. Rather than use  $p$  as a fitting factor, as done by others [48, 113, 114], completely diffuse boundaries ( $p = 0$ ) are assumed. This assumption is based on the idea that the reconstruction of free argon

Table 4.2: Predicted and/or measured bulk thermal conductivities for argon and silicon. The estimated uncertainty in all the LD predictions (due to the finite Brillouin zone resolution) is less than  $\pm 5\%$  [71]. The uncertainty in the argon MD predictions is less than  $\pm 5\%$  [39]. Based on typical predictions for SW silicon, the uncertainty in the silicon Green-Kubo MD result is estimated to be  $\pm 20\%$  [13, 80, 81].

Material	$T$ (K)	Method	$k$ (W/m-K)
Argon	20	LD (classical)	1.4
Argon	20	Green-Kubo MD [39]	1.2
Silicon	400	LD (classical)	350
Silicon	400	Green-Kubo MD [115, 116]	230
Silicon	300	LD (quantum)	560
Silicon	300	Experiment [87]	148

and silicon surfaces disrupts phonons traveling in the cross-plane direction, leading to a high probability that phonons incident on the boundary will scatter diffusely. Similarly, for thin films bounded by an amorphous material (such as a silicon thin film bounded by silica layers), the transition from a crystalline to an amorphous material presents a large disruption to the phonon propagation and is likely to diffusely scatter the majority of incident phonons.

The results of the structural analysis also suggests that the LD model for thin film thermal conductivity, described in the previous Section, will not be valid for very thin films. For films of extremely small thicknesses, the in-plane lattice parameters change. This effect, coupled with the restructuring of the free surfaces, which play a dominant role in very thin films, will cause the bulk phonon properties to be inaccurate for modeling phonon transport in these films. The limits of the LD model for predicting thin film thermal conductivities are discussed in the context of the model’s predicted results in Section 4.2.3.

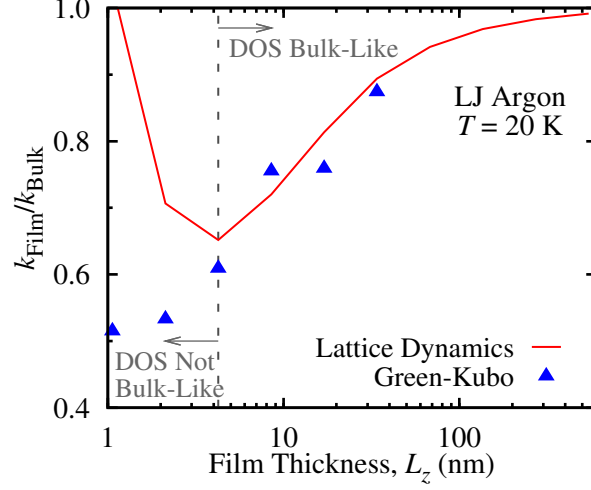


Figure 4.5: Thin film thermal conductivity as a fraction of the bulk thermal conductivity for LJ argon at a temperature of 20 K predicted from LD calculations and MD simulations using the Green-Kubo method.

### 4.2.3 Results

#### Thermal conductivity predictions

First consider LJ argon at a temperature of 20 K. The LD-based predictions are made using phonon properties in the classical limit [71] so that they may be compared to thermal conductivity predictions made with the Green-Kubo method using classical MD simulation. For the Green-Kubo MD method, five independent simulations of 9.0 ns are used with the first 0.4 ns used to equilibrate the system. Four conventional unit cells with a fixed lattice parameter of 5.315 Å are used in the in-plane directions. Based on the scatter in the independent in-plane thermal conductivity predictions, the error is estimated to be  $\pm 15\%$ .

The bulk thermal conductivities predicted by the LD and Green-Kubo MD methods are given in Table 4.2. The two predictions are in good agreement because the small atomic displacement assumption is valid at this temperature [71]. In Fig. 4.5, the thin film to bulk thermal conductivity ratio is plotted against film thickness.

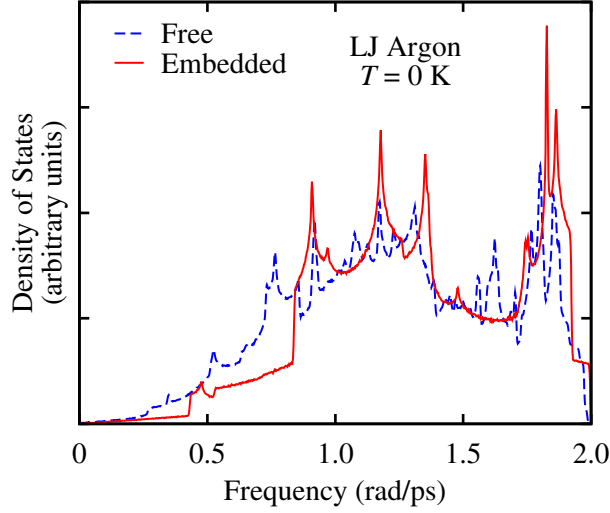


Figure 4.6: Phonon DOS for 2.1 nm LJ argon thin films at a temperature of 0 K with free surfaces (Free) and embedded in bulk (Embedded).

The thermal conductivity ratio is used to minimize differences between the different prediction methods. The thermal conductivity ratios predicted by the LD and Green-Kubo MD methods are in excellent agreement for films thicker than 4.3 nm, suggesting that the assumption of diffuse boundary scattering is valid for LJ argon thin films. The LD-based predictions for films thinner than 4.3 nm diverge from the Green-Kubo MD results. This disagreement is believed to be due to differences between the thin film and bulk phonon DOS.

As evidence for this assertion, the phonon DOS for a 2.1 nm thick LJ argon film at a temperature of 0 K computed for a structure with free surfaces that is relaxed using MD is plotted in Fig. 4.6. Also plotted is the DOS for a 2.1 nm thick film embedded in bulk [*i.e.*, limited to bulk phonons that satisfy Eq. (4.1)]. There are notable differences between the DOS of the free and embedded films, particularly between frequencies of 0.5 and 0.8 rad/ps, where the DOS of the free film is larger than the DOS of the embedded film. As the film thickness increases, the DOS of the free and embedded films converge to the bulk DOS. For films thinner than 2.1 nm,

the DOS of the free and embedded structures become more distinct. This qualitative comparison between the DOS of the free and embedded films suggests that the LD-based model for in-plane thin film thermal conductivity, which uses the phonon population of the embedded film, cannot be applied to LJ argon films with thicknesses of 2.1 nm (8 atomic layers) or less. This assessment is confirmed by the predicted thin films thermal conductivities, where, for films smaller than 4.3 nm (16 atomic layers), the predicted thermal conductivities diverge from the Green-Kubo results. Similarly, from the DOS of free and embedded SW silicon films and the predicted thermal conductivities, the LD-based approach is found to be appropriate when the film thickness is 17.4 nm (128 atomic layers) or greater.

For the SW silicon thin films, the LD-based results at a temperature of 400 K are computed in the classical limit so that they may be compared to Green-Kubo MD predictions. [13] The predicted bulk thermal conductivities are given in Table 4.2. The LD-based bulk thermal conductivity prediction is 52% higher than the corresponding Green-Kubo MD prediction. This difference is due to the low-temperature approximations inherent in the LD technique (see Section 2.3). As shown in Fig. 4.7(a), the LD model under-predicts the SW silicon thin film thermal conductivity ratio found from Green-Kubo MD by 30% on average. The majority of this under-prediction is likely caused by the assumption of completely diffuse boundary scattering. Assuming partially specular boundary scattering would increase the thermal conductivity. The under-prediction may also be partially due to the low-temperature approximations inherent in the LD methods, leading to an over-prediction of the phonon-phonon relaxation times and an under-prediction of  $F$ .

The available experimental measurements at a temperature of 300 K [33,34,36,49] are compared to quantum LD predictions at 300 K. The large difference between the

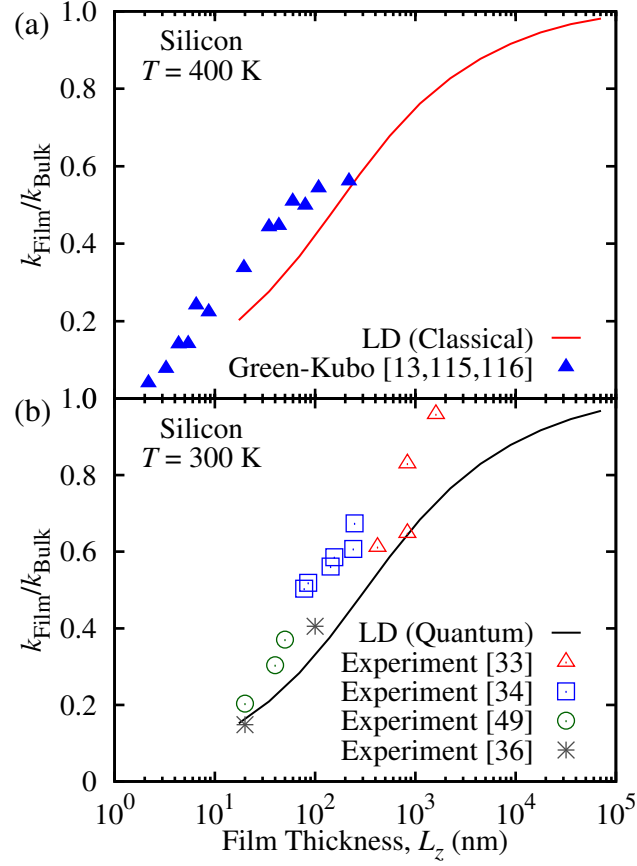


Figure 4.7: Silicon thin film thermal conductivity normalized by the bulk thermal conductivity as found from (a) classical LD calculations and the Green-Kubo MD method at a temperature of 400 K and (b) quantum LD calculations and experiment at a temperature of 300 K.



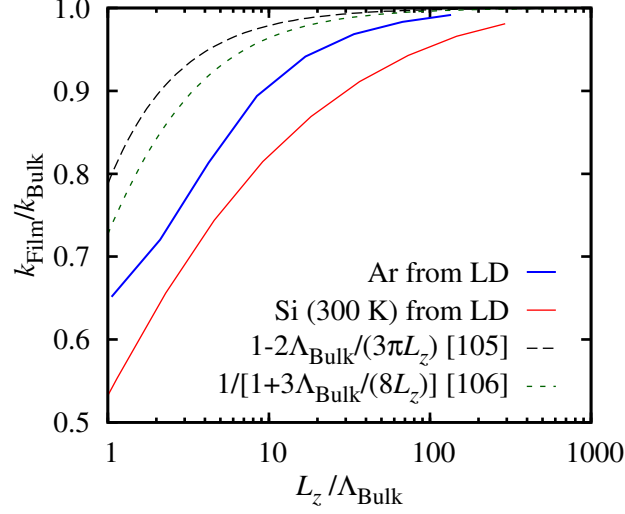


Figure 4.8: Thin film thermal conductivity ratio ( $k_{\text{Film}}/k_{\text{Bulk}}$ ) versus  $L_z/\Delta_{\text{Bulk}}$  for argon and silicon (300 K) thin films and estimations derived from theory.

LD-predicted and experimental bulk thermal conductivities, seen in Table 4.2, is due to the combined effects of the approximations in the LD techniques and the inability of the SW potential to accurately model thermal transport in silicon [76]. The four sets of experimental results plotted in Fig. 4.7(b) represent two *p*-type [34,49] and one *n*-type [33] silicon films sandwiched between silica layers and one suspended bridge of pure silicon [36]. The same bulk thermal conductivity value is used to compute the thermal conductivity ratio for each film [87]. The large scatter in the experimental data makes it difficult to discern an accurate trend. One can say, however, that the thermal conductivity ratio predicted with the LD model is in good agreement with the lower bound of the experimental results, consistent with the assumption of diffuse boundary scattering.

#### 4.2.4 Insights from phonon properties

Using the LD results, the average phonon mean free path (MFP),  $\Lambda$ , is computed from

$$\Lambda = \frac{k}{\sum_{\kappa} \sum_{\nu} c_{ph}(\kappa) |v_{g,x}(\kappa)|}. \quad (4.8)$$

Comparing Eq. (4.8) to Eqs. (2.1) and (4.2), one sees that  $\Lambda$  is a weighted average of  $|v_{g,x}| \tau_{p-p} F$ . The classical effective MFP for bulk LJ argon at a temperature of 20 K is 4.03 nm. For SW silicon at a temperature of 300 K (400 K), the bulk quantum (classical) effective MFP is 243 nm (125 nm). The reductions of the effective MFPs in the thin films are the same as the reductions of the thermal conductivity (*i.e.*,  $\Lambda_{\text{Film}}/\Lambda_{\text{Bulk}} = k_{\text{Film}}/k_{\text{Bulk}}$ ). The reductions in the thermal conductivity and MFPs for the thin films are driven by the boundary scattering [Eq. (4.3)], which, under the assumption of diffuse scattering, does a good job of accounting for the altered phonon dynamics. In Fig. 4.8, the thermal conductivity ratio is plotted versus  $L_z/\Lambda_{\text{Bulk}}$  for the LJ argon film and the SW silicon film at a temperature of 300 K. Also plotted in Fig. 4.8 are two proposed, simple models [105,106] for predicting the reduction of the in-plane thermal conductivity using the bulk MFP. Neither expression can predict the differing rates of convergence to bulk of the LJ argon and SW silicon thin film thermal conductivity ratios.

The frequency-dependent contribution to the thermal conductivity for bulk SW silicon and for the 556 and 34.8 nm thin films at a temperature of 300 K are plotted in Fig. 4.9. The area under each curve is proportional to the total thermal conductivity. Phonon modes with frequencies below 50 rad/ps dominate thermal transport. The film boundaries have the largest impact on these phonon modes. The phonon modes with higher frequencies, which contribute little to the total thermal conductivity,

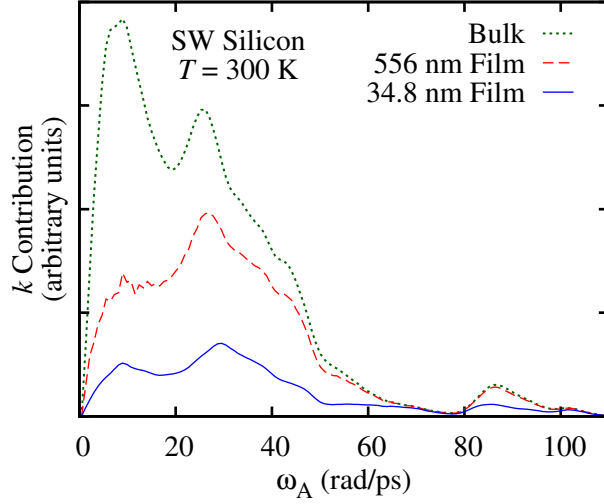


Figure 4.9: Contribution to the phonon thermal conductivity versus frequency for SW silicon in bulk and 556 and 34.8 nm thin films at a temperature of 300 K. The area under each curve is proportional to the total thermal conductivity.

are less sensitive to the boundaries. These results can be explained by noting that high-frequency phonons generally have small group velocities and phonon-phonon relaxation times. In the limit of zero group-velocity or phonon-phonon relaxation time,  $F$  is unity [see Eq. (4.3)] and the boundaries do not affect the phonon properties. For thinner films, however, the boundaries affect even the high-frequency phonons, as illustrated by the reduction in the peak at 86 rad/ps in the 34.8 nm film.

The information contained in Fig. 4.9 can be used to devise strategies to alter the in-plane thermal transport properties of silicon thin films. For example, to reduce the in-plane thermal conductivity, films could be fabricated with embedded nanoparticles where the size of the nano-particles is tuned to scatter phonons of specific wavelengths [117–119]. In bulk, the most effective nano-particles would be those that scatter phonons with wavelengths that correspond to frequencies around 10 rad/ps. In thin films, however, the most effective nano-particles would scatter phonons with frequencies closer to 30 rad/ps.

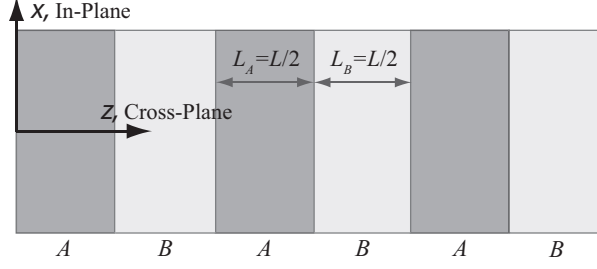


Figure 4.10: Schematic diagram of the superlattice. The superlattice is periodic in all three directions. The mass of material  $B$  is two or five times that of material  $A$  and  $L_A = L_B = L/2$ .

The in-plane thermal conductivity of a thin film can be increased by reducing the probability that phonons will scatter diffusely at its boundary. Careful fabrication and intelligent selection of the materials bonded to the surfaces of the thin film (*i.e.*, controlling the substrate material and growth process) will increase the thermal conductivity. High quality interfaces encourage specular phonon scattering and the transmission of phonons between the thin film and the adjacent material, particularly for long wavelength phonon modes, which tend to have low frequencies. [6]

### 4.3 In-plane and cross-plane phonon transport in superlattices

#### 4.3.1 Computational framework

Superlattices do not present the same modeling challenges as the thin films. Superlattices are periodic in all three dimensions, therefore, the LD techniques can be directly applied. It is important to note however, that the LD techniques implicitly model only coherent phonon transport. This limitation of the LD techniques means that the interfaces do not act as scattering sites, limiting the ability of the LD techniques to model thermal transport in heterostructures.

Here, only ideal superlattices containing two materials, argon and “heavy” argon, are examined. Both materials are modeled with the Lennard-Jones potential using the same parameters but “heavy” argon has a mass two times or five times that of

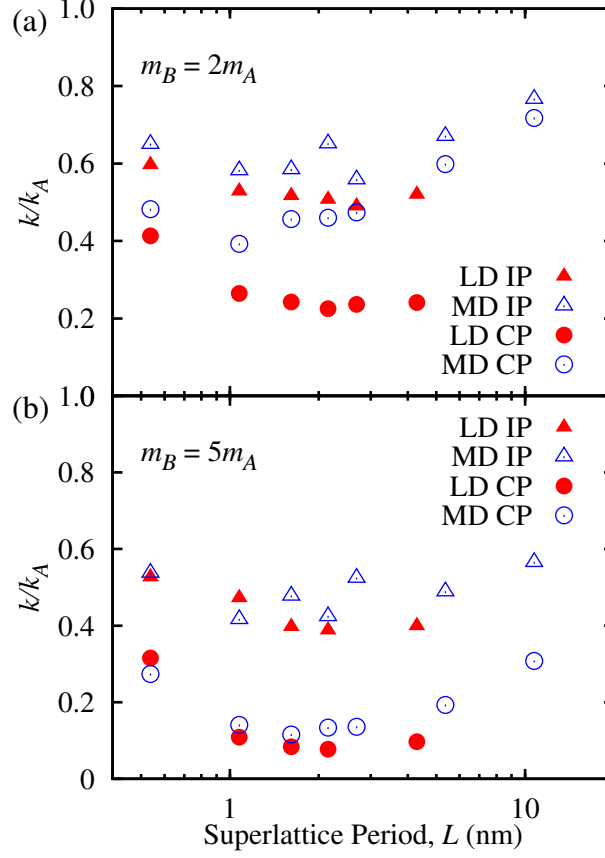


Figure 4.11: In-plane (IP) and cross-plane (CP) thermal conductivities for (a)  $m_B/m_A = 2$  and (b)  $m_B/m_A = 5$  superlattices as a fraction of the thermal conductivity of bulk argon from LD and MD [85]. The prediction uncertainty is estimated to be  $\pm 5\%$  for the LD method, due to the finite BZ resolution and  $\pm 20\%$  for the Green-Kubo MD results [85].

argon. The superlattices are of type  $ABAB$  as shown in Fig. 4.10, where the thickness of each film is equal,  $L_A = L_B = L/2$ . The cross-plane ( $z$ ) direction is oriented along the  $[001]$  crystallographic direction. The unit cell spans a full superlattice period,  $L$  and contains  $4L/a$  atoms. The superlattices are examined in the classical limit at a temperature of 40 K, where MD based predictions are available [85]. The thermal conductivity predictions are extrapolated to an infinite number of wave vectors using four  $N_0 \times N_0 \times N_0$  wave vector grids where  $N_0 = 6, 8, 10$ , and 12 (see Section 2.3.2).

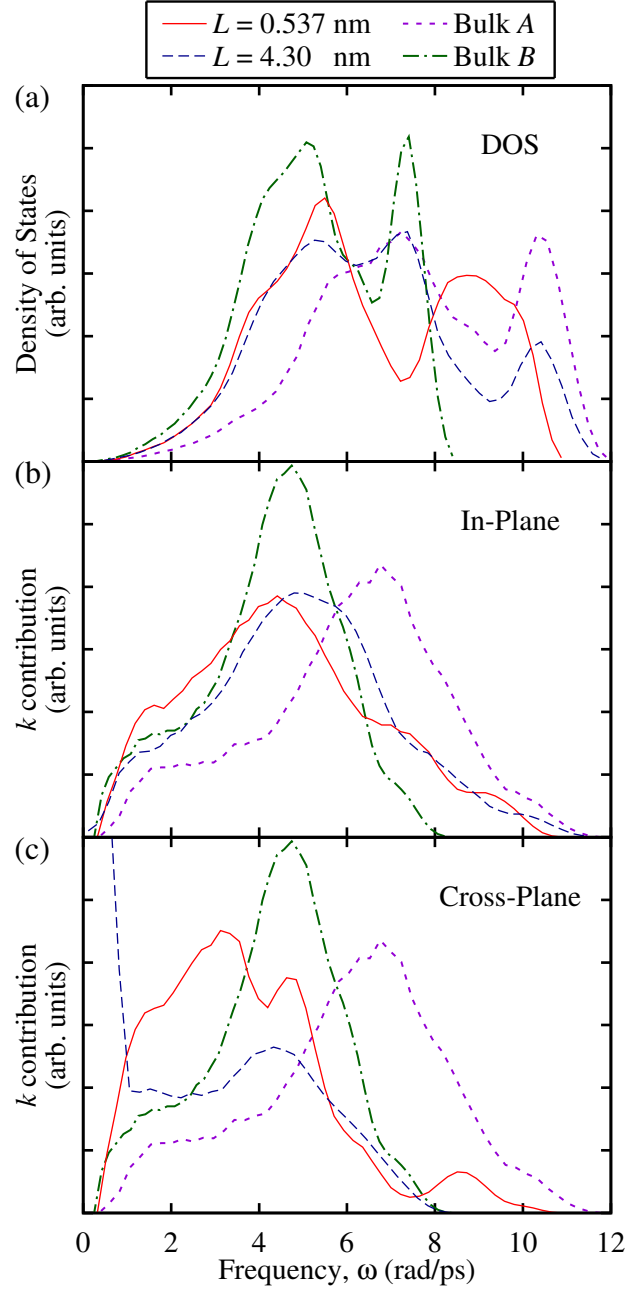


Figure 4.12: The (a) Phonon DOS and (b) in-plane and (c) cross-plane contributions to the thermal conductivity as a function of frequency for the  $m_B/m_A = 2$  superlattices with  $L = 0.537$  and  $L = 4.30$  nm as well as bulk extents of materials *A* and *B*. The area under the phonon DOS curve is proportional to the number density of phonons (equal in all structures) while the area under the thermal conductivity contribution curves are proportional to the thermal conductivity of each structure.

### 4.3.2 Results and discussion

First, consider the superlattices where the mass of material  $B$  is twice the mass of argon (material  $A$ ). The LD-predicted in-plane and cross-plane thermal conductivities are plotted in Fig. 4.11(a) as a fraction of the bulk thermal conductivity of argon,  $k_A$  (see Table 4.2). Also plotted in Fig. 4.11(a) are in-plane results from Green-Kubo MD predictions and cross-plane results from the direct MD method [85]. For the shortest period superlattices considered, the LD and MD predictions agree. The agreement for the in-plane thermal conductivity predictions continues for the superlattices with longer periods. In the cross-plane direction, however, the LD-predicted thermal conductivities diverge from the MD-predicted values as  $L$  increases. This disagreement is a result of the coherent phonon transport imposed by the LD method.

To better understand the ramifications of forced coherent phonon transport, consider idealized phonon transport in long period superlattices with perfect interfaces. In the idealized case of a phonon propagating in either material, if the phonon encounters an interface, it will either transmit into the adjacent material (if the frequency of the phonon is supported in both materials) or elastically reflect off the interface. Either way, energy propagation continues along the in-plane direction in a coherent manner until it undergoes a phonon-phonon scattering event. When a phonon reflects off the interface, however, the cross-plane direction of energy propagation has reversed. Thus, both elastic reflections from interfaces and inelastic scattering events disrupt energy transport in the cross-plane direction.

This idealized phonon transport is a good approximation of what occurs in the MD simulation. It also explains the reason why the in-plane thermal conductivity is higher than the cross-plane thermal conductivity. The LD model differs from this

ideal. Since the LD calculations enforce coherent transport through the superlattice, any phonons traveling in the cross-plane direction can exist in both materials. In the LD model, the phonons traveling in the cross-plane direction can not be associated with either material  $A$  or material  $B$  but are a product of the composite material (*i.e.*, the superlattice as a whole). The interfaces have no effect on these phonons. Thus, the reduction in the cross-plane thermal conductivity below the bulk value arises because of the altered phonon properties for the structure as a whole, not the effect of bulk-like phonons interacting with interfaces. In very short period superlattices, the LD model is accurate for both cross-plane and in-plane phonon transport because the individual material layers are too short for phonons to develop and propagate in a single layer. Thus, these superlattices behave as a single crystal rather than a composite of several thin film and the phonon transport in any direction is strictly coherent. For long period superlattices, though, the LD-predicted polarization vectors indicate that phonons traveling solely in the in-plane direction can be associated with a single material layer. Hence, these phonons are properly modeled with the LD techniques and the LD- and MD-predicted in-plane thermal conductivities, plotted in Fig. 4.11(a), agree well.

Support for these assessments of the LD model is given in Figs. 4.12(a)-(c), which show the phonon DOS and the in-plane and cross-plane thermal conductivity as a function of frequency for  $L = 0.537$  and  $L = 4.30$  nm superlattices with  $m_B = 2m_A$ . Also plotted in the figures are the phonon DOS and thermal conductivity contribution for bulk extents of materials  $A$  and  $B$ . For the  $L = 4.30$  nm superlattice, the phonons in materials  $A$  and  $B$  are largely independent. The phonon DOS of the  $L = 4.30$  nm superlattice is approximately the average of the phonon DOS of the bulk materials. Similarly, the contribution to the in-plane thermal conductivity is well approximated



by the average of the bulk materials. However, only phonons that are due to the superlattice as a whole can propagate in the cross-plane direction and contribute to the thermal conductivity. As seen in Fig. 4.12(c), the cross-plane propagating phonons are dominated by low frequency (which are also long wavelength) phonons and no phonons with frequencies above the maximum frequency in material  $B$  can propagate across the material layers.

For the  $L = 0.537$  nm superlattices, the period is short enough that the superlattice behaves as a single material rather than a composite of two different materials. The phonon DOS for the short period superlattice is not a composite of the DOS for the bulk materials. It exhibits a strong local minimum at 7.5 rad/ps, where a local maximum exists in both DOS and a local maximum at 8.5 rad/ps where material  $A$  possesses a local minimum and the DOS of material  $B$  is nonexistent. The contribution to the in-plane thermal conductivity shifts away from the average of the bulk contributions such that the lower frequency phonons transport more energy through the shorter period superlattice. Most striking in this superlattice is the cross-plane phonon transport. A noticeable, albeit small, contribution to the cross-plane thermal conductivity comes from phonon modes with frequencies that are not present in the bulk extent of material  $B$ . This phenomenon has also been observed in MD simulation of transport across thin films [120].

The results for the  $m_B = 5m_A$  superlattices, shown in Fig. 4.11(b), are similar to the results for the  $m_B = 2m_A$  superlattices. The thermal conductivity predictions from LD agree with the MD results for the in-plane direction and for the cross-plane direction in short period superlattices. As the superlattice period is increased, the LD- and MD-predicted cross-plane thermal conductivities do not diverge as quickly as they do for the  $m_B = 2m_A$  superlattices. In the  $m_B = 5m_A$  superlattices, fewer phonons

can transmit from material  $A$  into material  $B$  than in the  $m_B = 2m_A$  superlattices because of the larger mass difference (and correspondingly larger differences in the phonon DOS). Because of this reduced transmission, the coherent phonons play a more important role in the cross-plane thermal conductivity. Thus, the LD-based predictions are more accurate even for longer superlattice periods.

#### 4.4 Conclusions

The in-plane thermal conductivity of a thin film is reduced from the corresponding bulk value. The thinner the film, the more severe the reduction. Efforts to explain the mechanisms behind this reduction are complicated by the routine use of fitting parameters and the isotropic approximation when modeling phonon transport. To eliminate these complications, a methodology for predicting the in-plane thermal conductivity of thin films has been developed and presented. This method uses bulk phonon properties obtained from LD calculations along with the Boltzmann transport equation under the relaxation time approximation. The effect of the boundaries are included by considering only those phonons with wavelengths that fit within the film and modifying the relaxation times to account for mode-dependent, diffuse boundary scattering [see Eqs. (4.2) and (4.3)]. The use of diffuse boundary scattering is justified by the reconstruction observed in the free surfaces of argon and silicon thin films. Additionally, it is shown that using the Matthiessen rule will result in an under-prediction of the in-plane thin film thermal conductivity of at most 12%.

Given that bulk phonon properties are being used, it is not expected the LD model should work for very thin films, where the phonon population deviates from that of a bulk system. It is found that the use of bulk phonon properties is appropriate for LJ argon films thicker than 4.3 nm and SW silicon films thicker than 17.4 nm.

The LD-based thermal conductivity predictions for argon thin films at a temperature of 20 K are in excellent agreement with predictions made using the Green-Kubo MD method (see Fig. 4.5). This agreement supports the assumption that phonon-boundary scattering is diffuse in LJ argon films.

When compared to Green-Kubo MD predictions for SW silicon at a temperature of 400 K, the LD model over-predicts the thermal conductivity reduction by an average of 30% (see Fig. 4.7), suggesting the existence of partially specular phonon boundary scattering. The LD-predicted reductions in the thermal conductivity are in good agreement with the lower bound of the available experimental measurements. This last result, combined with the spread in the experimental data, indicates that the quality of the thin film boundary affects the phonon-boundary scattering, creating boundaries that can be partially specular to completely diffuse.

Upon computing the bulk MFPs in the argon and silicon systems, it is found that the reduction in the in-plane thin film thermal conductivity cannot be explained by this parameter alone. Instead, the properties of the individual phonon modes are required. Knowledge of the phonon properties can also be used to gain insight into the mechanisms of phonon transport through bulk crystals and nano-structures and to quantify the importance of individual phonon modes. This insight can potentially be used to devise and tune techniques to adjust the thermal conductivity of nano-structured materials.

Although a superlattice can be thought of as periodic layers of thin films, it can be modeled directly using the LD techniques because it is periodic. However, the LD methods enforce coherent transport for the phonons that propagate in the cross-plane direction. These phonons can be considered bulk-like phonons of the superlattice as a whole as they do not interact with the interfaces and can exist in both material layers.

This scenario of coherent phonon transport is accurate for short period superlattices, where the individual material layers are too thin to support bulk-like phonons in each layer. It is inaccurate for long period superlattices, however, since bulk-like phonons can develop in a single layer, propagate in the cross-plane direction, and interact with the interfaces. Despite this inaccuracy in the cross-plane direction, the in-plane thermal conductivity can be accurately modeled using LD. The in-plane thermal conductivities predicted by the LD and MD methods are in agreement for all superlattices considered (see Fig. 4.11), because bulk-like phonons can develop in each layer and propagate in the in-plane directions.

## CHAPTER V

### **Transport in structures with reduced dimensionality: Graphene and carbon nanotubes**

#### **5.1 Introduction**

The thin films examined in Chapter IV are quasi-two-dimensional structures. The energy transport is in the in-plane directions, however, phonons can still propagate in the cross-plane direction. Graphene, however, is a true two-dimensional structure, in which phonons can only travel in the plane of the structure. Similarly, CNTs are true one-dimensional structures, in which phonons can only propagate along the axis of the tube. There has been much excitement and speculation about the phonon transport properties in these structures of reduced dimensionality. The thermal conductivities of these structures, for example, have been predicted [22, 121, 122] and measured [123, 124] to be higher than that of diamond. Potential applications for these carbon materials include embedding to produce thermally conductive polymers and epoxies [125], use as electrical components to reduce heat generation and improve heat removal [123], and a host of additional applications to take advantage of their unique electrical, structural, and optical properties [126, 127].

The mechanisms underlying the extremely large thermal conductivity in graphene and CNTs are not well understood [22, 122]. Much theoretical and numerical work has

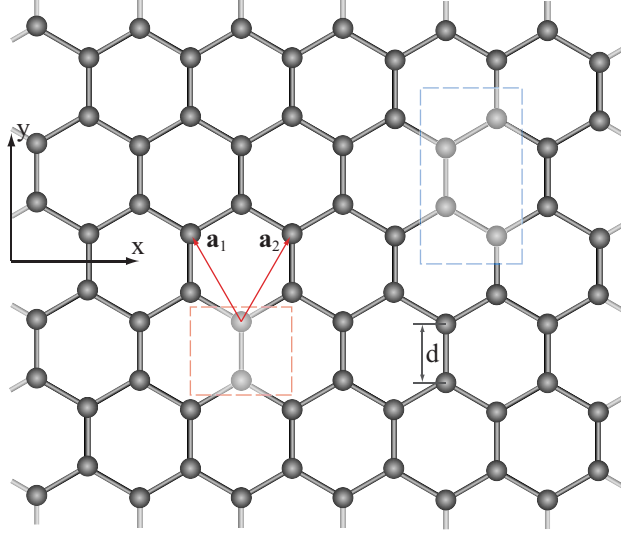


Figure 5.1: Schematic diagram for graphene with carbon-carbon distance  $d$ . The two and four atom unit cells are denoted by boxes. The four atom unit cell is used in this work. The two atom unit cell is the primitive cell. The primitive lattice vectors are given by  $\mathbf{a}_1$  and  $\mathbf{a}_2$ . The armchair CNTs are defined by the chiral vector  $\mathbf{C}_h = l\mathbf{a}_1 + l\mathbf{a}_2$ , which gives the CNT's circumference (about the  $x$  axis) and are denoted by  $(l,l)$ . The unit cell used for the CNTs encloses the entire tube cross section and has a length ( $x$  extent) of  $\sqrt{3}d$ ; the same as the four atom unit cell shown.

been done to study the thermal transport through these structures [22,121–124]. However, the same factors that obfuscate the characteristics of phonon transport in bulk crystals, thin films, and superlattices (fitting parameters, major approximations and assumptions, experimental challenges due to extreme small scale) are present when studying phonon transport in structures of reduced dimensionality. Thus, graphene and CNTs are ideal candidates to be examined using LD calculations.

## 5.2 Structure and modeling

A schematic diagram for graphene is shown in Fig. 5.1. The four atom unit cell is used in this work and is analogous to the unit cell used for the CNTs. Armchair CNTs are defined by the chiral vector  $\mathbf{C}_h = l\mathbf{a}_1 + l\mathbf{a}_2$ , where  $\mathbf{a}_1$  and  $\mathbf{a}_2$  are the primitive lattice vectors associated with the two atom primitive cell. The chiral vector gives the CNT's circumference (about the  $x$  axis) and are denoted by  $(l,l)$  [126]. The unit

cell used for the CNTs encloses the entire tube cross section and has a length/lattice parameter ( $x$  extent) of  $a = \sqrt{3}d$ ; the same as the four atom unit cell shown.

The Brenner reactive empirical bond order (REBO) potential [128] is chosen to model the interactions between the carbon atoms in the graphene and CNT structures. The dihedral angle is found to be insignificant [83] and is neglected in this study. When the zero-strain carbon-carbon distance of 1.42 Å [128,129] is used, soft phonon modes (*i.e.*, imaginary frequencies) are found from harmonic LD calculations. Such phonon modes are indicative of unstable structures, and, in this case, is evidence that isolated graphene sheets and CNTs buckle slightly [127]. Here, the soft phonon modes are removed by slightly straining the graphene sheets and CNTs by using a carbon-carbon distance of 1.43 Å. The radial strain in the CNTs is relaxed by a steepest decent minimization of the energy with respect to the radial atomic positions. The frequency shifts in both the graphene and CNT structures are ignored, as they make some of the low frequency modes negative. This issue is likely related to the instability demonstrated by the harmonic calculations, which has not been fully removed. For computing the thermal conductivity, the thicknesses of the graphene sheets and CNT rings are set to 3.4 Å, which is the separation between the graphene layers in graphite [130,131].

### 5.3 Results

The [100] dispersion curves and the phonon DOS are shown for graphene and the (5,5) and (10,10) CNTs in Figs. 5.2-5.4. The CNT dispersion curves possess the characteristic four acoustic branches, one longitudinal dispersion branch, two degenerate transverse/bending branches, and a branch due to twisting about the tube axis. Of particular note are the lowest frequency acoustic branches which are

quadratic near  $\kappa = \mathbf{0}$  rather than linear. These branches correspond to the out-of-plane transverse mode in graphene and the two degenerate transverse (bending) modes in the CNTs. These dispersion branches give rise to a unique temperature dependence of the specific heat and thermal conductivity in the low-temperature limit [126,132]. The other acoustic dispersion branches are linear near  $\kappa = \mathbf{0}$ , as is typical of most crystals, and the longitudinal modes give rise to large sound velocities ( $\sim 20,000$  m/s for both graphene and the CNTs).

The phonon DOS of the (5,5) CNT exhibits characteristics of a one-dimensional system, where the phonon DOS varies as  $1/\sqrt{\omega}$  [132] and is analogous to the  $1/\sqrt{E}$  dependence of the electronic DOS in one dimensional systems [133]. These characteristics are less clear in the larger, (10,10) CNT, whose phonon DOS bears a closer resemblance to the phonon DOS for graphene. Thus, as the diameter of a CNTs is increased, the phonon modes become more like those found in graphene and similar thermal properties should be expected from graphene and large diameter, single-walled CNTs.

The graphene thermal conductivity is extrapolated from  $2N_0 \times N_0$  lattices with  $N_0 = 25, 30$ , and  $35$  unit cells. The predicted thermal conductivity in the  $x$  and  $y$  directions are  $380$  and  $300$  W/m-K. The result for the  $x$  direction compares well with the  $350$  W/m-K predicted by Thomas *et al.* [134] using the direct MD method with the Brenner REBO potential. The higher thermal conductivity is along the zigzag, which is along the axis of the armchair CNTs. The thermal conductivity contribution as a function of frequency is shown in Fig. 5.2(b). The contribution is nearly identical for both the  $x$  and  $y$  directions except around a frequency of  $5$  rad/ps. As seen in Fig. 5.5, the thermal conductivity predictions for the armchair CNTs made using the



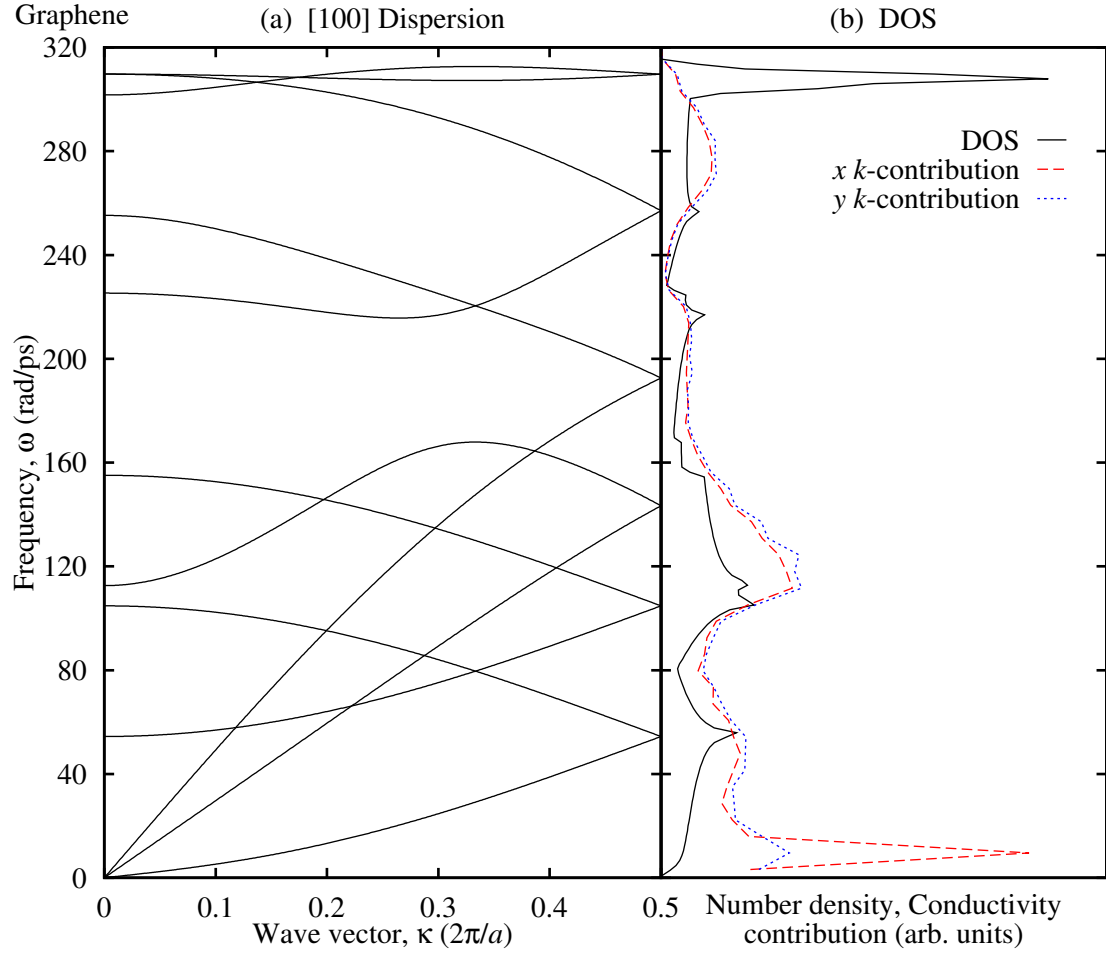


Figure 5.2: Dispersion curves in the [100] direction and phonon DOS for graphene.

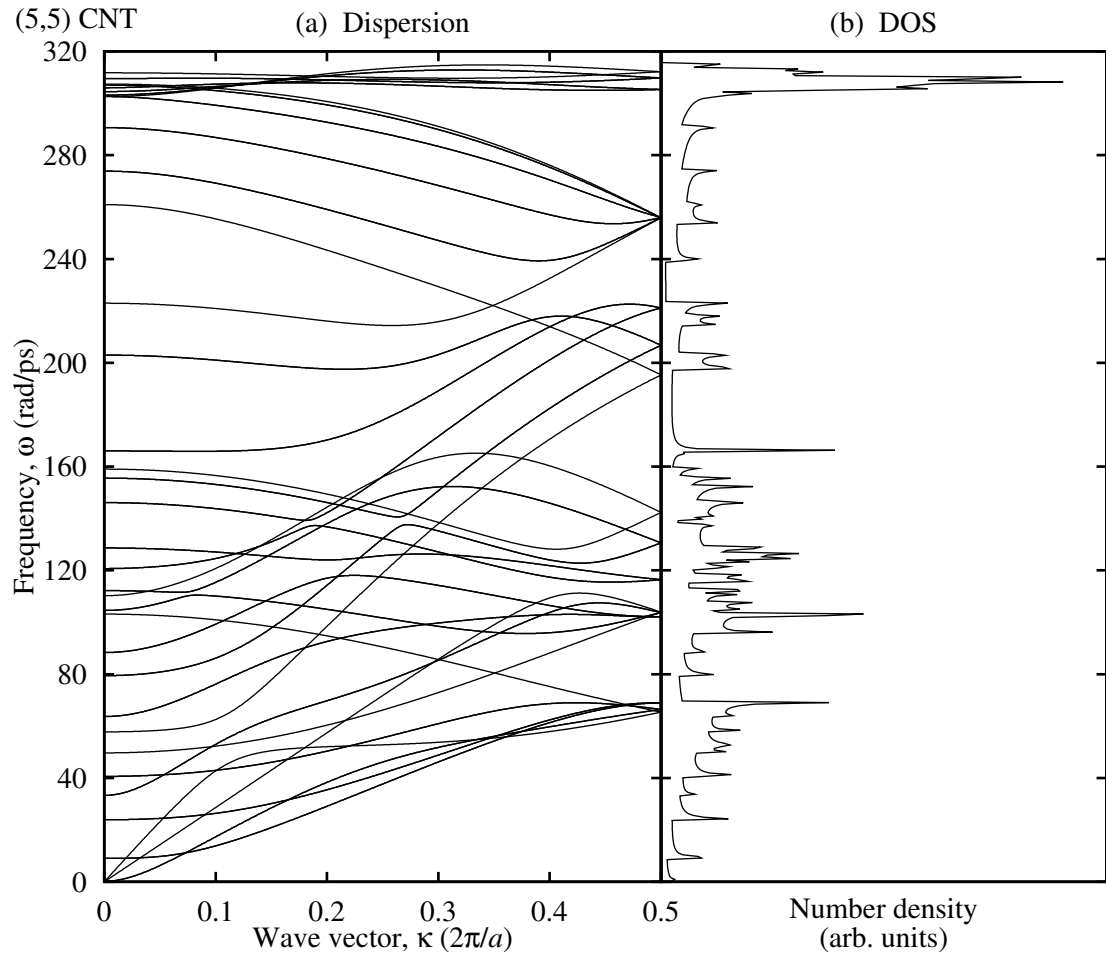


Figure 5.3: Dispersion curves and phonon DOS for the (5,5) CNT.

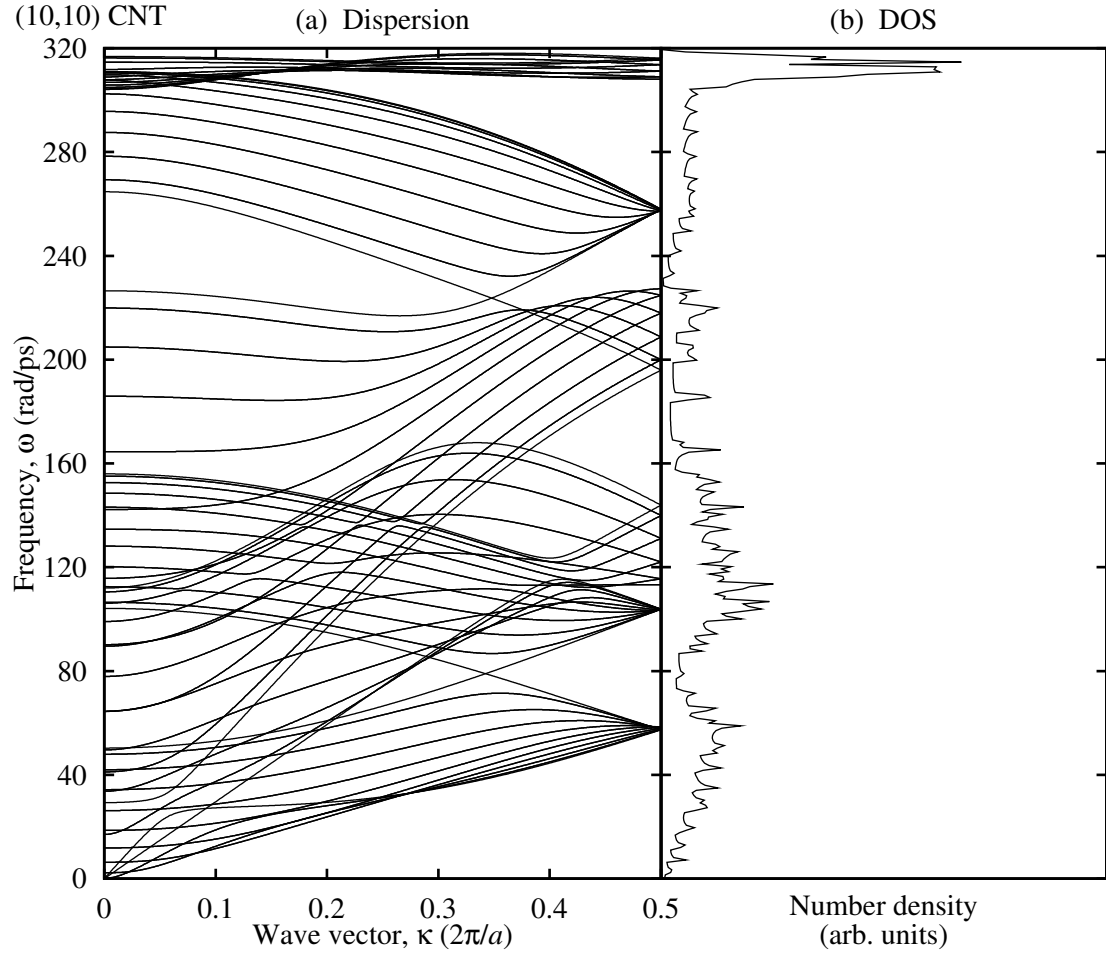


Figure 5.4: Dispersion curves and phonon DOS for the (10,10) CNT.

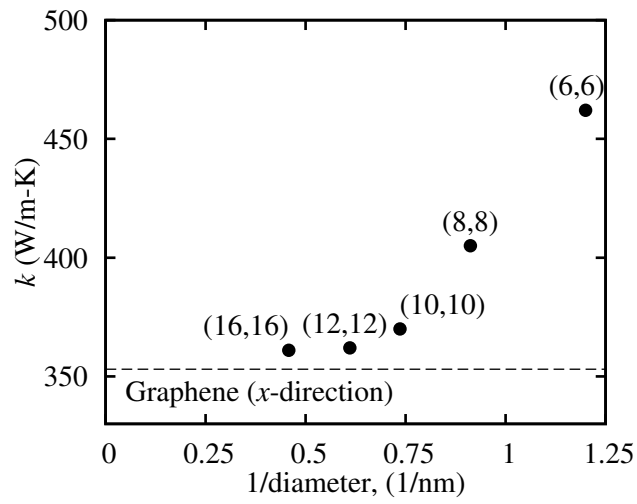


Figure 5.5: Thermal conductivity in graphene and armchair CNTs as predicted by the direct method and MD simulation [134].

direct MD method converge to the graphene thermal conductivity in the  $x$  direction as the CNT diameter increases.

Thermal conductivity predictions for the CNTs were not made using LD because of issues with size effects. Carbon nanotubes up to 3000 unit cells in length (740 nm) were examined. Yet, the thermal conductivity did not converge to a value that was independent of the BZ resolution. Furthermore, the extrapolation technique did not provide a reasonable fit to the predictions, hence it could not be used. This failure to achieve a length-independent thermal conductivity prediction is surprising given that length-independent predictions are achieved in the larger diameter CNTs using 700 nm long CNTs with the direct MD method [134].

Investigation of the phonon relaxation times reveals that the vast majority of the phonon lifetimes have converged to length-independent values for CNTs with as few as 50 unit cells (12 nm). The low-frequency acoustic modes, however, never converge. When using the spectral energy density with MD, Thomas *et al.* [82] find all the phonon relaxation times in the (8,8) CNT to be independent of length when 50 or more unit cells are used. Using the same length CNT with anharmonic LD results in an over-prediction of the low-frequency acoustic mode relaxations times by up to two orders of magnitude when compared to the spectral energy density results [82, 135]. This difference is in spite of the fact that the anharmonic LD calculations and the spectral energy density method are closely related [83]. For identical systems, one should expect the same result from the LD and spectral energy density methods if the assumptions used in the LD calculations are correct.

The phonon lifetimes predicted with the spectral energy density method all converge to length-independent values and the predicted thermal conductivity is in excellent agreement with the direct MD prediction [82]. Thus, the spectral energy density

predictions should be viewed as correct. The over-prediction of the low-frequency acoustic relaxation times by the LD method may be caused by neglecting phonon-phonon scattering processes involving four or more phonons. It may also be caused by broadening of the allowed wave vectors.

Scattering processes involving four or more phonons are captured with the spectral energy density in MD simulation but not with anharmonic LD calculation. The constraints on the three-phonon processes, imposed by the conservation of wave vector and frequency, may not allow for sufficient representative interactions between the low-frequency acoustic modes and other phonons. Since the higher-order phonon interactions involve more phonon modes, the constraints on the wave vectors and frequencies are less restrictive, allowing for more scattering events to occur and reducing the relaxation time.

Though the LD-predicted relaxation times for the low-frequency acoustic phonons in CNTs never length-independent, they do appear to be converging to the spectral energy predictions [135] with increasing CNT length, which suggests that it is not the higher-order phonon processes that lead to the discrepancy with the spectral energy density predictions. Instead, the over-prediction of the low-frequency acoustic mode relaxation times may be due to broadening of the wave vector. This wave vector broadening is analogous to frequency broadening which is included in the anharmonic LD calculations used in this work through Eqs. (2.31), (2.32) and (2.33), where the phonon linewidths are used as the broadening parameter. As shown in Fig. 5.6, both broadening in the phonon frequencies and wave vectors is observed with the spectral energy density. Indeed, broadening in the frequencies is used to determine the phonon relaxation times. Just as the frequency broadening relaxes the energy conservation restraint, so too should the wave vector broadening relax the constraint on the wave

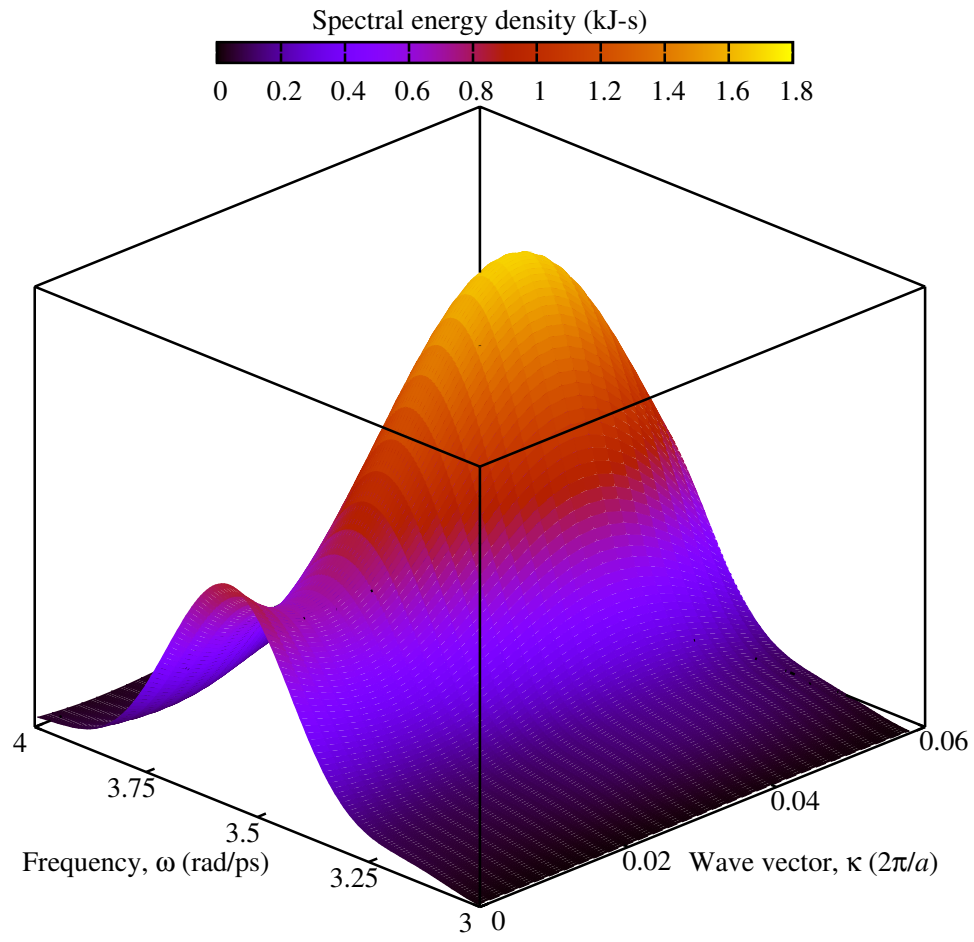


Figure 5.6: Spectral energy density around the lowest optical phonon mode at  $\kappa_x = \frac{2\pi}{50a}$  in the (8,8) CNT [136].

vectors. Because of this broadening, all combinations of three phonons are a valid interaction, and the relaxed constraints on the frequencies and wave vectors become a factor in defining the strength of the interaction. Thus, there are many possible three-phonon interactions even for a relatively small number of unit cells.

The frequency and wave vector broadening can be thought of as artifacts of the uncertainty inherent in mapping the finite atomic motion onto normal mode coordinates. In the limit of zero atomic motion, the total energy of each atom is constant (equivalently, there are no anharmonic effects) and there is no uncertainty in the phonon frequencies or wave vectors. For finite atomic motion, the displacements cause the total energy associated with each atom to fluctuate introducing anharmonicity. The resulting variations in atomic position and energy lead to an uncertainty/broadening in the wave vector and frequency. Unlike the frequency which is solved for in the LD calculations, the wave vector is assumed. The wave vector is imposed to describe the periodicity of the lattice and vastly reduces the number of independent equations. This simplification through periodicity is a cornerstone of the LD calculations. Thus, determining the uncertainty in the wave vector and broadening it in the LD calculations, in a manner similar to the frequency broadening, may not be possible.

## 5.4 Conclusions

The phonon DOS for armchair CNTs converge to the phonon DOS of graphene as the CNT diameter increases, suggesting that the thermal properties in large diameter CNTs are similar to that of graphene. This hypothesis is shown to be true by the direct MD thermal conductivity predictions of Thomas *et al.* (Fig. 5.5) [134]. The contribution to the thermal conductivity as a function of frequency is nearly identical for the  $x$  and  $y$  directions in graphene, except at 5 rad/ps.

Though CNTs up to 3000 unit cells (740 nm) in length were examined with the LD methods, a length-independent thermal conductivity could not be obtained, nor could the extrapolation procedure be used. The non-convergence of the thermal conductivity prediction can be traced to a small number of low-frequency acoustic phonon modes, whose relaxation times do not converge to length-independent values. Comparison to relaxation times predicted using the spectral energy density method with MD reveals that for a 50 unit cell, (8,8) CNT, the LD method over-predicts the relaxation times of these low-frequency acoustic modes by up to two orders of magnitude. The disagreement between the spectral energy density results and the LD predictions may be partially due to the importance of interactions involving four or more phonons, which are not included in the LD calculations. It is more likely, however, that this large discrepancy is caused by a broadening of the phonon wave vectors, observed in the spectral energy density. Like the broadening of the frequencies, which is incorporated in the anharmonic LD calculations used in this work, the broadening of the wave vectors is an artifact of finite atomic motion (anharmonicity).



## CHAPTER VI

# Quantum versus classical systems: Assessing the applicability of quantum corrections to classical thermal transport predictions

### 6.1 Introduction to quantum corrections

Classical MD simulation is a powerful tool for predicting physical behavior and material properties [137–139]. As a general rule, MD simulations of solids are considered valid near and above a material’s Debye temperature, where all of the vibrational modes (*i.e.*, phonons in a crystal) are fully excited. Molecular dynamics simulations are not valid at lower temperatures, where quantum effects cannot be neglected. To mitigate this limitation, quantum corrections (QCs) have been developed. The purpose of QCs is to map predictions made for a classical system onto corresponding values in a quantum system. Quantum corrections have been derived from first principles for thermodynamic, mechanical, and structural properties (*e.g.*, Helmholtz free energy, entropy, bulk modulus, and pair distribution function) [140–142]. Rigorous QCs for transport properties such as thermal conductivity are more difficult to obtain [143].

The commonly-used QCs for thermal conductivity are based on *ad-hoc* physical arguments rather than fundamental theory. These QCs are applied to the temperature,  $T$ , and the thermal conductivity,  $k$  [144, 145]. The temperature correction is

made by equating the total energies of the classical and quantum systems. The energy equality can be expressed as

$$\sum_{\boldsymbol{\kappa}, \nu}^{N, 3n} E^{\text{C}}(\boldsymbol{\kappa}_{\nu}) = \sum_{\boldsymbol{\kappa}, \nu}^{N, 3n} E^{\text{Q}}(\boldsymbol{\kappa}_{\nu}), \quad (6.1)$$

where the sums are over all phonon modes denoted by  $N$  wave vectors,  $\boldsymbol{\kappa}$ , and  $3n$  dispersion branches,  $\nu$ ,  $E(\boldsymbol{\kappa}_{\nu})$  is the energy of a phonon mode, and the superscripts C and Q indicate classical and quantum. By assuming (i) equipartition of the classical energy and subtracting the three translational degrees of freedom and (ii) the quantum energy to be harmonic, Eq. (6.1) becomes

$$3(Nn - 1)k_{\text{B}}T^{\text{C}} = \sum_{\boldsymbol{\kappa}, \nu}^{N, 3n} \left[ \hbar\omega(\boldsymbol{\kappa}_{\nu}) f_0^{\text{Q}}(\boldsymbol{\kappa}_{\nu}) + \frac{\hbar\omega(\boldsymbol{\kappa}_{\nu})}{2} \right]. \quad (6.2)$$

The term  $\hbar\omega(\boldsymbol{\kappa}_{\nu})/2$  is the zero-point (ZP) energy. The ZP energy has no parallel in a classical system, and, as will be shown, plays an important role in the QCs. Equation (6.2) cannot be explicitly solved for  $T^{\text{Q}}$ , but  $T^{\text{Q}}$  can be determined by computing  $T^{\text{C}}$  for a series of  $T^{\text{Q}}$  values and then interpolating.

The thermal conductivity correction is

$$k^{\text{Q}} = k^{\text{C}} \frac{dT^{\text{C}}}{dT^{\text{Q}}}, \quad (6.3)$$

which arises from equating the heat fluxes obtained from the Fourier law in the classical and quantum systems. The QCs given by Eqs. (6.2) and (6.3) have been applied to classical MD thermal conductivity predictions for amorphous silicon [145], crystalline silicon in bulk [146–148] and thin films [13],  $\beta$ -silicon carbide [149], silicon-germanium superlattices [102], carbon nanotubes [22], and transition metals (the phonon contribution) [150].

The validity of Eqs. (6.2) and (6.3) is questionable as they are not derived from fundamental relations and have not been rigorously tested. The doubts regarding

these QCs are further exemplified by the non-consensus on whether to include the ZP energy in Eq. (6.2) or to ignore it [89]. The objective of this Chapter is to rigorously assess the validity of the QCs for thermal conductivity given by Eqs. (6.2) and (6.3). To do so, the classical and quantum thermal conductivities of isotopically-pure, crystalline silicon modeled with the SW potential [104] is self-consistently predicted via lattice dynamics calculations between temperatures of 10 and 1000 K. Then the QCs are applied to the classical predictions and their accuracy is directly assessed. While the low-temperature approximations inherent in the LD techniques cause them to lose accuracy at high temperature, the quantum and classical thermal conductivity predictions remain self-consistent [71]. The QCs are found to be invalid. The reasons for the failure of the QCs are explained by using phonon properties obtained from the LD calculations.

## 6.2 Assessing the quantum corrections

### 6.2.1 Quantum and classical thermal conductivity

The SW silicon thermal conductivities predicted using the LD method are plotted in Fig. 6.1 for the quantum and classical systems between temperatures of 10 and 1000 K. The calculations are performed on the eight-atom unit cell arrayed on a simple cubic,  $N_0 \times N_0 \times N_0$  lattice. The lattice parameter is set to 5.43 Å, which is within 0.4% of the MD-predicted lattice parameters at all temperatures considered [151]. To achieve size-independent thermal conductivity predictions,  $N_0 = 12$  is used for temperatures above 100 K and  $N_0 = 30$  is used for lower temperatures. As is seen in Fig. 6.1, the quantum and classical predictions converge at high temperature, as they must. The low-temperature thermal conductivity behavior is also as expected. The quantum thermal conductivity peaks at a temperature of 30 K then

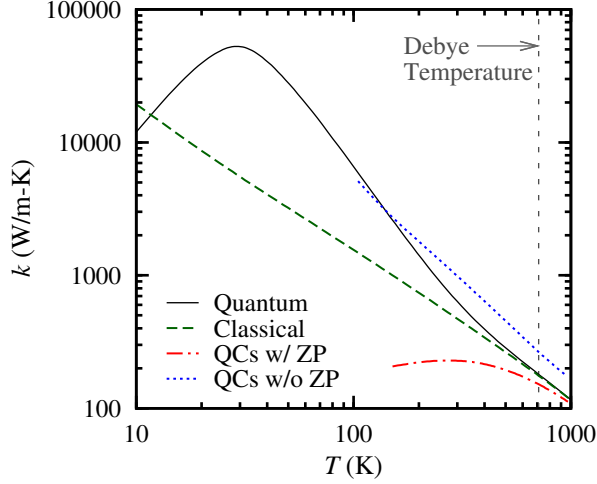


Figure 6.1: Thermal conductivity predictions for the quantum and classical systems and the quantum-corrected classical prediction using the ZP energy (QCs w/ ZP) and neglecting it (QCs w/o ZP). Reprinted with permission from [72]. Copyright *Physical Review B* 2009.

approaches zero as the temperature goes to zero. The classical thermal conductivity prediction increases monotonically as the temperature decreases and diverges to infinity at zero-temperature. For temperatures less than 100 K, phonon scattering from defects, isotopes, and boundaries is important [76]. We have neglected these scattering mechanisms, resulting in very large thermal conductivity values at these temperatures. We note that Broido *et al.* [76] predicted the thermal conductivity of SW silicon using an approach related to the LD method presented here with these additional scattering mechanisms included.

For temperatures above 15 K, the classical thermal conductivities are less than the quantum values. This result is not necessarily intuitive because the classical phonon specific heats are always greater than their quantum counterparts and, according to Eq. (2.11), will tend to increase the classical thermal conductivity over the quantum value. The thermal conductivity, however, is also affected by the group velocities and the relaxation times. Because SW silicon is a stiff material, the group velocities for

the quantum and classical systems are nearly identical and show weak temperature dependence. The relaxation times, however, have a large impact.

Plotted in Fig. 6.2 are the phonon linewidths versus harmonic frequency at a temperature of 100 K. At frequencies below 80 rad/ps, the quantum phonons have smaller linewidths than the classical phonons. At higher frequencies, the situation is reversed. By considering the equation for the linewidth [Eq. (2.23)], one sees that two types of phonon interactions contribute to  $\Gamma(\kappa)$ . One is the decay of the phonon  $\omega(\kappa)$  into two phonons [ $\omega(\kappa) \rightarrow \omega(\kappa') + \omega(\kappa'')$ , a type I interaction]. The other is the annihilation of the phonon with a second to create a third [ $\omega(\kappa) + \omega(\kappa') \rightarrow \omega(\kappa'')$  or  $\omega(\kappa) + \omega(\kappa'') \rightarrow \omega(\kappa')$ , a type II interaction]. The differences between the quantum and classical linewidths are driven by the occupation numbers,  $f_0^Q$  and  $f_0^C$ , which weight the phonon interactions. For the quantum and classical systems, the type I interactions are weighted by  $f_0^Q(\kappa') + f_0^Q(\kappa'') + 1$  and  $f_0^C(\kappa') + f_0^C(\kappa'')$ . Of these two weighting factors, the quantum expression is always greater than the classical expression for the same set of frequencies at the same temperature. The type II weighting factor for the quantum system,  $f_0^Q(\kappa') - f_0^Q(\kappa'')$ , is always less than its classical counterpart,  $f_0^C(\kappa') - f_0^C(\kappa'')$ . Energy conservation, enforced by the Dirac delta functions in Eq. (2.23), causes type I interactions to dominate when  $\omega(\kappa)$  is large, resulting in quantum linewidths that are greater than their classical counterparts. When  $\omega(\kappa)$  is small, type II interactions dominate, giving rise to quantum linewidths that tend to be smaller than the classical values. At intermediate frequencies, both type I and type II interactions play an important role. This discussion illustrates an important point, which is that the relaxation time for a single phonon mode depends strongly on the other phonon modes in the system.

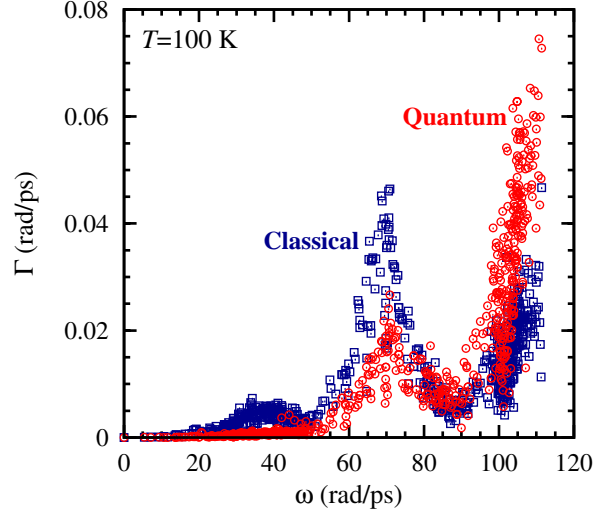


Figure 6.2: Phonon linewidths ( $\Gamma = \frac{1}{2\tau}$ ) plotted versus harmonic frequency for quantum and classical systems at a temperature of 100 K. Reprinted with permission from [72]. Copyright *Physical Review B* 2009.

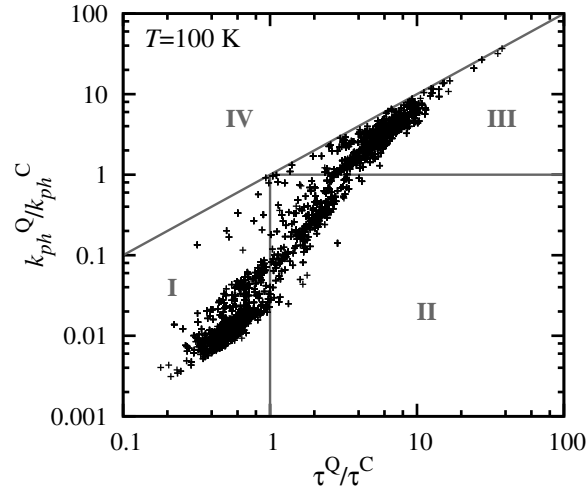


Figure 6.3: Ratio of the quantum to classical phonon thermal conductivities plotted versus the relaxation time ratio for all phonon modes at a temperature of 100 K. Reprinted with permission from [72]. Copyright *Physical Review B* 2009.

To explore the consequences of the different relaxation times on the thermal conductivity, consider Fig. 6.3 where the ratio of the mode-dependent thermal conductivities,  $k_{ph}^Q/k_{ph}^C [= c_{ph}^Q(v_{g,x}^Q)^2\tau^Q/c_{ph}^C(v_{g,x}^C)^2\tau^C]$ , is plotted against the ratio of the relaxation times,  $\tau^Q/\tau^C$ , at a temperature of 100 K. One can identify four regions separated by the lines  $k_{ph}^Q/k_{ph}^C = 1$ ,  $\tau^Q/\tau^C = 1$ , and  $k_{ph}^Q/k_{ph}^C = \tau^Q/\tau^C$ . Region IV is inaccessible because the quantum specific heat is always lower than the classical specific heat. In regions I and II, the mode-dependent quantum thermal conductivity is lower than the classical value, despite the quantum relaxation time being larger than the classical relaxation time in region II. For phonon modes in region III, the quantum relaxation time is so much larger than the classical value that it negates the reduction caused by the specific heat. The net result in this region is that the mode-dependent quantum thermal conductivity is larger than the classical value. For temperatures above 15 K, the phonons in region III dominate the thermal transport, causing the total quantum thermal conductivity to be greater than the classical prediction (see Fig. 6.1).

### 6.2.2 Quantum-corrected thermal conductivity

The temperature mapping from the classical system to the quantum system defined by Eq. (6.2) is plotted in Fig. 6.4 when the ZP energy is both considered and neglected. Also plotted is the scaling factor  $dT^C/dT^Q$  defined by Eq. (6.3). This factor is independent of the ZP energy and is always less than one. The scaling factor can be written as

$$\frac{dT^C}{dT^Q} = \frac{1}{3(Nn-1)k_B} \sum_{\kappa,\nu}^{N,3n} c_{ph}^Q(\kappa)_\nu, \quad (6.4)$$

which is obtained by differentiating Eq. (6.2) with respect to  $T^Q$  and assuming the phonon frequencies to be temperature-independent. The temperature mapping depends strongly on the inclusion or exclusion of the ZP energy. For the same quantum

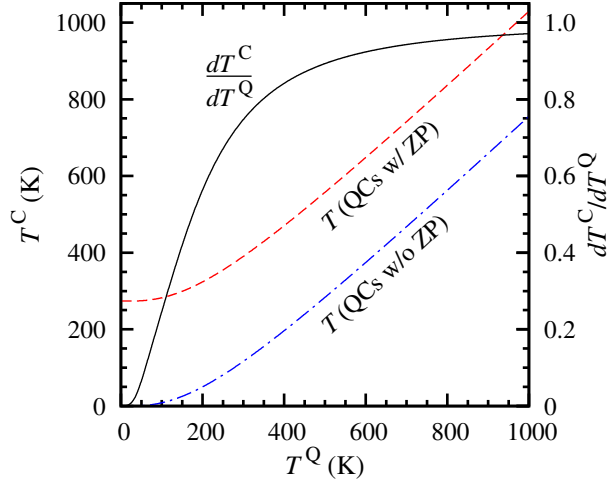


Figure 6.4: Mapping between quantum and classical temperatures with and without the ZP energy and  $dT^C/dT^Q$  as defined by Eqs. (6.2) and (6.3). Reprinted with permission from [72]. Copyright *Physical Review B* 2009.

temperature, the classical temperatures for the two cases are offset by the average ZP energy divided by  $k_B$ , which is 270 K for SW silicon. When the ZP energy is included, the corrected temperature is greater than the quantum temperature, the corrected and quantum temperatures converge in the high-temperature (*i.e.* classical) limit, and a classical system below a temperature of 270 K has no quantum counterpart. When the ZP energy is excluded, the corrected temperature is less than the quantum temperature and the corrected and quantum temperatures do not converge in the high-temperature limit, but are separated by 270 K.

The effect of the QCs on the classical thermal conductivity prediction is shown in Fig. 6.1, where we plot the quantum-corrected classical predictions. Neglecting the ZP energy increases the thermal conductivity. Including the ZP energy causes the thermal conductivity to shift downward, away from the quantum predictions.

For QCs to be valid, the corrected classical predictions must (i) converge to the quantum predictions at high temperature and (ii) provide a better estimation of



the quantum thermal conductivity than the uncorrected classical predictions. The four sets of results (quantum, classical, and two sets of quantum-corrected classical values) do converge at high temperature, though the convergence is slow for both sets of quantum-corrected values. At the SW silicon Debye temperature of 710 K [20], the corrected thermal conductivities with and without the ZP energy are 10% lower and 30% higher than the quantum value, while the uncorrected classical prediction is within 5% of the quantum value. At a temperature of 300 K, less than half the Debye temperature, the classical prediction is still within 15% of the quantum value. For temperatures above 200 K, neither of the QC approaches improves upon the agreement between the uncorrected classical value and the quantum value.

When including the ZP energy, a maximum in the thermal conductivity is predicted. The location and magnitude of this maximum, however, are clearly wrong. The lowest uncorrected temperature we consider is 10 K, which corresponds to a temperature of 105 K for the QCs without the ZP energy. The quantum-corrected thermal conductivity predictions without the ZP energy can be extended to lower temperatures by fitting a power function to the uncorrected classical predictions and extrapolating. In doing so (not shown), the quantum-corrected thermal conductivity does not exhibit a maximum when the ZP energy is neglected. From these observations, it is concluded that the QCs prescribed by Eqs. (6.2) and (6.3), with the ZP energy either included or neglected, do not properly account for quantum effects. These QCs even fail at high temperatures, where quantum effects are small.

### 6.2.3 Analyzing the quantum corrections

The reasons why the QCs given by Eqs. (6.2) and (6.3) fail can be deduced by considering the mode-dependence of the phonon properties ( $\omega$ ,  $c_{ph}$ ,  $v_{g,x}$ , and  $\tau$ ). In Fig.

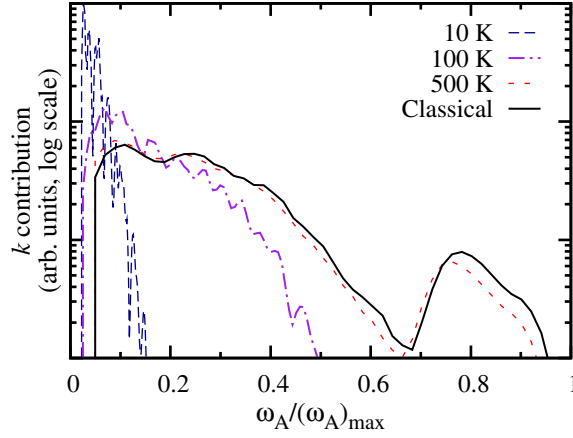


Figure 6.5: Scaled contribution to the thermal conductivity as a function of frequency ratio. The classical results at all temperatures collapse to a single curve. Reprinted with permission from [72]. Copyright *Physical Review B* 2009.

6.5, the contribution to the thermal conductivity is plotted versus phonon frequency, both scaled by their maximum values, for temperatures of 10, 100, and 500 K. When plotted this way, the results for the classical systems collapse to a single, temperature-independent curve. For the quantum system, however, the low-frequency phonons increasingly dominate the thermal conductivity as the temperature decreases. This effect is due to the temperature-dependence of the occupation number, which effectively freezes out the high-frequency modes at low temperatures. Applying the QCs given by Eqs. (6.2) and (6.3) shifts the thermal conductivity by a temperature-dependent scale factor. Yet, from Fig. 6.5 it can be seen that the frequency-dependence of the mode contribution is strongly temperature-dependent. The thermal conductivity thus cannot be properly corrected by applying a system-level scaling factor.

The reasons why the QCs fail are further addressed by investigating what would need to be done to properly correct a classically-predicted thermal conductivity. From the discussion in the previous paragraph, it is known that QCs must be performed on the level of the phonon modes [*i.e.*, the terms inside the summation in Eq. (2.11)]. To

simplify the analysis, the assumption of a temperature-independent lattice constant is retained. It is also assumed that the frequency shift is negligible. This assumption is good for SW silicon as the root mean square of  $\Delta/\omega$  is less than 0.03 for all temperatures considered. When the frequency shift is neglected, the  $x$ -component of the group velocity becomes temperature-independent and is the same in the quantum and classical systems. The phonon specific heats and relaxation times, however, differ between the two systems. If these two mode-dependent properties can be properly quantum-corrected, then a quantum thermal conductivity could be predicted from classical phonon properties. In what follows, it is assumed that all the classical phonon properties are known. Though not typically found in a Green-Kubo [42, 80] or direct [41, 80] MD-based thermal conductivity prediction, these phonon properties can be obtained from MD simulations through normal mode analysis (see Section 2.4).

Correcting the specific heat is straight-forward. The classical specific heat is a constant and the quantum specific heat can be computed from the phonon frequency. The first step in converting the classical thermal conductivity to a quantum thermal conductivity thus involves scaling the contribution of each phonon mode by  $c_{ph}^Q/c_{ph}^C$  [103]. From Eq. (6.4), one sees that the quantum correction defined by Eq. (6.3) is on the right track in that it scales the classical thermal conductivity by the ratio of the quantum specific heat to the classical specific heat. This scaling, however, is performed on the system level, rather than on the level of the phonon modes, as is required.

The relaxation times cannot be corrected in the same manner. Using the LD approach, the effort required to compute quantum relaxation times is the same as the effort required to compute classical relaxation times. Additionally, if the quantum

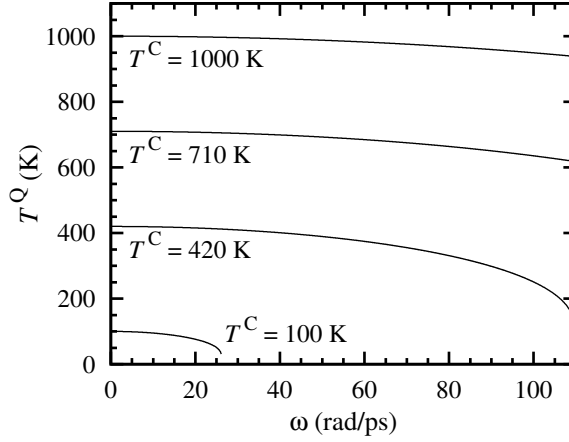


Figure 6.6: Frequency-dependent quantum temperatures as determined by Eq. (6.5) for various classical temperatures. For temperatures less than 420 K, some of the high-frequency phonons cannot be mapped into any quantum system. Reprinted with permission from [72]. Copyright *Physical Review B* 2009.

relaxation times were known, the quantum thermal conductivity could be computed directly using Eq. (2.11).

What one would like is for the classical relaxation times to be representative of the relaxation times of a corresponding quantum system. The quantum system represented by the classical relaxation times is determined by setting  $\tau^Q = \tau^C$  for each phonon mode, which is equivalent to letting  $\Gamma^Q = \Gamma^C$ . The equation for the quantum linewidth [Eq. (2.23)] can be converted to a classical linewidth by setting

$$f^C = f^Q + 1/2. \quad (6.5)$$

This condition links the quantum and classical systems. Solving Eq. (6.5) for  $T^Q$ , we find the temperature of a quantum system that has the same occupation number as the classical system to be

$$T^Q = \frac{\hbar\omega}{k_B \ln \left[ \frac{2k_B T^C + \hbar\omega}{2k_B T^C - \hbar\omega} \right]}. \quad (6.6)$$

A problem with Eq. (6.6) can be immediately seen. The quantum temperature is a function of the phonon frequency, meaning that the classical relaxation times cannot

be mapped onto an equilibrium quantum system at a single temperature. The quantum temperature corresponding to classical temperatures of 100, 420, 710, and 1000 K is plotted versus frequency in Fig. 6.6. Above the Debye temperature (710 K), the range of quantum temperatures associated with the classical temperature is small. The classical relaxation times at these temperatures are a good approximation of the quantum relaxation times, and there is no need to perform a quantum correction. As the classical temperature decreases below the Debye temperature, the range of quantum temperatures increases and the classical relaxation times are not indicative of the relaxation times of an equilibrium quantum system. When the classical temperature drops below 420 K, some of the high-frequency phonon modes cannot be mapped onto any quantum system. Though they make a small direct contribution to the thermal conductivity, these high-frequency phonons are important in that they scatter with low-frequency phonons. These mapping issues are also inherent in Eq. (6.2) (where  $T^Q$  is found as a weighted average) and contribute to the failure of the QCs.

#### 6.2.4 Discussion

Others have argued for the QCs given by Eqs. (6.2) and (6.3) because they can bring classical MD thermal conductivity predictions into better agreement with experimental measurements. When examining all the available data, however, it is found that some obtain better agreement when the ZP energy is considered [13, 22, 103, 149] while others find better agreement when the ZP energy is ignored [147, 148]. Based on the results presented in Section 6.2.3, any improved agreement is believed to be fortuitous as MD-predicted thermal conductivities are sensitive to the chosen interatomic potential. Interatomic potentials are an approximation of the complex interactions

that exist between atoms, which only *ab initio* calculations (*e.g.*, density functional theory) can accurately capture. Using an approach related to the LD method presented here, Broido and co-workers found that a fully quantum-mechanical treatment of SW silicon does not match the experimental thermal conductivity data [76], while the same treatment using input from density functional theory calculations does [152].

Alternative approaches for obtaining a quantum thermal conductivity prediction from classical MD simulations have been suggested. These approaches are based on modifying the MD simulation itself, making them fundamentally different than QCs, which are a post-processing procedure. Li suggested initializing a classical MD simulation with a phonon distribution corresponding to a quantum system at equilibrium [153]. Wang proposed a classical MD simulation that interacts with heat baths that are forced to maintain quantum phonon distributions [154]. The drawback of these approaches is that the MD simulation is limited temporally or spatially. A system with an initial quantum configuration will eventually relax to an equilibrium classical state. A large MD system in contact with quantum heat baths will have a classical phonon distribution far from the heat baths.

Quantum MD simulation (*e.g.*, Car-Parrinello [155]) in conjunction with the Green-Kubo or direct method has not been used to predict thermal conductivity because it is too computationally expensive. In spite of its name, quantum MD simulation is a classical prediction method since the nuclei obey Newton's equations of motion rather than the Schrödinger equation. A less computationally expensive approach is to use Feynman path integrals to effectively transform a quantum system into a classical system, whose static properties can then be computed using classical MD or Monte Carlo simulations [156]. Centroid MD, an extension of path-integral MD

developed by Cao and Voth [157,158], has been used to predict transport properties of quantum systems, such as thermal conductivity and shear viscosity [159].

Fully quantum-mechanical predictions of thermal conductivity, made using the LD method employed here or a related method developed by Omini and Sparavigna [74,75], are an excellent alternative to MD-based predictions for ordered systems well below the Debye temperature, where the weakly-interacting phonon model is valid. Lattice dynamics-based predictions of the thermal conductivity have the additional advantages of allowing their input to come from density functional theory calculations and providing the complete phonon properties [71]. At higher temperatures, quantum effects are unimportant and classical MD based methods are suitable if an accurate interatomic potential is available.

### 6.3 Conclusions

The validity of the commonly-used QCs for thermal conductivity [Eqs. (6.2) and (6.3)] have been assessed by using harmonic and anharmonic LD calculations to self-consistently predict the quantum and classical thermal conductivities of SW silicon. Applying the QCs to the classical predictions, with or without the ZP energy, does not bring them into better agreement with the quantum predictions compared to the uncorrected classical values above temperatures of 200 K (see Fig. 6.1). When neglecting the ZP energy, the quantum-corrected temperature does not approach the quantum temperature in the high-temperature limit and there is no maximum in the thermal conductivity. When the ZP energy is included, the corrected thermal conductivity shifts away from the quantum prediction and the location and magnitude of the maximum do not agree with the quantum results. The same behavior can be seen in Lennard-Jones argon (see Table 3.3).

The frequency dependence of the thermal conductivity (see Fig. 6.5) is examined to find that system-level properties, like those used in Eqs. (6.2) and (6.3), cannot be used to bring classical thermal conductivities into agreement with quantum values. While the specific heat can be quantum-corrected on a mode-by-mode basis, the system temperature cannot be quantum-corrected because the phonons in a classical system are not representative of the phonons in an equilibrium quantum system at a single temperature (see Fig. 6.6). Differences between the classical and quantum relaxation times (see Figs. 6.2 and 6.3) can be attributed to the frequency dependence of the occupation numbers and the dominant scattering mechanism. The mapping of classical phonons onto an equivalent quantum system is approximately correct only at high temperatures, where QCs are unnecessary.



## CHAPTER VII

### Conclusion and outlook

#### 7.1 Overview

The effective thermal conductivity of structures with dimensions on the nano-scale has been predicted [13,14,16,100] and observed [2,5,6,9,17,18,33–36] to be lower than the corresponding thermal conductivity in bulk materials. This phenomenon is due to the confinement of lattice vibrations (*i.e.*, phonons), which are the primary energy carriers in insulating materials. The thermal characterization of such structures is needed in order to model the heat transport in devices that incorporate these nano-scale structures. The ability to engineer materials on the nano-scale also gives rise to the possibility of selectively engineering the thermal properties of materials.

A fundamental understanding of the mechanisms of thermal transport in nano-structured materials and a means of determining their thermal conductivities would be invaluable in the design and characterization of these materials. Such understanding and tools are currently lacking. Measuring the thermal conductivity of structures with nano-scale dimensions experimentally would be a difficult and time consuming task due to the extremely small size of the structures and the geometry dependence of the thermal conductivity. Current numerical techniques used to predict the lattice

thermal conductivity of crystals are approximate or are computationally intensive so have had only limited success in advancing the understanding of phonon transport.

Harmonic and anharmonic LD calculations, combined with the BTE, have the potential to provide accurate predictions of the thermal conductivity of nano-structured materials and insights into the nature of phonon transport in such materials. Like the well-known MD simulation method, LD is an atomistic modeling technique. Unlike MD, which numerically integrates the equations of motion, LD utilizes several approximations to allow for an analytical solution to the equations of motion. Hence, the LD calculations have the potential to be much less computationally expensive than MD simulation but are also less accurate. The approximations made in the LD calculations, namely the assumption of small atomic motion and weak anharmonicity, are valid at low temperatures.

In Chapter III, it was shown that thermal conductivity predictions made at low temperatures ( $\leq 40\%$  of the Debye temperature) for LJ argon using the LD method are in reasonable agreement (within 30%) with MD predictions made using the direct, Green-Kubo, and normal mode analysis methods (see Fig. 3.3) [71]. As the temperature increases, both the LD and the normal mode analysis methods lose accuracy since the anharmonicity of the atomic interactions increases and the phonon normal mode coordinates become less accurate in describing the atomic motion. Because the LD method provides the basic phonon properties that give rise to the thermal conductivity, the method can be used to directly study the mechanisms of thermal transport rather than having to rely upon inferences from the thermal conductivity, which is an aggregate property. Taking advantage of this attribute of the LD method, it was shown that the isotropic approximation and assumption that low frequency phonon dominate thermal transport are not valid in LJ argon.

Thermal transport in thin films [73] and superlattices was studied using the LD method in Chapter IV. Because thin films are not periodic in the cross-plane direction, the LD method cannot be used to predict their thermal conductivities directly. Instead, bulk phonon properties were used along with a mode-dependent correction factor to account for diffuse boundary scattering. This model is accurate for films in which the phonon population is bulk-like (see Fig. 4.6). The LD-predicted thermal conductivity for LJ argon and SW silicon thin films is consistent with prediction made using the Green-Kubo MD method [13] and experimental measurements [33–36] (see Figs. 4.5 and 4.7). From the results, it was demonstrated that the thin film thermal conductivity cannot be predicted using average phonon properties of the bulk material, such as the average MFP. Lattice dynamics calculations can be directly applied to superlattices since they are fully periodic. However, the LD method enforces coherent phonon transport, thus, it incorrectly models cross-plane transport in long period superlattices. Comparison with Green-Kubo MD predictions for ideal LJ superlattices, though, indicates that the LD method can be used to predict the in-plane thermal conductivity as well as the cross-plane thermal conductivity in short period superlattices.

The phonon properties of graphene and armchair CNTs were examined in Chapter V using the Brenner REBO potential. These carbon structures have very large sound velocities, around 20,000 m/s, which contribute to the large thermal conductivities. For the (5,5) CNT, the smallest diameter CNT considered, the phonon DOS exhibits characteristics of a one dimensional system. As the CNT diameter increases, the phonon DOS approaches the DOS of graphene. This trend is also seen in the thermal conductivities predicted using the direct MD method [134]. Thermal conductivity predictions could not be made for the CNTs that were independent of the BZ resolu-

tion. Examination of the phonon mode properties revealed that the relaxation times for some of the low-frequency acoustic modes never converge to a resolution independent value though all other relaxation times do. The converged lifetimes are in agreement with predictions made using MD and the spectral energy density [82, 135]. These results suggest that the LD method could be improved by accounting for the broadening of the wave vectors that can be seen in the spectral energy density (see Fig. 5.6).

In Chapter VI, the ability of the LD method to self-consistently predict both classical and quantum thermal conductivities was used to assess the validity of QCs to MD-predicted thermal conductivities. It was found that the temperature correction and the scaling of the thermal conductivity do not properly account for quantum effects (see Fig. 6.1). If the phonon properties are corrected on a mode-by-mode basis, the quantum specific heat can be properly included in the calculation of the thermal conductivity, however, the classical relaxation times cannot be adjusted to account for quantum effects. Thus, only methods that include the proper quantum phonon distribution in the prediction of the relaxation times can be used to predict a quantum thermal conductivity.

## 7.2 Contribution

The main contribution of this work is the demonstration that mode-dependent phonon properties are vital to advancing the understanding of and accurately describing thermal transport through crystal lattices. By examining the phonon properties and their relation to the thermal conductivity in Chapter III, several approximations and assumptions commonly used to simplify models of phonon transport have been assessed in this work. The isotropic approximation and the assumption that low fre-

quency phonon modes dominate thermal transport have been shown to be incorrect for LJ argon. In this system, the relaxation times can be treated as isotropic (see Fig. 3.4) but not the velocities. The thermal conductivity of SW silicon, however, is dominated by low-frequency phonon modes (see Fig. 6.5) and can be accurately modeled using the isotropic approximation [40, 92]. The LD predictions were used in Chapter IV to show that average phonon properties in bulk materials are insufficient to describe the reduction of the thermal conductivity of thin films. Yet, this reduction can be described using mode-dependent phonon properties and a relatively simple but accurate boundary scattering relation (see Figs. 4.5 and 4.7 and Appendix C). In Chapter VI, LD-predicted phonon properties were used to show that QCs are invalid and to explain why. The phonon properties were also used to show that no post-processing procedure for quantum correcting classically predicted phonon relaxation times can be successful.

The primary contribution of demonstrating the importance of mode-dependent phonon properties was achieved by developing a formal and robust procedure for implementing LD calculations to predict all phonon properties relevant to thermal transport. Though the basic formalism for both harmonic and anharmonic LD calculations has been developed by others [50, 55, 58, 61, 160], anharmonic LD calculations have been rarely utilized [64–66, 70], particularly in the recent past. Such little interest in using the anharmonic LD method to study lattice thermal transport is most likely due to a combination of obscurity, relative complexity, and challenges in implementing the method. The work presented here has been disseminated in peer-reviewed journals (references [71–73]) which serves to lessen the method’s obscurity. The complexity of the anharmonic LD method cannot be reduced, but by providing a complete, step-by-step derivation starting from the equations of motion, as is

done in Appendix B, the theory of anharmonic LD will be more accessible to non-experts. The most significant challenges associated with anharmonic LD have also been addressed in this work. A novel procedure for evaluating the Cauchy principal values and Dirac delta functions used to evaluate the frequency shift and linewidth was presented. Though Eqs. (2.31) and (2.32) have been used by others [55, 70], the specification of  $\epsilon$  has been *ad hoc* and constant for all interactions. Here, the choice of Eqs. (2.31) and (2.32) and the interaction-dependent prescription for  $\epsilon$ , Eq. (2.33), were motivated by the derivation of the frequency shift and linewidth equations and describe the frequency broadening of lattice vibrations. To address the effect of the finite BZ resolution an extrapolation procedure has been devised and implemented for LJ argon in bulk, ideal LJ superlattices, and graphene modeled with the Brenner REBO potential. Though this extrapolation procedure is empirical, it was found to be quite robust. With the analysis of the thin films using LD, an example of how LD calculations maybe be applied to non-periodic structures has also been provided.

### 7.3 Future work and outlook

The LD method has the major benefit of providing the complete phonon properties and relating these directly to the thermal conductivity. The LD method is also much less computationally expensive than the MD method for systems with few atoms in the unit cell and the LD calculations are trivial to parallelize. For example, the LD predictions of the thermal conductivities of the bulk crystals, thin films, and graphene, all of which have few atoms in the unit cell, take orders of magnitude less computational effort than MD-based thermal conductivity predictions of the same systems. A parallel algorithm has been used for the superlattices and CNTs, which are computationally expensive because of the large number of atoms in the unit

cells. This parallel algorithm simply assigns a portion of the BZ to each processor, which computes the properties of all phonons in that region. The ability to rapidly predict the thermal conductivity along with the phonon properties would be valuable in designing nano-structures with unique thermal properties.

Other advantages of the LD method are that it can provide predictions for a quantum system and the input required to make the calculations can be determined from density functional theory calculations. These characteristics allow the LD method to be used to make *ab initio* predictions of phonon properties and the thermal conductivity for a quantum system. The only other method with this ability is the closely related method of Omini and Sparavigna which uses Fermi's Golden Rule to compute the phonon-phonon interaction strengths [74, 75, 77]. Broido *et al.* used this method with DFPT to make *ab initio* predictions of the thermal conductivity of silicon and germanium [152]. The full DFPT calculations has only been implemented for zinc-blende structures [161] and needs to be generalized to an arbitrary crystal lattice.

Despite the advantages of the LD method, its limitations will undoubtedly hinder its use. The low-temperature approximations inherent in the LD calculations make them inaccurate at high temperatures. Lattice dynamics calculations are also limited to crystalline materials where phonon transport is coherent. This limitation is demonstrated in the inability of the LD method to properly predict the cross-plane thermal conductivity of long period superlattices.

The correct modeling of thermal transport across superlattice interfaces using LD-based techniques should be the topic of future work. A possible strategy would be to use a LD-based method called the scattering boundary method [120, 162] to predict the transmission coefficients of phonon incident of the interface. Then the lattice Boltzmann method, or a similar method using the BTE, would be used to track the

time evolution of the phonon modes. This procedure should work well in the diffuse limit. In the transition regime, however, when the transport of phonon modes can be diffuse or ballistic, the identification and interaction of the modes in these different transport regimes is a major challenge.

The spectral energy density method of predicting the phonon properties is likely to become a valuable and widely used tool for the study of phonon transport. It is an emerging method, having only been used once to predict the thermal conductivity of a (8,8) CNT [82], and is closely related to the LD method. The spectral energy density uses the atomic displacements as determined from MD simulation to calculate the phonon frequencies and relaxation times. Therefore, the spectral energy density includes the full effect of anharmonicity, not just the low-order anharmonicities as in the LD method, but is purely classical. The anharmonicity still needs to be weak in order to use the spectral energy density method, though, otherwise the peaks in the function will not be Lorentzian in form. The spectral energy density may also be useful in systems where the LD method is difficult to implement, such as near an interface or in a non-periodic system. Perhaps the most exciting aspect of the spectral energy density is that it has been suggested that the timescale and lengthscale needed to obtain good statistics using the spectral energy density are short enough that the method may be used with quantum MD simulation. Thus, with a combination of the LD and the spectral energy methods, quantum and classical *ab initio* thermal conductivity predictions can be made over a wide temperature range.



## BIBLIOGRAPHY

## BIBLIOGRAPHY

- [1] David G. Cahill, K. E. Goodson, and Arunava Majumdar. Thermometry and thermal transport in micro/nanoscale solid-state devices and structures. *ASME Journal of Heat Transfer*, 124(2):223–241, 2002.
- [2] David G. Cahill, Wayne K. Ford, Kenneth E. Goodson, Gerald D. Mahan, Arun Majumdar, Humphrey J. Maris, Roberto Merlin, and Simon R. Phillpot. Nanoscale thermal transport. *Journal of Applied Physics*, 93(2):793–818, 2003.
- [3] G Chen. Nanoscale heat transfer and information technology. *Rohsenow Symposium on Future Trends of Heat Transfer*, page 3, 2003.
- [4] Eric Pop and K. E. Goodson. Thermal phenomena in nanoscale transistors. *ASME Journal of Electronic Packaging*, 128:102–108, 2006.
- [5] K. E. Goodson, L. Jiang, S. Sinha, Eric Pop, and S. Im. Microscale thermal engineering of electronic systems. In *Rohsenow Symposium on Future Trends of Heat Transfer*, Cambridge, MA, 2003.
- [6] A. D. McConnell and K.E. Goodson. Thermal conduction in silicon micro- and nanostructures. *Annual Review of Heat Transfer*, 14:129–168, 2005.
- [7] G. Chen and M. Neagu. Thermal conductivity and heat transfer in superlattices. *Applied Physics Letters*, 71(19):2761, 1997.
- [8] F. J. DiSalvo. Thermoelectric cooling and power generation. *Science*, 285(5428):703–706, 1999.
- [9] T. Borca-Tasciuc, W. Liu, J. Liu, T. Zeng, D. Song, C. Moore, G. Chen, K. Wang, and M. Goorsky. Thermal conductivity of symmetrically strained si/ge superlattices. *Superlattices and Microstructures*, 28(3):199–206, 2000.
- [10] Scott T. Huxtable, Alexis R. Abramson, Chang-Lin Tien, Arun Majumdar, Chris LaBounty, Xiaofeng Fan, Gehong Zeng, John E. Bowers, Ali Shakouri, and Edward T. Croke. Thermal conductivity of Si/SiGe and SiGe/SiGe superlattices. *Applied Physics Letters*, 80(10):1737–1739, 2002.
- [11] G Chen, M. S. Dresselhaus, G. Dresselhaus, J. P. Fleurial, and T. Caillat. Recent developments in thermoelectric materials. *International materials reviews*, 48(1):45–66, 2003.
- [12] M.S. Dresselhaus, G. Chen, M.Y. Tang, R.G. Yang, H. Lee, D.Z. Wang, Z.F. Ren, J.-P. Fleurial, and P. Gogna. New directions for low-dimensional thermoelectric materials. *Advanced Materials*, 19(8):1043–1053, 2007.
- [13] Carlos J. Gomes, Marcela Madrid, Javier V. Goicochea, and Cristina H. Amon. In-plane and out-of-plane thermal conductivity of silicon thin films predicted by molecular dynamics. *Journal of Heat Transfer*, 128:1114–1121, 2006.

- [14] P. Heino. Dispersion and thermal resistivity in silicon nanofilms by molecular dynamics. *The European Physical Journal B - Condensed Matter and Complex Systems*, 60(2):171–179, 2007.
- [15] D. Baillis and J. Randrianalisoa. Prediction of thermal conductivity of nanostructures: Influence of phonon dispersion approximation. *International Journal of Heat and Mass Transfer*, 52(11-12):2516–2527, 2009.
- [16] N. Mingo. Calculation of Si nanowire thermal conductivity using complete phonon dispersion relations. *Physical Review B*, 68(11):113308, 2003.
- [17] S.-M. Lee, David G. Cahill, and Rama Venkatasubramanian. Thermal conductivity of Si–Ge superlattices. *Applied Physics Letters*, 70(22):2957–2959, 1997.
- [18] S. Chakraborty, C. A. Kleint, A. Heinrich, C. M. Schneider, J. Schumann, M. Falke, and S. Teichert. Thermal conductivity in strain symmetrized Si/Ge superlattices on Si(111). *Applied Physics Letters*, 83(20):4184–4186, 2003.
- [19] D. A. Broido and T. L. Reinecke. Lattice thermal conductivity of superlattice structures. *Physical Review B*, 70(8):081310, 2004.
- [20] E. S. Landry and A. J. H. McGaughey. Effect of interfacial species mixing on phonon transport in semiconductor superlattices. *Physical Review B*, 79(7):075316–075318, 2009.
- [21] M. Grujicic, G. Cao, and Walter N. Roy. Computational analysis of the lattice contribution to thermal conductivity of single-walled carbon nanotubes. *Journal of Materials Science*, 40(8):1943–1952, 2005.
- [22] Jennifer R. Lukes and Hongliang Zhong. Thermal conductivity of individual single-wall carbon nanotubes. *Journal of Heat Transfer*, 129(6):705–716, 2007.
- [23] Junichiro Shiomi and Shigeo Maruyama. Diffusive-ballistic heat conduction of carbon nanotubes and nanographene ribbons. *International Journal of Thermophysics*, 2008.
- [24] Deyu Li, Scott T. Huxtable, Alexis R. Abramson, and Arun Majumdar. Thermal transport in nanostructured solid-state cooling devices. *Journal of Heat Transfer*, 127(1):108–114, 2005.
- [25] J. D. Chung, A. J. H. McGaughey, and M. Kaviani. Role of phonon dispersion in lattice thermal conductivity modeling. *Journal of Heat Transfer*, 126(3):376–380, 2004.
- [26] Terry M. Tritt, editor. *Thermal Conductivity Theory, Properties, and Applications*. Physics of Solids and Liquids. Kluwer Academic/Plenum Publishers, New York, 2004.
- [27] J M Ziman. *Electrons and Phonons: The Theory of Transport Phenomena in Solids*. Clarendon Press, Oxford, 1960.
- [28] R. E. Peierls. *Quantum Theory of Solids*. The International Series of Monographs on Physics. Clarendon press, Oxford, 1955.
- [29] P. G. Klemens. The thermal conductivity of dielectric solids at low temperatures (theoretical). *Proceedings of the Royal Society of London. Series A, Mathematical and Physical Sciences*, 208(1092):108–133, 1951.
- [30] Joseph Callaway. Model for lattice thermal conductivity at low temperatures. *Physical Review*, 113(4):1046–1051, 1959.
- [31] M. G. Holland. Analysis of lattice thermal conductivity. *Physical Review*, 132(6):2461–2471, 1963.
- [32] M. G. Holland. Phonon scattering in semiconductors from thermal conductivity studies. *Physical Review*, 134(2A):A471–A480, 1964.

- [33] M. Asheghi, Y.K. Leung, S.S. Wong, and K.E. Goodson. Phonon-boundary scattering in thin silicon layers. *Applied Physics Letters*, 71(13):1798, 1997.
- [34] Y. S. Ju and K. E. Goodson. Phonon scattering in silicon films with thickness of order 100 nm. *Applied Physics Letters*, 74(20):3005–3007, 1999.
- [35] W. Liu and M. Asheghi. Phonon-boundary scattering in ultrathin single-crystal silicon layers. *Applied Physics Letters*, 84(19):3819–3821, 2004.
- [36] Wenjun Liu and Mehdi Asheghi. Thermal conductivity measurements of ultra-thin single crystal silicon layers. *Journal of Heat Transfer*, 128(1):75–83, 2006.
- [37] Peter Carruthers. Theory of thermal conductivity of solids at low temperatures. *Reviews of Modern Physics*, 33(1):92–138, 1961.
- [38] Sreekant V.J. Narumanchi, Jayathi Y. Murthy, and Cristina H. Amon. Submicron heat transport model in silicon accounting for phonon dispersion and polarization. *Journal of Heat Transfer*, 126(6):946–955, 2004.
- [39] Alan J. H. McGaughey and M. Kaviani. Quantitative validation of the Boltzmann transport equation phonon thermal conductivity model under the single-mode relaxation time approximation. *Physical Review B*, 69(9):094303, 2004.
- [40] D. P. Sellan, E. S. Landry, J. E. Turney, A. J. H. McGaughey, and C. H. Amon, Predicting thin film phonon thermal conductivity using anharmonic lattice dynamics calculations and the lattice Boltzmann method. In preparation.
- [41] J.R. Lukes, D.Y. Li, X.-G. Liang, and C.-L. Tien. Molecular dynamics study of solid thin-film thermal conductivity. *Journal of Heat Transfer*, 122(3):536–543, 2000.
- [42] Hideo Kaburaki, Ju Li, Sidney Yip, and Hajime Kimizuka. Dynamical thermal conductivity of argon crystal. *Journal of Applied Physics*, 102(4):043514–043516, 2007.
- [43] G. D. Mahan. Quantum Boltzmann equation for photons. *Journal of Mathematical Physics*, 37(9):4333–4351, 1996.
- [44] M. Liebendörfer, M. Rampp, H.-Th. Janka, and A. Mezzacappa. Supernova simulations with Boltzmann neutrino transport: A comparison of methods. *The Astrophysical Journal*, 620:840–860, 2005.
- [45] S. Aoki. Hydrodynamics of a highly flattened galaxy, based on the collisionless Boltzmann equation. *Astronomy and Astrophysics*, 148(1):1–11, 1985.
- [46] G. P. Srivastava. *The Physics of Phonons*. Adam Hilger, Bristol, 1990.
- [47] N. W. Ashcroft and N. D. Mermin. *Solid State Physics*. Saunders College Publishing, Fort Worth, 1976.
- [48] M. Asheghi, K. Kurabayashi, R. Kasnavi, and K. E. Goodson. Thermal conduction in doped single-crystal silicon films. *Journal of Applied Physics*, 91(8):5079–5088, 2002.
- [49] Y. Sungtaek Ju. Phonon heat transport in silicon nanostructures. *Applied Physics Letters*, 87(15):153106–153103, 2005.
- [50] Max Born and Kun Huang. *Dynamical Theory of Crystal Lattices*. Clarendon Press, Oxford, 1954.
- [51] C. Kittel. *Introduction to Solid State Physics*. Wiley, New york, 6th edition, 1986.

- [52] H. Zhao, Z. Tang, G. Li, and N.R. Aluru. Quasiharmonic models for the calculation of thermodynamic properties of crystalline silicon under strain. *Journal of Applied Physics*, 99(6):064314, 2006.
- [53] Martin T. Dove. *Introduction to Lattice Dynamics*. Cambridge University Press, Cambridge, UK, 1993.
- [54] A. J. H. McGaughey, M. I. Hussein, E. S. Landry, M. Kaviani, and G. M. Hulbert. Phonon band structure and thermal transport correlation in a layered diatomic crystal. *Physical Review B*, 74(10):104304–104301, 2006.
- [55] A. A. Maradudin and A. E. Fein. Scattering of neutrons by an anharmonic crystal. *Physical Review*, 128(6):2589–2608, 1962.
- [56] M. L. Klein, G. K. Horton, and J. L. Feldman. Thermodynamic properties of solid Ar, Kr, and Xe based upon a short-range central force and the conventional perturbation expansion of the partition function. *Physical Review*, 184(3):968–978, 1969.
- [57] R. A. Cowley. Anharmonic crystals. *Reports of Progress in Physics*, 31:123–166, 1968.
- [58] J. J. J. Kokkedee. Anharmonic effects in the coherent scattering of neutrons by crystals : A formal treatment of shift and width of the peaks in the scattering spectrum. *Physica*, 28(4):374–408, 1962.
- [59] A. A. Maradudin and P. A. Flinn. Anharmonic contributions to the Debye-Waller factor. *Physical Review*, 129(6):2529–2547, 1963.
- [60] J. A. Reissland. *The Physics of Phonons*. John Wiley & Sons, New York, 1973.
- [61] Duane C. Wallace. *Thermodynamics of Crystals*. John Wiley & Sons, New York, 1972.
- [62] T. R. Koehler, N. S. Gillis, and Duane C. Wallace. Anharmonic interaction in aluminum. I. *Physical Review B*, 1(12):4521–4528, 1970.
- [63] N. S. Gillis and T. R. Koehler. Anharmonic interactions in aluminum. II. *Physical Review B*, 3(10):3568–3571, 1971.
- [64] H. R. Glyde and Roger Taylor. Anharmonic lattice dynamics in Na. *Physical Review B*, 5(4):1206–1213, 1972.
- [65] H. R. Glyde and M. G. Smoes. Phonons in solid argon. *Physical Review B*, 22(12):6391–6402, 1980.
- [66] Henry R. Glyde and Roger Taylor. Anharmonic phonons in Cs. *Physical Review B*, 25(10):6500–6503, 1982.
- [67] Stefano Baroni, Stefano de Gironcoli, Andrea Dal Corso, and Paolo Giannozzi. Phonons and related crystal properties from density-functional perturbation theory. *Reviews of Modern Physics*, 73(2):515–562, 2001.
- [68] Alberto Debernardi, Stefano Baroni, and Elisa Molinari. Anharmonic phonon lifetimes in semiconductors from density-functional perturbation theory. *Physical Review Letters*, 75(9):1819–1822, 1995.
- [69] G. Deinzer, G. Birner, and D. Strauch. *Ab Initio* calculation of the linewidth of various phonon modes in germanium and silicon. *Physical Review B*, 67(14):144304, 2003.
- [70] Anthony J. C. Ladd, Bill Moran, and William G. Hoover. Lattice thermal conductivity: A comparison of molecular dynamics and anharmonic lattice dynamics. *Physical Review B*, 34(8):5058–5064, 1986.

- [71] J. E. Turney, E. S. Landry, A. J. H. McGaughey, and C. H. Amon. Predicting phonon properties and thermal conductivity from anharmonic lattice dynamics calculations and molecular dynamics simulations. *Physical Review B*, 79(6):064301–064312, 2009.
- [72] J. E. Turney, A. J. H. McGaughey, and C. H. Amon. Assessing the applicability of quantum corrections to classical thermal conductivity predictions. *Physical Review B*, 79(22):224305–224307, 2009.
- [73] J. E. Turney, A. J. H. McGaughey, and C. H. Amon, In-plane phonon transport in thin films. In review.
- [74] M. Omini and A. Sparavigna. An iterative approach to the phonon Boltzmann equation in the theory of thermal conductivity. *Physica B*, 212(2):101–112, 1995.
- [75] M. Omini and A. Sparavigna. Beyond the isotropic-model approximation in the theory of thermal conductivity. *Physical Review B*, 53(14):9064–9073, 1996.
- [76] D. A. Broido, A. Ward, and N. Mingo. Lattice thermal conductivity of silicon from empirical interatomic potentials. *Physical Review B*, 72(1):014308, 2005.
- [77] M. Omini and A. Sparavigna. Heat transport in dielectric solids with diamond structure. *Nuovo Cimento Della Societa Italiana Di Fisica. D*, 19(10):1537, 1997.
- [78] J. M. Haile. *Molecular Dynamics Simulation: Elementary Methods*. John Wiley and Sons, Inc., New York, 1992.
- [79] Arun Majumdar. Microscale energy transport in solids. In C.-L. Tien, Arun Majumdar, and F. M. Gerner, editors, *Microscale Energy Transport*, page 72. Taylor and Francis, Washington, 1998.
- [80] Patrick K. Schelling, Simon R. Phillpot, and Pawel Keblinski. Comparison of atomic-level simulation methods for computing thermal conductivity. *Physical Review B*, 65(14):144306, 2002.
- [81] D. P. Sellan, E. S. Landry, J. E. Turney, A. J. H. McGaughey, and C. H. Amon, Size effects in molecular dynamics thermal conductivity predictions. In preparation.
- [82] J. A. Thomas, J. E. Turney, R. M. Iutzi, A. J. H. McGaughey, and C. H. Amon, Predicting phonon dispersion relations and lifetimes from the spectral energy density. In review.
- [83] J. A. Thomas, *Water Flow and Heat Transfer through Carbon Nanotubes*. Ph.D. thesis, Carnegie Mellon University, Pittsburgh, Pennsylvania, In preparation.
- [84] Patrice Chantrenne and Jean-Louis Barrat. Finite size effects in determination of thermal conductivities: Comparing molecular dynamics results with simple models. *Journal of Heat Transfer*, 126(4):577–585, 2004.
- [85] E. S. Landry, M. I. Hussein, and A. J. H. McGaughey. Complex superlattice unit cell designs for reduced thermal conductivity. *Physical Review B*, 77(18):184302–184313, 2008.
- [86] Hideo Kaburaki, Ju Li, and Sidney Yip. Thermal conductivity of solid argon by classical molecular dynamics. In *Materials Research Society Symposium*, volume 538, pages 503–508, Boston, MA, USA, 1998. Materials Research Society, Warrendale, PA, USA.
- [87] David R. Lide, editor. *CRC Handbook of Chemistry and Physics*. CRC Press/Taylor and Francis, Boca Raton, FL, 88 (internet version 2008) edition, 2008.
- [88] A. J. H. McGaughey and M. Kaviani. Thermal conductivity decomposition and analysis using molecular dynamics simulations: Part I. Lennard-Jones argon. *International Journal of Heat and Mass Transfer*, 47(8-9):1783–1798, 2004.

- [89] Alan J. H. McGaughey. *Phonon Transport in Molecular Dynamics Simulations: Formulation and Thermal Conductivity Prediction*. Ph.D. thesis, University of Michigan, Ann Arbor, Michigan, 2004.
- [90] Lev Kantorovich. *Quantum Theory of the Solid State: An Introduction*, volume 136 of *Fundamental Theories of Physics*. Kluwer Academic Publishers, Dordrecht, 2004.
- [91] In their paper, McGaughey and Kaviani [39] incorrectly take the decay constant to be half the relaxation time. Here, their reported relaxation times and thermal conductivities are divided by two to correct for the error.
- [92] Asegun S. Henry and Gang Chen. Spectral phonon transport properties of silicon based on molecular dynamics simulations and lattice dynamics. *Journal of Computational and Theoretical Nanoscience*, 5(2):1–12, 2008.
- [93] Denzil Roberts and Gregory Triplett. Tuning nonlinear susceptibility in strained AlGaAs/InGaAs quantum cascade lasers. *Solid-State Electronics*, 52(10):1669–1673, 2008.
- [94] Dongshe Zhang, Jonathan A. Downing, Fritz J. Knorr, and Jeanne L. McHale. Room-temperature preparation of nanocrystalline TiO<sub>2</sub> films and the influence of surface properties on dye-sensitized solar energy conversion. *The Journal of Physical Chemistry B*, 110(43):21890–21898, 2006.
- [95] Martin Green. Polycrystalline silicon on glass for thin-film solar cells. *Applied Physics A*, 96(1):153–159, 2009.
- [96] Y.-L. Li, Y.-R. Huang, and Y.-H. Lai. Efficiency droop behaviors of InGaN/GaN multiple-quantum-well light-emitting diodes with varying quantum well thickness. *Applied Physics Letters*, 91(18):181113–181113, 2007.
- [97] H Bottner, G Chen, and Rama Venkatasubramanian. Aspects of thin-film superlattice thermoelectric materials, devices, and applications. *MRS Bulletin*, 31:211–216, 2006.
- [98] Kenneth E. Goodson and Y. Sungtaek Ju. Heat conduction in novel electronic films. *Annual Review of Materials Science*, 29(1):261–293, 1999.
- [99] Shin-ichiro Tamura, Yukihiro Tanaka, and Humphrey J. Maris. Phonon group velocity and thermal conduction in superlattices. *Physical Review B*, 60(4):2627–2630, 1999.
- [100] B. Yang and G. Chen. Partially coherent phonon heat conduction in superlattices. *Physical Review B*, 67(19):195311, 2003.
- [101] Alexis R. Abramson, Chang-Lin Tien, and Arun Majumdar. Interface and strain effects on the thermal conductivity of heterostructures: A molecular dynamics study. *Journal of Heat Transfer*, 124(5):963–970, 2002.
- [102] S. Volz, J. B. Saulnier, G. Chen, and P. Beauchamp. Computation of thermal conductivity of Si/Ge superlattices by molecular dynamics techniques. *Microelectronics Journal*, 31(9-10):815–819, 2000.
- [103] Javier V. Goicochea. *Hierarchical Modeling of Heat Transfer in Electronic Devices*. Ph.D. thesis, Carnegie Mellon University, Pittsburgh, PA, 2008.
- [104] F.H. Stillinger and T.A. Weber. Computer simulation of local order in condensed phases of silicon. *Physical Review B*, 31(8):5262–5271, 1985.
- [105] M.I. Flik and C.L. Tien. Size effect on the thermal conductivity of high-T<sub>c</sub> thin-film superconductors. *Journal of Heat Transfer*, 112(4):872–881, 1990.

- [106] A. Majumdar. Microscale heat conduction in dielectric thin films. *Journal of Heat Transfer*, 115(1):7–16, 1993.
- [107] K. Fuchs. Electron theory of the conductivity of thin metallic films. *Proceedings of the Cambridge Philosophical Society*, 34:100–108, 1938.
- [108] E.H. Sondheimer. The mean free path of electrons in metals. *Advances in Physics*, 1:1–42, 1952.
- [109] P. Chantrenne, J.L. Barrat, X. Blase, and J.D. Gale. An analytical model for the thermal conductivity of silicon nanostructures. *Journal of Applied Physics*, 97(10):104318, 2005.
- [110] Paul C. Weakliem and Emily A. Carter. Constant temperature molecular dynamics simulations of Si(100) and Ge(100): Equilibrium structure and short-time behavior. *Journal of Chemical Physics*, 96(4):3240–3250, 1992.
- [111] Inder P. Batra. Atomic structure of the Si(001)-(2x1) surface. *Physical Review B*, 41(8):5048–5054, 1990.
- [112] R. M. Tromp, R. J. Hamers, and Demuth J. E. Si(001) dimer structure observed with scanning tunneling microscopy. *Physical Review Letters*, 55(12):1303–1306, 1985.
- [113] T. Zeng and G. Chen. Phonon heat conduction in thin films: Impacts of thermal boundary resistance and internal heat generation. *Journal of Heat Transfer*, 123(2):340–347, 2001.
- [114] Saswati Barman and G. P. Srivastava. Thermal conductivity of suspended Gaas nanostructures: Theoretical study. *Physical Review B*, 73(20):205308–205306, 2006.
- [115] Carlos J. Gomes. *Molecular Dynamics Study of Silicon Thin Films Thermal Conductivity*. Ph.D. thesis, Carnegie Mellon University, Pittsburgh, PA, 2005.
- [116] The thermal conductivity for bulk SW silicon at a temperature of 400 K is estimated by fitting a power law to the reported thermal conductivity predictions at temperatures of 300, 500, 700, and 1000 K.
- [117] Woochul Kim, Joshua Zide, Arthur Gossard, Dmitri Klenov, Susanne Stemmer, Ali Shakouri, and Arun Majumdar. Thermal conductivity reduction and thermoelectric figure of merit increase by embedding nanoparticles in crystalline semiconductors. *Physical Review Letters*, 96(4):045901–045904, 2006.
- [118] W. Kim, S. L. Singer, and A. Majumdar. Tuning thermal transport in crystalline solids using embedded nanoparticles. *Journal of Physics: Conference Series*, 92:012085, 2007.
- [119] N. Mingo, D. Hauser, N. P. Kobayashi, M. Plissonnier, and A. Shakouri. Nanoparticle-in-alloy approach to efficient thermoelectrics: Silicides in sige. *Nano Letters*, 9(2):711–715, 2009.
- [120] E. S. Landry, and A. J. H. McGaughey, Effect of film thickness on the thermal resistance of confined semiconductor thin films. To appear in *Journal of Applied Physics*.
- [121] L. Lindsay, D. A. Broido, and Natalio Mingo. Lattice thermal conductivity of single-walled carbon nanotubes: Beyond the relaxation time approximation and phonon-phonon scattering selection rules. *Physical Review B*, 80(12):125407–125407, 2009.
- [122] N. Mingo and D. A. Broido. Length dependence of carbon nanotube thermal conductivity and the “problem of long waves”. *Nano Letters*, 5(7):1221–1225, 2005.
- [123] S. Ghosh, I. Calizo, D. Teweldebrhan, E. P. Pokatilov, D. L. Nika, A. A. Balandin, W. Bao, F. Miao, and C. N. Lau. Extremely high thermal conductivity of graphene: Prospects for thermal management applications in nanoelectronic circuits. *Applied Physics Letters*, 92(15):151911–151913, 2008.



- [124] Alexander A. Balandin, Suchismita Ghosh, Wenzhong Bao, Irene Calizo, Desalegne Teweldebrhan, Feng Miao, and Chun Ning Lau. Superior thermal conductivity of single-layer graphene. *Nano Letters*, 8(3):902–907, 2008.
- [125] M. J. Biercuk, M. C. Llaguno, M. Radosavljevic, J. K. Hyun, A. T. Johnson, and J. E. Fischer. Carbon nanotube composites for thermal management. *Applied Physics Letters*, 80(15):2767–2769, 2002.
- [126] Valentin N. Popov. Carbon nanotubes: Properties and application. *Materials Science and Engineering: R: Reports*, 43(3):61–102, 2004.
- [127] A. K. Geim and K. S. Novoselov. The rise of graphene. *Nature Materials*, 6(3):183–191, 2007.
- [128] Donald W. Brenner, Olga A. Shenderova, Judith A. Harrison, Steven J. Stuart, Boris Ni, and Susan B. Sinnott. A second-generation reactive empirical bond order (Rebo) potential energy expression for hydrocarbons. *Journal of Physics: Condensed Matter*, 14(4):783–802, 2002.
- [129] Jae-Yel Yi and J. Bernholc. Atomic structure and doping of microtubules. *Physical Review B*, 47(3):1708 – 1711, 1993.
- [130] C. Casiraghi, A. Hartschuh, E. Lidorikis, H. Qian, H. Harutyunyan, T. Gokus, K. S. Novoselov, and A. C. Ferrari. Rayleigh imaging of graphene and graphene layers. *Nano Letters*, 7(9):2711–2717, 2007.
- [131] Z. H. Ni, H. M. Wang, J. Kasim, H. M. Fan, T. Yu, Y. H. Wu, Y. P. Feng, and Z. X. Shen. Graphene thickness determination using reflection and contrast spectroscopy. *Nano Letters*, 7(9):2758–2763, 2007.
- [132] Janina Zimmermann, Pasquale Pavone, and Gianaurelio Cuniberti. Vibrational modes and low-temperature thermal properties of graphene and carbon nanotubes: Minimal force-constant model. *Physical Review B*, 78(4):045410–045413, 2008.
- [133] Michael P. Marder. *Condensed Matter Physics*. John Wiley and Sons, New York, 2000.
- [134] J. A. Thomas, R. M. Iutzi, and A. J. H. McGaughey. Thermal conductivity and phonon transport in empty and water-filled carbon nanotubes. To appear in *Physical Review B*.
- [135] Private communication with J. A. Thomas of Carnegie Mellon University.
- [136] Data provided by J. A. Thomas of Carnegie Mellon University.
- [137] M. P. Allen and D. J. Tildesley. *Computer Simulation of Liquids*. Oxford University Press, Oxford, 1987.
- [138] D. C. Rapaport. *The Art of Molecular Dynamics Simulation*. Cambridge University Press, Cambridge, 1995.
- [139] A. J. H. McGaughey and M. Kaviani. Phonon transport in molecular dynamics simulations: Formulation and thermal conductivity prediction. In G. Greene, Y. Cho, J. Hartnett, and A. Bar-Cohen, editors, *Advances in Heat Transfer*, volume 39, pages 169–255. Elsevier, 2006.
- [140] Peter H. Berens, Donald H. J. Mackay, Gary M. White, and Kent R. Wilson. Thermodynamics and quantum corrections from molecular dynamics for liquid water. *The Journal of Chemical Physics*, 79(5):2375–2389, 1983.
- [141] Masanori Matsui. Molecular dynamics study of the structural and thermodynamic properties of mgo crystal with quantum correction. *The Journal of Chemical Physics*, 91(1):489–494, 1989.

- [142] V. A. Levashov, S. J. L. Billinge, and M. F. Thorpe. Quantum correction to the pair distribution function. *Journal of Computational Chemistry*, 28(11):1865–1882, 2007.
- [143] Jianwei Che, Tahir Cagin, Weiqiao Deng, and William A. Goddard III. Thermal conductivity of diamond and related materials from molecular dynamics simulations. *The Journal of Chemical Physics*, 113(16):6888–6900, 2000.
- [144] C. Z. Wang, C. T. Chan, and K. M. Ho. Tight-binding molecular-dynamics study of phonon anharmonic effects in silicon and diamond. *Physical Review B*, 42(17):11276–11283, 1990.
- [145] Young Hee Lee, R. Biswas, C. M. Soukoulis, C. Z. Wang, C. T. Chan, and K. M. Ho. Molecular-dynamics simulation of thermal conductivity in amorphous silicon. *Physical Review B*, 43(8):6573–6580, 1991.
- [146] A. Maiti, G. D. Mahan, and S. T. Pantelides. Dynamical simulations of nonequilibrium processes – heat flow and the kapitza resistance across grain boundaries. *Solid State Communications*, 102(7):517–521, 1997.
- [147] S. Volz and G. Chen. Lattice dynamic simulation of silicon thermal conductivity. *Physica B*, 263-264:709–712, 1999.
- [148] Sebastian G. Volz and Gang Chen. Molecular-dynamics simulation of thermal conductivity of silicon crystals. *Physical Review B*, 61(4):2651–2656, 2000.
- [149] Ju Li, Lisa Porter, and Sidney Yip. Atomistic modeling of finite-temperature properties of crystalline  $\beta$ -SiC: Ii. thermal conductivity and effects of point defects. *Journal of Nuclear Materials*, 255(2-3):139–152, 1998.
- [150] P. Heino. Nanoscale thermal conductivity: Size dependence by molecular dynamics. *Physica Scripta*, T114:171–174, 2004.
- [151] Javier V. Goicochea, Marcela Madrid, and Cristina Amon. Thermal properties for bulk silicon based on the determination of relaxation times using molecular dynamics. *Journal of Heat Transfer*, 132(1):012401–012411, 2010.
- [152] D. A. Broido, M. Malorny, G. Birner, Natalio Mingo, and D. A. Stewart. Intrinsic lattice thermal conductivity of semiconductors from first principles. *Applied Physics Letters*, 91(23):231922–231923, 2007.
- [153] Ju Li. *Modeling Microstructural Effects on Deformation Resistance and Thermal Conductivity*. Ph.D. thesis, Massachusetts Institute of Technology, Cambridge, MA, 2000.
- [154] Jian-Sheng Wang. Quantum thermal transport from classical molecular dynamics. *Physical Review Letters*, 99(16):160601–160604, 2007.
- [155] R. Car and M. Parrinello. Unified approach for molecular dynamics and density-functional theory. *Physical Review Letters*, 55(22):2471 – 2474, 1985.
- [156] D. M. Ceperley. Path integrals in the theory of condensed helium. *Reviews of Modern Physics*, 67(2):279–355, 1995.
- [157] Jianshu Cao and Gregory A. Voth. The formulation of quantum statistical mechanics based on the Feynman path centroid density. I. Equilibrium properties. *The Journal of Chemical Physics*, 100(7):5093–5105, 1994.
- [158] Jianshu Cao and Gregory A. Voth. The formulation of quantum statistical mechanics based on the Feynman path centroid density. II. Dynamical properties. *The Journal of Chemical Physics*, 100(7):5106–5117, 1994.

- [159] Yoshiteru Yonetani and Kenichi Kinugawa. Transport properties of liquid para-hydrogen: The path integral centroid molecular dynamics approach. *The Journal of Chemical Physics*, 119(18):9651–9660, 2003.
- [160] Duane C. Wallace. Renormalization and statistical mechanics in many-particle systems. I. Hamiltonian perturbation method. *Physical Review*, 152(1):247–260, 1966.
- [161] Private communication with D. A. Broido of Boston College.
- [162] J.-S. Wang, J. Wang, and J. T. Lu. Quantum thermal transport in nanostructures. *The European Physical Journal B*, 62(4):381–404, 2008.
- [163] Rudolf Peierls. *Surprises in Theoretical Physics*. Princeton Series in Physics. Princeton University Press, Princeton, NJ, 1979.

## APPENDICES

## APPENDIX A

### Introduction to crystals and phonons

#### A.1 Direct space and reciprocal space representations

A crystalline solid is a material whose atoms are arranged in a regular, repeating pattern. Any crystal structure can be constructed from a knowledge of its Bravais lattice and its basis. A  $D$ -dimensional Bravais lattice is a collection of points whose positions are described by

$$\mathbf{r}_{(0)}^{(l)} = \sum_{\alpha}^D l_{\alpha} \mathbf{a}_{\alpha}, \quad (\text{A.1})$$

where  $l_{\alpha}$  is an integer and  $\mathbf{a}_{\alpha}$  the  $\alpha^{\text{th}}$  lattice vector. Lattices (understood to mean Bravais lattices) are invariant under translations by the lattice vectors, meaning that the origin can be moved to any lattice point. There are fourteen Bravais lattices in three dimensions [47].

The basis, or unit cell, is the building block of a crystal structure. Associated with the basis is a volume,  $V_{uc}$ , and one or more atomic position vectors such that, when the basis is arrayed over the lattice, the entire space is tiled and the positions of all the atoms are properly defined as a combination of the lattice and basis vectors. Using  $\mathbf{r}_{(b)}^{(0)}$  to denote the equilibrium position of the  $b^{\text{th}}$  atom in the unit cell, the equilibrium position of any atom in the crystal is given by the vector

$$\mathbf{r}_{(b)}^{(l)} = \mathbf{r}_{(b)}^{(0)} + \mathbf{r}_{(0)}^{(l)}. \quad (\text{A.2})$$

Neither the basis nor the lattice are uniquely defined for a crystal. The smallest possible basis is called the primitive cell and the associated lattice is defined by primitive vectors. Another important basis called the conventional unit cell is defined as the smallest unit cell that displays the same symmetry as the full crystal.

Several common crystal lattices can be classified as cubic lattices. For these lattices the conventional unit cell is a cubic cell with a side length of  $a$ , where  $a$  is the lattice parameter (*i.e.*, the side length of the unit cell). The lattice sites are defined by the translation vector

$$\mathbf{r}_0^{(l)} = l_1 \mathbf{a}_1 + l_2 \mathbf{a}_2 + l_3 \mathbf{a}_3. \quad (\text{A.3})$$

where, in this case, the lattice vectors are:  $\mathbf{a}_1 = a\hat{i}$ ,  $\mathbf{a}_2 = a\hat{j}$ , and  $\mathbf{a}_3 = a\hat{k}$ , for the three Cartesian unit vectors  $\hat{i}$ ,  $\hat{j}$ , and  $\hat{k}$ . The most basic cubic lattice is the simple cubic (SC) lattice. For a SC lattice the conventional and primitive unit cells are the same. The two other cubic Bravais lattices are the body-centered cubic (BCC) and face-centered cubic (FCC) lattices. The argon and silicon crystals considered in this work are FCC. The FCC lattice has a conventional, SC unit cell that is four times larger than its primitive, FCC cell. The primitive FCC lattice vectors are often taken to be  $\mathbf{a}_1 = a/2(\hat{i} + \hat{j})$ ,  $\mathbf{a}_2 = a/2(\hat{j} + \hat{k})$ , and  $\mathbf{a}_3 = a/2(\hat{i} + \hat{k})$ . In this work, lattices of finite extent are described by  $N_1 \times N_2 \times N_3$  where  $N_\alpha$  is the number of conventional unit cells arrayed along the  $\alpha^{\text{th}}$  lattice vector. Lattices of infinite extent are then modeled using periodic boundary conditions.

An alternate way to represent the crystal structure is the reciprocal space representation. In the reciprocal space, the crystal lattice is described by the reciprocal lattice vectors which are defined in terms of the direct space lattice vectors. For a

3-dimensional system, the reciprocal lattice vectors are

$$\mathbf{b}_1 = 2\pi(\mathbf{a}_2 \times \mathbf{a}_3)/V_{uc} \quad (\text{A.4a})$$

$$\mathbf{b}_2 = 2\pi(\mathbf{a}_3 \times \mathbf{a}_1)/V_{uc} \quad (\text{A.4b})$$

$$\mathbf{b}_3 = 2\pi(\mathbf{a}_1 \times \mathbf{a}_2)/V_{uc}, \quad (\text{A.4c})$$

where the volume of the unit cell is given by  $V_{uc} = \mathbf{a}_1 \cdot (\mathbf{a}_2 \times \mathbf{a}_3)$ . The reciprocal lattice has the same symmetry as the direct lattice and is invariant under translation by reciprocal lattice vectors.

The advantage of the reciprocal space representation are that lattice vibrations (*i.e.*, phonons) are easier to describe using the reciprocal lattice. The vibrations are described using the phonon mode coordinates,  $q(\boldsymbol{\kappa})_\nu$ . The identifiers  $\boldsymbol{\kappa}$  and  $\nu$  are the wave vector and dispersion branch. Due to translational symmetry, the number of unique wave vectors,  $\boldsymbol{\kappa}$ , is equal to  $N$ , the number of unit cells ( $N_x N_y N_z$ , when periodic boundaries are used). By convention, the unique wave vectors are restricted to the first BZ, which is centered at  $\boldsymbol{\kappa} = \mathbf{0}$ . Wave vectors outside the first BZ can be brought into the first BZ by adding or subtracting reciprocal lattice vectors. The unique wave vectors can be determined using

$$\boldsymbol{\kappa} = \sum_{\alpha} \mathbf{b}_{\alpha} \frac{n_{\alpha}}{N_{\alpha}}, \quad (\text{A.5})$$

where  $n_{\alpha}$  is an integer such that  $N_{\alpha}/2 < n_{\alpha} \leq N_{\alpha}/2$ . Associated with each wave vector are  $3n$  phonon modes (in 3-dimensions), where  $n$  is the number of atoms in the unit cell.

## A.2 Properties of phonons

In the direct space representation, the dynamics of the atoms are described by the displacement,  $u_{\alpha}(\mathbf{r}_b)$ . The phonon mode coordinate is related to the atomic displace-

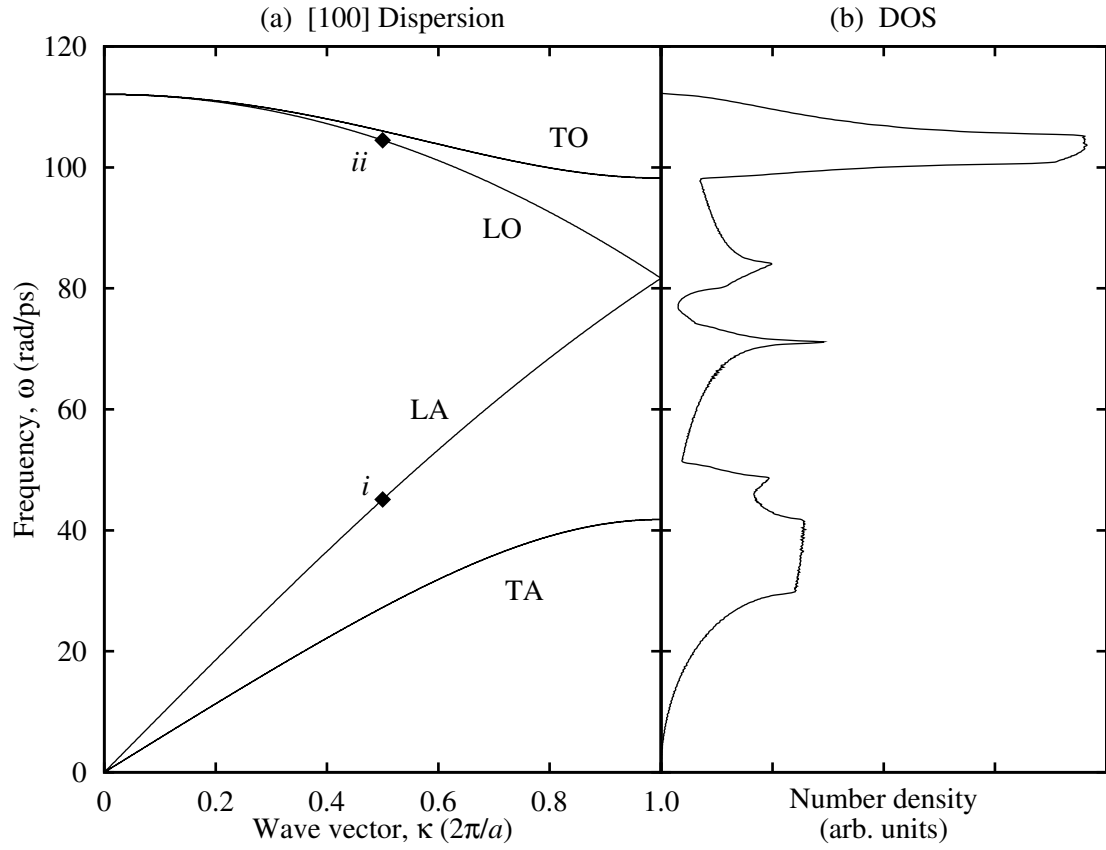


Figure A.1: Calculated (a) dispersion in the [100] direction and (b) phonon DOS for SW silicon. The longitudinal acoustic (LA), longitudinal optical (LO), transverse acoustic (TA), and transverse optical (TO) branches are labeled. The transverse branches are two-fold degenerate.



ment through a spatial Fourier transform [46],

$$q(\boldsymbol{\kappa}) = \sum_{\alpha,b,l}^{3,n,N} \sqrt{\frac{m_b}{N}} u_{\alpha}(b)^l e^*(\boldsymbol{\kappa})_{\alpha} \exp[-i\boldsymbol{\kappa} \cdot \mathbf{r}_b^l], \quad (\text{A.6})$$

where  $N$  is the total number of unit cells ( $N_x N_y N_z$ ),  $m_b$  is the mass of atom  $b$ ,  $e(\boldsymbol{\kappa})_{\alpha}^b$  is the component of the phonon mode-shape,  $\mathbf{e}(\boldsymbol{\kappa})$ , associated with atom  $b$  and direction  $\alpha$ , and  $*$  denotes the complex conjugate. The phonon mode coordinate is time-dependent and oscillates with a characteristic frequency,  $\omega(\boldsymbol{\kappa})$ .

The phonon dispersion is the relationship between the frequency and wave vector. An example of the calculated phonon dispersion for the [100] direction in silicon is shown in Fig. A.1(a). Shown in Fig. A.1(b) is the phonon density of states (DOS) which gives the number density of phonons versus frequency for all phonon modes in the full BZ. In the figure, there are six dispersion branches labeled as LA, LO, TA, and TO. The L and T stand for the type of wave, longitudinal or transverse. In a longitudinal wave, the atoms move along the wave vector, while in a transverse wave, the atoms move perpendicular to the wave vector. In Fig. A.1, the transverse branches are two-fold degenerate. A common misconception is that all phonons can be categorized as either longitudinal or transverse. While generally true along high symmetry directions (*e.g.*, [100], [110], [111], etc.), phonons at an arbitrary wave vector are often neither purely longitudinal nor purely transverse but a mixture of both.

The A is for acoustic. At each value of the wave vector, there are always three acoustic branches present in a 3-dimensional crystal. The acoustic frequencies go to zero at  $\boldsymbol{\kappa} = \mathbf{0}$  (the  $\Gamma$ -point). These acoustic frequencies near the  $\Gamma$ -point are related to the propagation of sound through a crystal. The O or optical branches are those which do not have zero frequency at the  $\Gamma$ -point. At the  $\Gamma$ -point the slope of the optical

branches must be zero. The name optical arises from the fact that these branches can interact with photons, though not necessarily at the frequencies of visible light. For a crystal with  $n$  atoms in the unit cell, there will be  $3n - 3$  optical branches, one for each degree of freedom minus the three acoustic branches.

This nomenclature for identifying dispersion branches is widely used. One should not place too much significance on the differences implied by the different names, however, since the naming convention breaks down under close inspection. In an isotropic crystal, the phonons are all purely longitudinal or purely transverse. Likewise, along high symmetry directions (*e.g.*,  $[100]$ ,  $[110]$ ,  $[111]$ , etc.) in anisotropic crystals, the phonons are typically either longitudinal or transverse. However, the phonons at an arbitrary wave vector in an anisotropic crystal can be a mixture of both wave types [28]. Additionally, portions of acoustic branches can be transformed to optical branches by a process of zone-folding by simply increasing the size of the unit cell.

As has been stated, the unit cell and direct lattice vectors are not unique for a crystal. Since the reciprocal space representation is dependent upon the unit cell and direct lattice vectors, altering the choice of the direct space representation also impacts the reciprocal space. This impact is illustrated in Fig. A.2, where the dispersion curves in the  $[100]$  direction are plotted for an argon crystal using a one atom, primitive unit cell with FCC lattice vectors and the four atom, conventional unit cell with SC lattice vectors. The boundary of the first BZ occurs at  $\kappa = \pm 2\pi/a$  for the primitive unit cell and  $\kappa = \pm \pi/a$  for the conventional unit cell. The dispersion curves for the primitive unit cell are translated to the negative half of the first BZ through a reciprocal lattice vector of the conventional unit cell. Through symmetry about  $\kappa = 0$  [ $\omega(\kappa) = \omega(\kappa)$ ,  $e(\kappa \ b) = e^*(\kappa \ b)$ , etc.], the dispersion curves for the primitive lattice are,

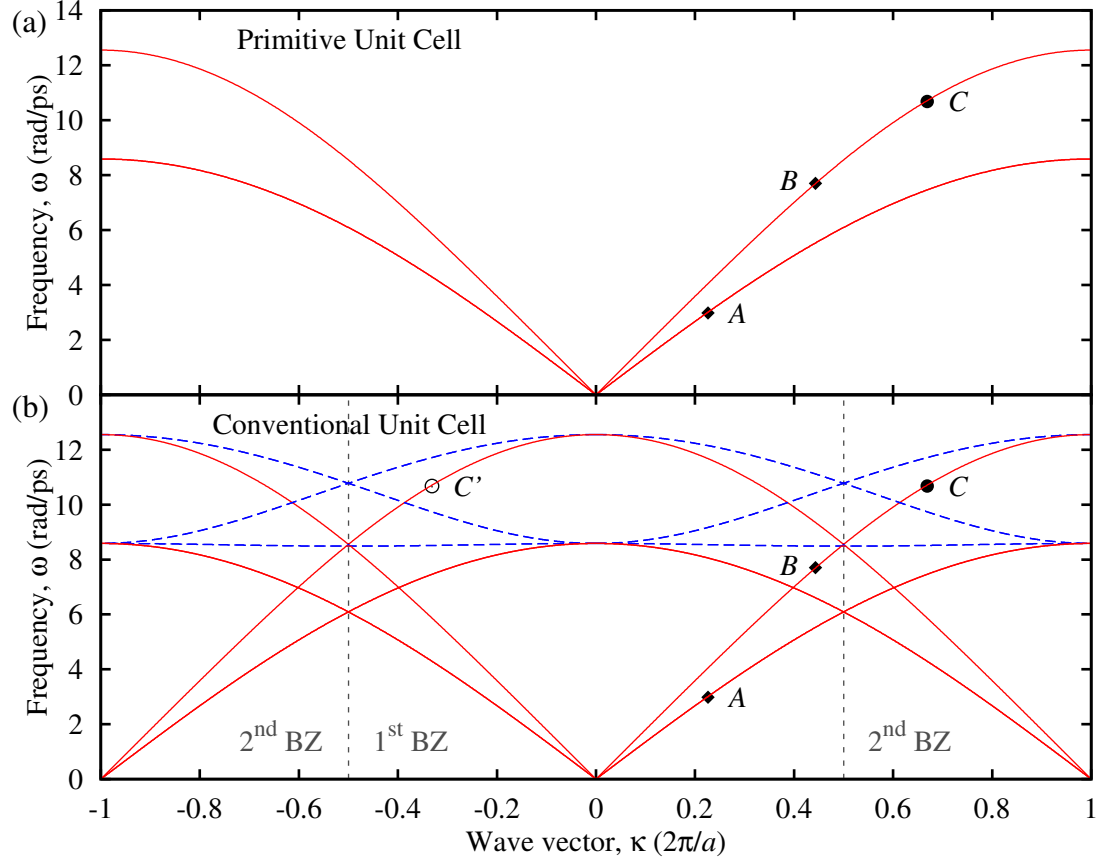


Figure A.2: Dispersion curves in the  $[100]$  direction for argon using (a) the primitive unit cell and (b) the conventional unit cell. With the primitive (conventional) unit cell, the first BZ is defined by  $-2\pi/a < \kappa \leq 2\pi/a$  ( $-\pi/a < \kappa \leq \pi/a$ ). For the conventional unit cell, the left ( $-2\pi/a < \kappa \leq -\pi/a$ ) and right ( $\pi/a < \kappa \leq 2\pi/a$ ) portions of the second BZ can be brought into the first BZ through translation by the reciprocal lattice vector,  $2\pi/a$ . The phonon modes labeled  $A$  and  $B$  are able to combine to produce phonon mode  $C$ . This 3-phonon interaction is a N-process in the primitive unit cell but an U-process in the conventional unit cell. In the U-process, phonon mode  $C$  is brought back into the first BZ to the equivalent mode  $C'$  through a translation by a reciprocal lattice.

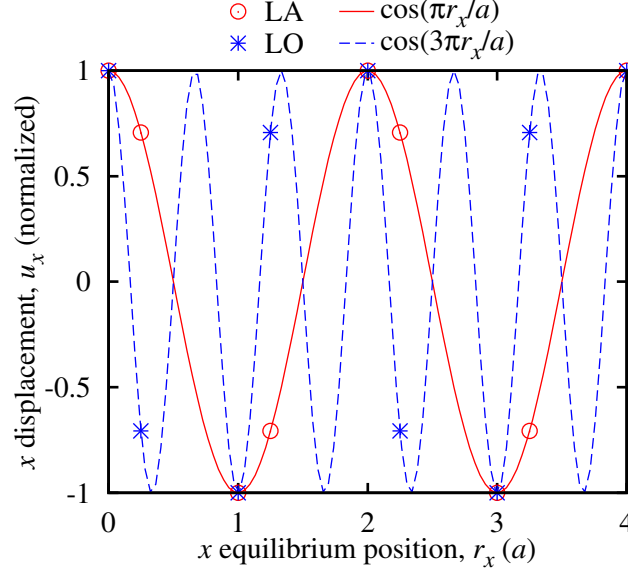


Figure A.3: Normalized displacements of the atoms along the  $[100]$  ( $x$ ) direction due to the LA and LO phonon modes at  $\kappa = \pi/a$  in silicon as defined through the real part of  $e\left(\begin{smallmatrix} \kappa & b \\ \nu & \alpha \end{smallmatrix}\right) \exp\left[i\boldsymbol{\kappa} \cdot \mathbf{r}_b^{(l)}\right]$ . The shortest wavelengths that describe the displacements due to these LA and LO modes are  $2a$  and  $2a/3$ .

in effect, folded back into the first BZ of the conventional unit cell. This effect is called zone-folding. The additional dispersion curves seen for the conventional unit cell (dotted lines) correspond to dispersion curves along other directions in the first BZ of the primitive unit cell, which, because of the change in shape of the first BZ, are mapped into the  $[100]$  direction of the conventional unit cell.

Zone-folding illustrates an important fact about phonons. For phonons the wave vector may not be related to the wavelength,  $\lambda$ , through  $\lambda = 2\pi/|\boldsymbol{\kappa}|$  as it is for subatomic particles such as electrons, neutrons, and photons. A phonon subjected to zone-folding, or to translation through a reciprocal lattice vector, does not undergo a change of its wavelength even though its wave vector does change. The wavelength of the phonon is determined through the periodicity of the quantity  $e\left(\begin{smallmatrix} \kappa & b \\ \nu & \alpha \end{smallmatrix}\right) \exp[i\boldsymbol{\kappa} \cdot \mathbf{r}_b^{(l)}]$ , which is just the normalized atomic displacements. Thus, both the mode shape and the wave vector are needed to determine the wavelength. This point is illustrated in

Fig. A.3, in which is plotted the atomic displacement due to the phonons at  $\kappa = \pi/a$  from the LA and LO silicon dispersion branches (labeled as *i* and *ii*) in Fig. A.1. The LA phonon mode as a wavelength of  $2a$  while the LO mode has a wavelength of  $2a/3$ .

The wave vector is a common source of misunderstanding concerning phonons and not just for its unusually complicated relation to the wavelength. The quantity  $\hbar\kappa$  has the same units as momentum and is suggestively called quasi-momentum, which is unfortunate because phonons do not carry momentum [51, 163]. Wave vectors are arbitrary up to a reciprocal lattice vector, and, as demonstrated in Fig. A.2, are dependent upon the choice of the unit cell and direct lattice vectors. Confusing matters is the constraint on the wave vector when phonons interact with other phonons and when phonons interact with subatomic particles. In phonon-phonon interactions, this constraint is commonly referred to as conservation of quasi-momentum. Yet, it stems from the translational symmetry of the lattice rather than the conservation law for real momentum. In subatomic particles, such as neutrons, electrons, and photons, the momentum is given by  $\hbar\kappa$ . However, the conservation of the wave vector, required for these particles to interact with phonons, arises from the periodic nature of the lattice rather than an accounting for momentum [133]. The momentum balance manifests as a change in the center of mass velocity of the crystal (if it is not fixed). Thus, the constraints for a subatomic particle to interact with a phonon are

$$\kappa_S = \kappa_{S'} \pm \kappa, \quad (\text{A.7a})$$

$$\hbar\kappa_S + m_C \mathbf{v}_C = \hbar\kappa_{S'} + m_C \mathbf{v}_{C'}, \quad (\text{A.7b})$$

$$\frac{\hbar^2 |\kappa_S|^2}{2m_S} + \frac{m_C}{2} |\mathbf{v}_C|^2 = \frac{\hbar^2 |\kappa_{S'}|^2}{2m_S} + \frac{m_C}{2} |\mathbf{v}_{C'}|^2 \pm \hbar\omega, \quad (\text{A.7c})$$

where the subscripts  $S$  and  $C$  ( $S'$ ,  $C'$ ) indicate the subatomic and crystal properties prior to (after) the interaction and the addition (subtraction) before the phonon prop-

erties indicates the phonon has been created (destroyed). Equation (A.7a) satisfies the Bragg condition and arises from the periodic nature of the lattice [133]. Equations (A.7b) and (A.7c) enforce the conservation of momentum and energy. In interactions between subatomic particles and phonons, the kinetic energy change of the crystal is small (due to its large mass) and can be neglected. Neglect of the crystal kinetic energy removes an unknown, allowing the momentum conservation law to be ignored as well. Hence, Eq. (A.7a) has the appearance of taking the place of a real momentum conservation law.

### A.3 The role of normal-processes in thermal resistance

For phonon-phonon scattering, usually only interactions involving three phonons are considered. Four- and higher-order phonon interactions are typically considered to be too rare to contribute significantly to the thermal resistance. Three phonons can interact in two ways. Two phonons can combine to form a third or a single phonon can decay into two phonons. The other two possibilities where three phonons spontaneously appear or disappear cannot occur in a crystal since they would violate conservation of energy. In addition to energy, phonon interactions must conserve quasi-momentum (crystal momentum) up to a reciprocal lattice vector. The conditions that need to be satisfied for a phonon-phonon interaction to occur can be written as

$$\hbar\omega_{(\nu)} = \hbar\omega_{(\nu')} + \hbar\omega_{(\nu'')} \quad \hbar\mathbf{k} = \hbar\mathbf{k}' + \hbar\mathbf{k}'' + j\hbar\mathbf{K} \quad \textit{Type I} \quad (\text{A.8a})$$

$$\hbar\omega_{(\nu)} + \hbar\omega_{(\nu')} = \hbar\omega_{(\nu'')} \quad \hbar\mathbf{k} + \hbar\mathbf{k}' = \hbar\mathbf{k}'' + j\hbar\mathbf{K} \quad \textit{Type II}, \quad (\text{A.8b})$$

where  $\mathbf{K}$  is any reciprocal lattice vector and  $j$  is an integer. Interactions where  $j$  is zero are called Normal-processes while for Umklapp-processes  $j$  is nonzero. The distinction is made between the two processes because it is widely accepted that N-processes by

themselves cannot contribute to thermal resistance [27, 46]. This thinking, however, is incorrect. Normal-processes do contribute directly to thermal resistance and are indistinguishable from U-processes.

The notion that N-processes do not contribute to thermal resistance originated with a statement by Rudolf Peierls. In his book on the *Quantum theory of solids* [28], Peierls states about N-processes:

Hence the collisions would be incapable of establishing complete statistical equilibrium if once  $\mathbf{J} \neq \mathbf{0}$  [ $\mathbf{J} = \sum_{\kappa, \nu} f(\nu) \kappa$ ]... Now a resultant  $\mathbf{J}$  in the positive  $x$ -direction means that the phonons in the positive  $x$ -direction will be more numerous than those traveling in the opposite direction, and this asymmetry will lead to a non-vanishing energy transport. In other words, in this hypothetical case a finite energy transport can persist without a temperature gradient to maintain it, and this implies an infinite thermal conductivity.

Instead of being an assertion on the unimportance of N-processes in thermal resistance, this statement is an argument on the necessity of including U-processes. Peierls also writes:

physically there is no important difference between processes in which the sum  $\kappa + \kappa'$  just remains within the basic cell, and those in which it falls just outside and has to be brought back by adding a suitable  $\mathbf{K}$ , and indeed the distinction between the two depends on our convention in choosing the basic cell. What matters, however, is whether or not we can find a convention with which  $[\mathbf{f} + \mathbf{f}' - \mathbf{f}'' = \mathbf{K}]$  would always hold with  $\mathbf{K} = \mathbf{0}$ .

So what Peierls is actually arguing is not that N-processes do not contribute to thermal resistance but that U-processes also contribute to thermal resistance. Though only the phonons in the first BZ are unique, 3-phonon processes that include two phonons from the first BZ and one from the second Brillouin zone need to be explicitly considered. Umklapp-processes are not a double counting of N-processes. All 3-phonon interactions that involve more than one phonon outside of the first BZ, however, can be expressed as a process with at least two of the phonons within the first BZ.

Rather than N and U-processes being two different types of three-phonon scattering processes, they obey the same physics and are, in fact, indistinguishable. To demonstrate that N and U-processes are not distinguishable, consider the argon dispersion curves in the  $[100]$  direction given in Fig. A.2. The phonon modes labeled  $A$  and  $B$  are able to combine to produce phonon mode  $C$ . This 3-phonon interaction is a N-process in the primitive unit cell but an U-process in the conventional unit cell. In the U-process, phonon mode  $C$  is brought back into the first BZ to the equivalent mode  $C'$  through a translation by a reciprocal lattice. This dependence of N and U-processes on the basis is noted by Peierls in the second quote above.

Regardless of Peierls' original intent, his statement is flawed. The error comes from treating the sum of the quasi-momentum as an indication of equilibrium. Because phonons do not carry momentum [51, 163], the quantity  $\mathbf{J} = \sum_{\mathbf{\kappa}, \nu} f(\nu) \mathbf{\kappa}$  is arbitrary and has no meaning. It is only by convention that only phonons in the first BZ are considered and the sum over quasi-momentum is zero for a system in equilibrium (it is actually non-zero if phonons on only the positive edge of the first BZ are considered). This convention is chosen for mathematical convenience but is otherwise arbitrary. One can add a constant wave vector,  $\delta\mathbf{\kappa}$ , to each wave vector in the conventional first



BZ with the result that the center of the first BZ is no longer at zero. This new first BZ is equivalent to the conventional first BZ but now  $\mathbf{J} \neq \mathbf{0}$ . Thus, the value of the quasi-momentum sum can be changed without changing the state of the crystal. Additionally, if the conventional first BZ is used, the normal mode coordinates can always be chosen such that  $\mathbf{J} = \mathbf{0}$  (again neglecting the edge of the first BZ). This result arises from the fact that  $q(\boldsymbol{\kappa}) = q^*(\boldsymbol{\kappa})$  and is shown in Appendix B.

Rather than consider the sum of the quasi-momentum, one should consider the total energy flux in a crystal:

$$\boldsymbol{\xi} = \frac{1}{V} \sum_{\boldsymbol{\kappa}, \nu} f(\boldsymbol{\kappa}) \hbar \omega(\boldsymbol{\kappa}) \mathbf{v}_g(\boldsymbol{\kappa}). \quad (\text{A.9})$$

Now the question to ask is: *can N-processes alone change the energy flux?* The answer to this question is yes. The total energy,  $\frac{1}{V} \sum_{\boldsymbol{\kappa}, \nu} f(\boldsymbol{\kappa}) \hbar \omega(\boldsymbol{\kappa})$ , is constant due to energy conservation, however, the total energy flux,  $\boldsymbol{\xi}$ , is guaranteed not to change through N-processes only if the constraints

$$\mathbf{v}_g(\boldsymbol{\kappa}) = \mathbf{v}_g(\boldsymbol{\kappa}') + \mathbf{v}_g(\boldsymbol{\kappa}'') \quad \text{Type I} \quad (\text{A.10a})$$

$$\mathbf{v}_g(\boldsymbol{\kappa}) + \mathbf{v}_g(\boldsymbol{\kappa}') = \mathbf{v}_g(\boldsymbol{\kappa}'') \quad \text{Type II}, \quad (\text{A.10b})$$

are added in addition to Eqs. (A.8) for type I and type II interactions. The only way to satisfy all three constraints for each of these 3-phonon processes is to require the group velocities to be constant (*i.e.*, the Debye approximation applies) and equal for each dispersion branch. This condition is impossible to satisfy for a real crystal since the group velocities would be undefined (from a discontinuous dispersion relation) at the zone boundaries. Thus, N-processes alone can change the energy flux and lead to thermal resistance in crystals.

## APPENDIX B

### Derivation of the lattice dynamics techniques

#### B.1 Harmonic lattice dynamics

The anharmonic corrections to the harmonic phonon frequencies are derived using quantum mechanics and perturbation theory. Here, the treatment outlined by Wallace [61, 160] is followed. The derivation starts in the normal way for determining the harmonic frequencies of vibration. Consider a three dimensional crystal lattice of  $N$  unit cells each containing  $n$  atoms. Let  $l$  index over unit cells and  $b$  index over atoms within the unit cells. The equilibrium position of an atom shall be denoted by  $r_\alpha^{(l)}$ , where  $\alpha$  gives the Cartesian component of the position vector. Given a general expression for the potential energy in the crystal,  $\Phi$ , one expands it in a Taylor series

about the atomic displacements as

$$\begin{aligned}
\Phi = & \Phi|_o + \sum_{\alpha_1, b_1, l_1}^{3, n, N} \left. \frac{\partial \Phi}{\partial r_{\alpha_1}(l_1)} \right|_o u_{\alpha_1}(l_1) \\
& + \frac{1}{2!} \sum_{\alpha_1, b_1, l_1}^{3, n, N} \sum_{\alpha_2, b_2, l_2}^{3, n, N} \left. \frac{\partial^2 \Phi}{\partial r_{\alpha_1}(l_1) \partial r_{\alpha_2}(l_2)} \right|_o u_{\alpha_1}(l_1) u_{\alpha_2}(l_2) \\
& + \frac{1}{3!} \sum_{\alpha_1, b_1, l_1}^{3, n, N} \sum_{\alpha_2, b_2, l_2}^{3, n, N} \sum_{\alpha_3, b_3, l_3}^{3, n, N} \left. \frac{\partial^3 \Phi}{\partial r_{\alpha_1}(l_1) \partial r_{\alpha_2}(l_2) \partial r_{\alpha_3}(l_3)} \right|_o u_{\alpha_1}(l_1) u_{\alpha_2}(l_2) u_{\alpha_3}(l_3) \\
& + \frac{1}{4!} \sum_{\alpha_1, b_1, l_1}^{3, n, N} \sum_{\alpha_2, b_2, l_2}^{3, n, N} \sum_{\alpha_3, b_3, l_3}^{3, n, N} \sum_{\alpha_4, b_4, l_4}^{3, n, N} \left. \frac{\partial^4 \Phi}{\partial r_{\alpha_1}(l_1) \partial r_{\alpha_2}(l_2) \partial r_{\alpha_3}(l_3) \partial r_{\alpha_4}(l_4)} \right|_o \\
& \times u_{\alpha_1}(l_1) u_{\alpha_2}(l_2) u_{\alpha_3}(l_3) u_{\alpha_4}(l_4) + O(u^5),
\end{aligned} \tag{B.1}$$

where  $u_\alpha$  is the  $\alpha$ -component of displacement from equilibrium and is small in comparison to the spacing between atoms. The derivatives are all evaluated for atoms at their equilibrium positions. The first two terms on the right hand side can be immediately neglected since  $\Phi|_o$  is merely a constant shift in the energy and the negative of the first derivative gives the component of the force on the atom, which is zero at equilibrium. The terms of order  $u^5$  and higher are also neglected as small in comparison to leading order terms.

Next, the system Hamiltonian is expressed in terms of Eq. (B.1). The Hamiltonian is

$$H = H_2 + H_3 + H_4, \tag{B.2}$$

where

$$H_2 = \frac{1}{2} \sum_{b, l}^{n, N} m_b \dot{u}_\alpha(l)^2 + \frac{1}{2!} \sum_{\alpha_1, b_1, l_1}^{3, n, N} \sum_{\alpha_2, b_2, l_2}^{3, n, N} \Phi_{\alpha_1 \alpha_2} \left( \begin{smallmatrix} l_1 & l_2 \\ b_1 & b_2 \end{smallmatrix} \right) \tag{B.3a}$$

$$H_3 = \frac{1}{3!} \sum_{\alpha_1, b_1, l_1}^{3, n, N} \sum_{\alpha_2, b_2, l_2}^{3, n, N} \sum_{\alpha_3, b_3, l_3}^{3, n, N} \Phi_{\alpha_1 \alpha_2 \alpha_3} \left( \begin{smallmatrix} l_1 & l_2 & l_3 \\ b_1 & b_2 & b_3 \end{smallmatrix} \right) \tag{B.3b}$$

$$H_4 = \frac{1}{4!} \sum_{\alpha_1, b_1, l_1}^{3, n, N} \sum_{\alpha_2, b_2, l_2}^{3, n, N} \sum_{\alpha_3, b_3, l_3}^{3, n, N} \sum_{\alpha_4, b_4, l_4}^{3, n, N} \Phi_{\alpha_1 \alpha_2 \alpha_3 \alpha_4} \left( \begin{smallmatrix} l_1 & l_2 & l_3 & l_4 \\ b_1 & b_2 & b_3 & b_4 \end{smallmatrix} \right), \tag{B.3c}$$

and

$$\Phi_{\alpha_1 \alpha_2 \dots \alpha_i} \left( \begin{smallmatrix} l_1 & l_2 & \dots & l_i \\ b_1 & b_2 & \dots & b_i \end{smallmatrix} \right) = \frac{\partial^i \Phi}{\partial r_{\alpha_1} \left( \begin{smallmatrix} l_1 \\ b_1 \end{smallmatrix} \right) \partial r_{\alpha_2} \left( \begin{smallmatrix} l_2 \\ b_2 \end{smallmatrix} \right) \dots \partial r_{\alpha_i} \left( \begin{smallmatrix} l_i \\ b_i \end{smallmatrix} \right)} \Big|_o u_{\alpha_1} \left( \begin{smallmatrix} l_1 \\ b_1 \end{smallmatrix} \right) u_{\alpha_2} \left( \begin{smallmatrix} l_2 \\ b_2 \end{smallmatrix} \right) \dots u_{\alpha_i} \left( \begin{smallmatrix} l_i \\ b_i \end{smallmatrix} \right). \quad (\text{B.4})$$

The dot over displacement denotes the time derivative while  $m_b$  is the mass of the  $b^{th}$  atom in the unit cell. First, consider the term  $H_2$ . Using a Fourier transform, a coordinate change is performed by letting

$$u_{\alpha} \left( \begin{smallmatrix} l \\ b \end{smallmatrix} \right) = [Nm_b]^{-1/2} \sum_{\boldsymbol{\kappa}} \sum_{\nu=1}^{3n} q(\boldsymbol{\kappa}_{\nu}) e(\boldsymbol{\kappa}_{\nu} \begin{smallmatrix} b \\ \alpha \end{smallmatrix}) \exp[i\boldsymbol{\kappa} \cdot \mathbf{r} \left( \begin{smallmatrix} l \\ b \end{smallmatrix} \right)] \quad (\text{B.5a})$$

$$\dot{u}_{\alpha} \left( \begin{smallmatrix} l \\ b \end{smallmatrix} \right) = [Nm_b]^{-1/2} \sum_{\boldsymbol{\kappa}} \sum_{\nu=1}^{3n} \dot{q}(\boldsymbol{\kappa}_{\nu}) e(\boldsymbol{\kappa}_{\nu} \begin{smallmatrix} b \\ \alpha \end{smallmatrix}) \exp[i\boldsymbol{\kappa} \cdot \mathbf{r} \left( \begin{smallmatrix} l \\ b \end{smallmatrix} \right)], \quad (\text{B.5b})$$

where  $q$  is the transformed coordinate and  $e$  is some coefficient to be determined.

The variables  $q$  and  $e$  are functions of  $\boldsymbol{\kappa}$  and  $\nu$ . The wave vector,  $\boldsymbol{\kappa}$ , has a magnitude that is equal to  $2\pi$  divided by the vibration wavelength. The periodic nature of the equations, namely the  $\exp[i\boldsymbol{\kappa} \cdot \mathbf{r} \left( \begin{smallmatrix} l \\ b \end{smallmatrix} \right)]$  terms, allows one to limit the wave vector to  $N$  non-degenerate, discrete points within the first Brillouin zone. The purpose of  $\nu$  is to enumerate the number of degrees of freedom available at each wave vector.

Substituting Eqs. (B.5a) and (B.5b) into Eq. (B.3a) yields

$$\begin{aligned} H_2 &= \frac{1}{2N} \sum_{\alpha, b, l}^{3, n, N} \left| \sum_{\boldsymbol{\kappa}, \nu}^{N, 3n} \dot{q}(\boldsymbol{\kappa}_{\nu}) e(\boldsymbol{\kappa}_{\nu} \begin{smallmatrix} b \\ \alpha \end{smallmatrix}) \exp[i\boldsymbol{\kappa} \cdot \mathbf{r} \left( \begin{smallmatrix} l \\ b \end{smallmatrix} \right)] \right|^2 + \frac{1}{2!N} \sum_{\alpha_1, b_1, l_1}^{3, n, N} \sum_{\alpha_2, b_2, l_2}^{3, n, N} \frac{\partial^2 \Phi}{\partial r_{\alpha_1} \left( \begin{smallmatrix} l_1 \\ b_1 \end{smallmatrix} \right) \partial r_{\alpha_2} \left( \begin{smallmatrix} l_2 \\ b_2 \end{smallmatrix} \right)} \Big|_o \\ &\quad \times \frac{1}{\sqrt{m_{b_1} m_{b_2}}} \sum_{\boldsymbol{\kappa}_1, \nu_1}^{N, 3n} q(\boldsymbol{\kappa}_{\nu_1}) e(\boldsymbol{\kappa}_{\nu_1} \begin{smallmatrix} b_1 \\ \alpha_1 \end{smallmatrix}) \exp[i\boldsymbol{\kappa}_1 \cdot \mathbf{r} \left( \begin{smallmatrix} l_1 \\ b_1 \end{smallmatrix} \right)] \sum_{\boldsymbol{\kappa}_2, \nu_2}^{N, 3n} q(\boldsymbol{\kappa}_{\nu_2}) e(\boldsymbol{\kappa}_{\nu_2} \begin{smallmatrix} b_2 \\ \alpha_2 \end{smallmatrix}) \exp[i\boldsymbol{\kappa}_2 \cdot \mathbf{r} \left( \begin{smallmatrix} l_2 \\ b_2 \end{smallmatrix} \right)] \\ &= \frac{1}{2N} \sum_{\boldsymbol{\kappa}_1, \nu_1}^{N, 3n} \sum_{\boldsymbol{\kappa}_2, \nu_2}^{N, 3n} \sum_{\alpha, b, l}^{3, n, N} \exp[i(\boldsymbol{\kappa}_1 + \boldsymbol{\kappa}_2) \cdot \mathbf{r} \left( \begin{smallmatrix} l \\ b \end{smallmatrix} \right)] \exp[i(\boldsymbol{\kappa}_1 + \boldsymbol{\kappa}_2) \cdot \mathbf{r} \left( \begin{smallmatrix} 0 \\ b \end{smallmatrix} \right)] \dot{q}(\boldsymbol{\kappa}_{\nu_1}) e(\boldsymbol{\kappa}_{\nu_1} \begin{smallmatrix} b \\ \alpha \end{smallmatrix}) \dot{q}(\boldsymbol{\kappa}_{\nu_2}) e(\boldsymbol{\kappa}_{\nu_2} \begin{smallmatrix} b \\ \alpha \end{smallmatrix}) \\ &\quad + \frac{1}{2!N} \sum_{\boldsymbol{\kappa}_1, \nu_1}^{N, 3n} \sum_{\boldsymbol{\kappa}_2, \nu_2}^{N, 3n} q(\boldsymbol{\kappa}_{\nu_1}) q(\boldsymbol{\kappa}_{\nu_2}) \sum_{\alpha_1, b_1, l_1}^{3, n, N} \sum_{\alpha_2, b_2, l_2}^{3, n, N} e(\boldsymbol{\kappa}_{\nu_1} \begin{smallmatrix} b_1 \\ \alpha_1 \end{smallmatrix}) e(\boldsymbol{\kappa}_{\nu_2} \begin{smallmatrix} b_2 \\ \alpha_2 \end{smallmatrix}) \exp[i(\boldsymbol{\kappa}_1 + \boldsymbol{\kappa}_2) \cdot \mathbf{r} \left( \begin{smallmatrix} l_1 \\ b_1 \end{smallmatrix} \right)] \\ &\quad \times \frac{1}{\sqrt{m_{b_1} m_{b_2}}} \frac{\partial^2 \Phi}{\partial r_{\alpha_1} \left( \begin{smallmatrix} l_1 \\ b_1 \end{smallmatrix} \right) \partial r_{\alpha_2} \left( \begin{smallmatrix} l_2 \\ b_2 \end{smallmatrix} \right)} \Big|_o \exp[i(\boldsymbol{\kappa}_1 + \boldsymbol{\kappa}_2) \cdot \mathbf{r} \left( \begin{smallmatrix} 0 \\ b_1 \end{smallmatrix} \right)] \exp[i\boldsymbol{\kappa}_2 \cdot (\mathbf{r} \left( \begin{smallmatrix} l_2 \\ b_2 \end{smallmatrix} \right) - \mathbf{r} \left( \begin{smallmatrix} l_1 \\ b_1 \end{smallmatrix} \right))]. \end{aligned} \quad (\text{B.6})$$

Both the kinetic and potential energies contain terms like  $\sum_{l_1}^N \exp[i(\boldsymbol{\kappa}_1 + \boldsymbol{\kappa}_2) \cdot \mathbf{r}_0^{(l_1)}]$  which, due to the periodicity in the lattice, is equal to  $N\delta_{\mathbf{K}}(\boldsymbol{\kappa}_1 + \boldsymbol{\kappa}_2)$ . The function  $\delta_{\mathbf{K}}(\boldsymbol{\kappa})$  is similar to the delta function. It is taken to be zero unless the argument is a multiple of a reciprocal lattice vector,  $\mathbf{K}$ , in which case it is one. The wave vectors are restricted to the first Brillouin zone ( $-\mathbf{K} < 2\boldsymbol{\kappa} \leq \mathbf{K}$ ) so  $-\mathbf{K} < \boldsymbol{\kappa}_1 + \boldsymbol{\kappa}_2 \leq \mathbf{K}$ . Note that  $\delta_{\mathbf{K}}(\boldsymbol{\kappa}_1 + \boldsymbol{\kappa}_2)$  is non-zero only for  $\boldsymbol{\kappa}_1 = -\boldsymbol{\kappa}_2$  or  $\boldsymbol{\kappa}_1 = \boldsymbol{\kappa}_2 = \mathbf{K}/2$ . The second condition is equivalent to the first if  $\boldsymbol{\kappa}_1 = \mathbf{K}/2$  and  $\boldsymbol{\kappa}_2 = -\mathbf{K}/2$  and  $\boldsymbol{\kappa}_2$  is shifted by  $\mathbf{K}$  to get  $\boldsymbol{\kappa}_1 = \boldsymbol{\kappa}_2 = \mathbf{K}/2$ . Therefore,  $\boldsymbol{\kappa}_1 = -\boldsymbol{\kappa}_2$ , which can immediately be used in the kinetic energy. The sum appears to be coupled to additional terms in the potential energy, though. The sum can be decoupled from these additional terms by again using lattice periodicity as well as translational invariance.

The last part of Eq. (B.6) can be rewritten as

$$\begin{aligned} & \sum_{l_1}^N \exp[i(\boldsymbol{\kappa}_1 + \boldsymbol{\kappa}_2) \cdot \mathbf{r}_0^{(l_1)}] \sum_{\alpha_1, b_1}^{3,n} \sum_{\alpha_2, b_2, l}^{3,n, N} \frac{1}{\sqrt{m_{b_1} m_{b_2}}} \frac{\partial^2 \Phi}{\partial r_{\alpha_1}^{(0)}(b_1) \partial r_{\alpha_2}^{(l)}(b_2)} \Big|_o \\ & \times \exp[i(\boldsymbol{\kappa}_1 + \boldsymbol{\kappa}_2) \cdot \mathbf{r}_{b_1}^{(0)}] \exp[i\boldsymbol{\kappa}_2 \cdot (\mathbf{r}_{b_2}^{(l)} - \mathbf{r}_{b_1}^{(0)})], \end{aligned} \quad (\text{B.7})$$

where  $l = l_2 - l_1$ . One can now see that the summation over  $l_1$  is independent of all other summations. This fact is used to rewrite Eq. (B.6) as

$$\begin{aligned} H_2 = & \frac{1}{2} \sum_{\alpha_1, b_1}^{3,n} \sum_{\nu_1}^{3n} \sum_{\boldsymbol{\kappa}_2, \nu_2}^{N, 3n} \left| \dot{q}_{(\nu_1)}^{(\boldsymbol{\kappa}_2)} e\left(\begin{smallmatrix} \boldsymbol{\kappa}_2 & b_1 \\ \nu_1 & \alpha_1 \end{smallmatrix}\right) \right\| \dot{q}_{(\nu_2)}^{(\boldsymbol{\kappa}_2)} e\left(\begin{smallmatrix} \boldsymbol{\kappa}_2 & b_2 \\ \nu_2 & \alpha_2 \end{smallmatrix}\right) \Big| \\ & + \frac{1}{2} \sum_{\nu_1}^{3n} \sum_{\boldsymbol{\kappa}_2, \nu_2}^{N, 3n} q_{(\nu_1)}^{(\boldsymbol{\kappa}_2)} q_{(\nu_2)}^{(\boldsymbol{\kappa}_2)} \sum_{\alpha_1, b_1}^{3,n} \sum_{\alpha_2, b_2}^{3,n} D_{\boldsymbol{\kappa}_2} \left(\begin{smallmatrix} b_1 & b_2 \\ \alpha_1 & \alpha_2 \end{smallmatrix}\right) e\left(\begin{smallmatrix} \boldsymbol{\kappa}_2 & b_1 \\ \nu_1 & \alpha_1 \end{smallmatrix}\right) e\left(\begin{smallmatrix} \boldsymbol{\kappa}_2 & b_2 \\ \nu_2 & \alpha_2 \end{smallmatrix}\right), \end{aligned} \quad (\text{B.8})$$

where

$$D_{\boldsymbol{\kappa}} \left(\begin{smallmatrix} b_1 & b_2 \\ \alpha_1 & \alpha_2 \end{smallmatrix}\right) = \sum_l^N \frac{1}{\sqrt{m_{b_1} m_{b_2}}} \frac{\partial^2 \Phi}{\partial r_{\alpha_1}^{(0)}(b_1) \partial r_{\alpha_2}^{(l)}(b_2)} \Big|_o \exp[i\boldsymbol{\kappa} \cdot (\mathbf{r}_{b_2}^{(l)} - \mathbf{r}_{b_1}^{(0)})]. \quad (\text{B.9})$$

This last equation defines the dynamical matrix. It is the only place where the complexities of atomic interactions come into play in the harmonic Hamiltonian.

In the next step, the last line of Eq. (B.8) is treated separately by introducing the variable  $\omega^2(\boldsymbol{\kappa}_\nu)$ . Let

$$\omega^2(\boldsymbol{\kappa}_\nu) e\left(-\boldsymbol{\kappa}_\nu \begin{smallmatrix} b_1 \\ \alpha_1 \end{smallmatrix}\right) e\left(\boldsymbol{\kappa}_\nu \begin{smallmatrix} b_1 \\ \alpha_1 \end{smallmatrix}\right) = \sum_{\alpha_2, b_2}^{3,n} D_{\boldsymbol{\kappa}}\left(\begin{smallmatrix} b_1 & b_2 \\ \alpha_1 & \alpha_2 \end{smallmatrix}\right) e\left(-\boldsymbol{\kappa}_\nu \begin{smallmatrix} b_1 \\ \alpha_1 \end{smallmatrix}\right) e\left(\boldsymbol{\kappa}_\nu \begin{smallmatrix} b_2 \\ \alpha_2 \end{smallmatrix}\right). \quad (\text{B.10})$$

Then divide out  $e\left(-\boldsymbol{\kappa}_\nu \begin{smallmatrix} b_1 \\ \alpha_1 \end{smallmatrix}\right)$  and rearrange to obtain  $3n$  coupled equations:

$$\sum_{\alpha_2, b_2}^{3,n} D_{\boldsymbol{\kappa}}\left(\begin{smallmatrix} b_1 & b_2 \\ \alpha_1 & \alpha_2 \end{smallmatrix}\right) e\left(\boldsymbol{\kappa}_\nu \begin{smallmatrix} b_2 \\ \alpha_2 \end{smallmatrix}\right) - \omega^2(\boldsymbol{\kappa}_\nu) e\left(\boldsymbol{\kappa}_\nu \begin{smallmatrix} b_1 \\ \alpha_1 \end{smallmatrix}\right), \quad (\text{B.11})$$

which can be rewritten as the vector equation  $\underline{D}_{\boldsymbol{\kappa}} \mathbf{e}(\boldsymbol{\kappa}_\nu) = \omega^2(\boldsymbol{\kappa}_\nu) \mathbf{e}(\boldsymbol{\kappa}_\nu)$  (the underscore denotes a matrix). By this point one should be able to see that Eq. (B.11) describes a general eigenvalue problem where  $\omega^2(\boldsymbol{\kappa}_\nu)$  is the eigenvalue of matrix  $\underline{D}_{\boldsymbol{\kappa}}$  associated with eigenvector  $\mathbf{e}(\boldsymbol{\kappa}_\nu)$ . Equation (B.11) provides a procedure to compute the  $3nN$  harmonic frequencies of vibration,  $\omega(\boldsymbol{\kappa}_\nu)$ , for a crystal lattice.

The form of the dynamical matrix allows some statements to be made about its eigenvalues and eigenvectors. First, the dynamical matrix is Hermetian, meaning  $\underline{D}_{\boldsymbol{\kappa}} = \underline{D}_{\boldsymbol{\kappa}}^*$ , where  $*$  denotes the conjugate transpose when applied to a vector or matrix and just the complex conjugate when applied to a scalar. Also for the dynamical matrix

$$D_{\boldsymbol{\kappa}}\left(\begin{smallmatrix} b_1 & b_2 \\ \alpha_1 & \alpha_2 \end{smallmatrix}\right) = D_{-\boldsymbol{\kappa}}^*\left(\begin{smallmatrix} b_1 & b_2 \\ \alpha_1 & \alpha_2 \end{smallmatrix}\right), \quad (\text{B.12})$$

which is easily verifiable using Eq. (B.9). The eigenvalues of a Hermetian matrix are always real. The eigenvectors can be chosen to be orthonormal such that

$$\sum_{\alpha, b}^{3,n} e^*\left(\boldsymbol{\kappa}_\nu \begin{smallmatrix} b \\ \alpha \end{smallmatrix}\right) e\left(\boldsymbol{\kappa}_\nu \begin{smallmatrix} b \\ \alpha \end{smallmatrix}\right) = \delta_{\nu_1 \nu_2} \quad (\text{B.13})$$

$$\sum_{\nu}^{3n} e^*\left(\boldsymbol{\kappa}_\nu \begin{smallmatrix} b_1 \\ \alpha_1 \end{smallmatrix}\right) e\left(\boldsymbol{\kappa}_\nu \begin{smallmatrix} b_2 \\ \alpha_2 \end{smallmatrix}\right) = \delta_{b_1 b_2} \delta_{\alpha_1 \alpha_2}, \quad (\text{B.14})$$

where  $\delta_{ij}$  is the Kronecker delta. The relations

$$\omega^2(\boldsymbol{\kappa}_\nu) = \omega^2(\boldsymbol{\kappa}_\nu) \quad (\text{B.15})$$

$$e(\begin{smallmatrix} \boldsymbol{\kappa} & b \\ \nu & a \end{smallmatrix}) = e^*(\begin{smallmatrix} \boldsymbol{\kappa} & b \\ \nu & a \end{smallmatrix}), \quad (\text{B.16})$$

also follow as a direct consequence of  $\underline{D}_{\boldsymbol{\kappa}}$  being Hermetian and Eq. (B.12). Finally, the inverse Fourier transforms of Eqs. (B.5) are

$$q(\begin{smallmatrix} \boldsymbol{\kappa} \\ \nu \end{smallmatrix}) = N^{-\frac{1}{2}} \sum_{\alpha, b, l}^{3, n, N} m_b^{\frac{1}{2}} u_{\alpha}(\begin{smallmatrix} l \\ b \end{smallmatrix}) e^*(\begin{smallmatrix} \boldsymbol{\kappa} & b \\ \nu & a \end{smallmatrix}) \exp[-i\boldsymbol{\kappa} \cdot \mathbf{r}(\begin{smallmatrix} l \\ b \end{smallmatrix})] \quad (\text{B.17a})$$

$$\dot{q}(\begin{smallmatrix} \boldsymbol{\kappa} \\ \nu \end{smallmatrix}) = N^{-\frac{1}{2}} \sum_{\alpha, b, l}^{3, n, N} m_b^{\frac{1}{2}} \dot{u}_{\alpha}(\begin{smallmatrix} l \\ b \end{smallmatrix}) e^*(\begin{smallmatrix} \boldsymbol{\kappa} & b \\ \nu & a \end{smallmatrix}) \exp[-i\boldsymbol{\kappa} \cdot \mathbf{r}(\begin{smallmatrix} l \\ b \end{smallmatrix})] \quad (\text{B.17b})$$

and  $q^*(\begin{smallmatrix} \boldsymbol{\kappa} \\ \nu \end{smallmatrix}) = q(\begin{smallmatrix} \boldsymbol{\kappa} \\ \nu \end{smallmatrix})$  and  $\dot{q}^*(\begin{smallmatrix} \boldsymbol{\kappa} \\ \nu \end{smallmatrix}) = \dot{q}(\begin{smallmatrix} \boldsymbol{\kappa} \\ \nu \end{smallmatrix})$ .

Now that a means of determining the harmonic frequencies of vibration has been determined and the constraints on the eigenvectors are known, Eq. (B.8) is recast in a simpler form.

$$H_2 = \frac{1}{2} \sum_{\boldsymbol{\kappa}, \nu}^{N, 3n} [\dot{q}^*(\begin{smallmatrix} \boldsymbol{\kappa} \\ \nu \end{smallmatrix}) \dot{q}(\begin{smallmatrix} \boldsymbol{\kappa} \\ \nu \end{smallmatrix}) + \omega^2(\begin{smallmatrix} \boldsymbol{\kappa} \\ \nu \end{smallmatrix}) q^*(\begin{smallmatrix} \boldsymbol{\kappa} \\ \nu \end{smallmatrix}) q(\begin{smallmatrix} \boldsymbol{\kappa} \\ \nu \end{smallmatrix})], \quad (\text{B.18})$$

where Eqs. (B.13), (B.16), and (B.17) have been used. The advantage of transforming the coordinates from  $u$  to  $q$  can now be clearly seen. The transformation allows the harmonic Hamiltonian to be written as a product of  $q$  coordinates which contains no cross terms. If only the harmonic Hamiltonian is considered, the crystal lattice can be treated as  $3nN$  non-interacting sub-systems.

A physically meaningful interpretation of Eq. (B.18) is sought by considering Hamiltonian mechanics. The second derivative of  $q$  is found to be  $\ddot{q}(\begin{smallmatrix} \boldsymbol{\kappa} \\ \nu \end{smallmatrix}) = -\frac{\partial H_2}{\partial q(\begin{smallmatrix} \boldsymbol{\kappa} \\ \nu \end{smallmatrix})} = -\omega^2(\begin{smallmatrix} \boldsymbol{\kappa} \\ \nu \end{smallmatrix}) q(\begin{smallmatrix} \boldsymbol{\kappa} \\ \nu \end{smallmatrix})$ . This equation of motion has solutions of the form  $q(\begin{smallmatrix} \boldsymbol{\kappa} \\ \nu \end{smallmatrix}) = C_1(\begin{smallmatrix} \boldsymbol{\kappa} \\ \nu \end{smallmatrix}) \exp[i\omega(\begin{smallmatrix} \boldsymbol{\kappa} \\ \nu \end{smallmatrix}) t] + C_2(\begin{smallmatrix} \boldsymbol{\kappa} \\ \nu \end{smallmatrix}) \exp[-i\omega(\begin{smallmatrix} \boldsymbol{\kappa} \\ \nu \end{smallmatrix}) t]$ , where  $C_1(\begin{smallmatrix} \boldsymbol{\kappa} \\ \nu \end{smallmatrix})$  and  $C_2(\begin{smallmatrix} \boldsymbol{\kappa} \\ \nu \end{smallmatrix})$  are real constants. The coordinate,  $q(\begin{smallmatrix} \boldsymbol{\kappa} \\ \nu \end{smallmatrix})$ , describes a lattice wave. Using Eq. (B.5a) one finds that

$$u_{\alpha}(\begin{smallmatrix} l \\ b \end{smallmatrix}) = [Nm_b]^{-\frac{1}{2}} \sum_{\boldsymbol{\kappa}, \nu}^{N, 3n} \{C_1(\begin{smallmatrix} \boldsymbol{\kappa} \\ \nu \end{smallmatrix}) \exp[i\omega(\begin{smallmatrix} \boldsymbol{\kappa} \\ \nu \end{smallmatrix}) t] + C_2(\begin{smallmatrix} \boldsymbol{\kappa} \\ \nu \end{smallmatrix}) \exp[-i\omega(\begin{smallmatrix} \boldsymbol{\kappa} \\ \nu \end{smallmatrix}) t]\} e(\begin{smallmatrix} \boldsymbol{\kappa} & b \\ \nu & a \end{smallmatrix}) \exp[i\boldsymbol{\kappa} \cdot \mathbf{r}(\begin{smallmatrix} l \\ b \end{smallmatrix})]. \quad (\text{B.19})$$

The displacement,  $u_\alpha(l)$ , is the real response of an atom due to a superposition of lattice waves. The interpretation is that there exist  $3nN$  non-interacting traveling waves contributing to the motion of the atoms in a crystal lattice. Additionally, since  $q^*(\boldsymbol{\kappa}) = q(\boldsymbol{\kappa})$  and  $\dot{q}^*(\boldsymbol{\kappa}) = \dot{q}(\boldsymbol{\kappa})$ ,  $C_1(\boldsymbol{\kappa}) = C_2(\boldsymbol{\kappa})$  and  $C_2(\boldsymbol{\kappa}) = C_1(\boldsymbol{\kappa})$ .

To further examine the properties of the phonon coordinates,  $q$  and  $\dot{q}$ , consider the displacements and velocities imposed on the atoms of a crystal due to some superposition of phonon modes. Both  $u_\alpha(l)$  and  $\dot{u}_\alpha(l)$  must be real for all vibrational frequencies at all time. This requirement is guaranteed to be satisfied since Eqs. (B.5a) and (B.5b) can be rewritten as

$$u_\alpha(l) = [Nm_b]^{-1/2} \sum_{\nu=1}^{3n} \sum_{\boldsymbol{\kappa} \geq \mathbf{0}} \{ q(\boldsymbol{\kappa}) e(\boldsymbol{\kappa} \mid b) \exp[i\boldsymbol{\kappa} \cdot \mathbf{r}_\alpha(l)] + q(\boldsymbol{\kappa}) e(-\boldsymbol{\kappa} \mid b) \exp[-i\boldsymbol{\kappa} \cdot \mathbf{r}_\alpha(l)] \} \quad (\text{B.20a})$$

$$\dot{u}_\alpha(l) = [Nm_b]^{-1/2} \sum_{\nu=1}^{3n} \sum_{\boldsymbol{\kappa} \geq \mathbf{0}} \{ \dot{q}(\boldsymbol{\kappa}) e(\boldsymbol{\kappa} \mid b) \exp[i\boldsymbol{\kappa} \cdot \mathbf{r}_\alpha(l)] + \dot{q}(\boldsymbol{\kappa}) e(-\boldsymbol{\kappa} \mid b) \exp[-i\boldsymbol{\kappa} \cdot \mathbf{r}_\alpha(l)] \}, \quad (\text{B.20b})$$

where the sums over the wave vectors are only over  $\boldsymbol{\kappa} \geq \mathbf{0}$  and any value involving the negative of the wave vector is just the complex conjugate of the corresponding value for the positive wave vector. For the special cases of when  $\boldsymbol{\kappa}$  is zero or equal to  $\mathbf{K}/2$  (*i.e.*, at the boundary of the first BZ), Eqs. (B.20a) and (B.20b) double count the phonon mode. This situation can be corrected by summing over half of the phonon coordinates (*i.e.*,  $q/2$ ,  $\dot{q}/2$ ). From the properties of the phonon mode coordinates and Eqs. (B.20a) and (B.20b), one should see that, from the point of view of the lattice, a phonon traveling forward with a positive frequency is identical to a phonon traveling backward with a negative frequency.

It is now convenient to introduce the annihilation and creation operators defined by

$$A(\boldsymbol{\kappa}) = [2\hbar\omega(\boldsymbol{\kappa})]^{-\frac{1}{2}} [\omega(\boldsymbol{\kappa}) q(\boldsymbol{\kappa}) + i\dot{q}(\boldsymbol{\kappa})], \quad (\text{B.21a})$$



$$A^*(\boldsymbol{\kappa}) = [2\hbar\omega(\boldsymbol{\nu})]^{-\frac{1}{2}} [\omega(\boldsymbol{\nu}) q(\boldsymbol{\kappa}) - i\dot{q}(\boldsymbol{\kappa})]. \quad (\text{B.21b})$$

In what follows, the properties of these annihilation and creation operators will be used extensively. The properties relevant to the discussion are listed below in Eqs. (B.22)-(B.25) without proof. The details can be found in most introductory textbooks on quantum mechanics [90].

$$[A(\boldsymbol{\nu}_1), A^*(\boldsymbol{\nu}_2)] = \delta_{\mathbf{K}}(\boldsymbol{\kappa}_1 - \boldsymbol{\kappa}_2) \delta_{\nu_1 \nu_2} \quad (\text{B.22})$$

$$[A(\boldsymbol{\nu}_1), A(\boldsymbol{\nu}_2)] = [A^*(\boldsymbol{\nu}_1), A^*(\boldsymbol{\nu}_2)] = 0 \quad (\text{B.23})$$

$$A(\boldsymbol{\nu}) \left| \psi_{f_0(\boldsymbol{\nu})} \right\rangle = f_0^{\frac{1}{2}}(\boldsymbol{\nu}) \left| \psi_{f_0(\boldsymbol{\nu})-1} \right\rangle \quad (\text{B.24})$$

$$A^*(\boldsymbol{\nu}) \left| \psi_{f_0(\boldsymbol{\nu})} \right\rangle = \left[ f_0^{\frac{1}{2}}(\boldsymbol{\nu}) + 1 \right]^{\frac{1}{2}} \left| \psi_{f_0(\boldsymbol{\nu})+1} \right\rangle. \quad (\text{B.25})$$

In the preceding, the bracket with two arguments separated by a comma denotes the commutator, defined by  $[Y, Z] = YZ - ZY$  for any two operators  $Y$  and  $Z$ . The vector  $\boldsymbol{\psi}_i$  is an eigenfunction of the Schrödinger equation,  $H\boldsymbol{\psi}_i = E_i\boldsymbol{\psi}_i$ , with Hamiltonian  $H$  and energy  $E_i$ . Dirac (bra-ket) notation is used to denote a specific eigenstate of the system. In this notation, the ket vector,  $|\psi_X\rangle = \sum_i C_i \boldsymbol{\psi}_i$ , represents the linear combination of eigenfunctions required for a system to be in a state with property  $X$ . Each ket vector has a corresponding bra vector defined as  $\langle\psi_X| = |\psi_X\rangle^*$ , where again  $*$  denotes the conjugate transpose. The property that we will be mostly concerned with is the Bose-Einstein distribution,  $f_0(\boldsymbol{\nu})$ , for each wave vector and dispersion branch. Here, the eigenstate corresponding to a set of specific occupation numbers will be denoted as  $\left| \psi_{f_0(\boldsymbol{\nu})} \right\rangle$ , where the occupation number of wave vector  $\boldsymbol{\kappa}$  and dispersion branch  $\nu$  is explicitly stated, while the others are suppressed. Adding a phonon of wave vector  $\boldsymbol{\kappa}$  and dispersion branch  $\nu$  results in the eigenstate  $\left| \psi_{f_0(\boldsymbol{\nu})+1} \right\rangle$ .

The harmonic Hamiltonian,  $H_2$ , is now written in terms of the creation and annihilation operators. Using Eq. (B.21),

$$q(\boldsymbol{\kappa}) = \left[ \frac{\hbar}{2\omega(\boldsymbol{\kappa})} \right]^{\frac{1}{2}} [A(\boldsymbol{\kappa}) + A^*(\boldsymbol{\kappa})], \quad (\text{B.26a})$$

$$\dot{q}(\boldsymbol{\kappa}) = i \left[ \frac{\hbar\omega(\boldsymbol{\kappa})}{2} \right]^{\frac{1}{2}} [A^*(\boldsymbol{\kappa}) - A(\boldsymbol{\kappa})]. \quad (\text{B.26b})$$

Substituting these expressions into Eq. (B.18), the Hamiltonian becomes

$$\begin{aligned} H_2 &= \frac{1}{2} \sum_{\boldsymbol{\kappa}, \nu}^{N, 3n} \hbar\omega(\boldsymbol{\kappa}) [A(\boldsymbol{\kappa}) A^*(\boldsymbol{\kappa}) + A^*(\boldsymbol{\kappa}) A(\boldsymbol{\kappa})] \\ &= \sum_{\boldsymbol{\kappa}, \nu}^{N, 3n} \hbar\omega(\boldsymbol{\kappa}) \left[ A^*(\boldsymbol{\kappa}) A(\boldsymbol{\kappa}) + \frac{1}{2} \right], \end{aligned} \quad (\text{B.27})$$

where Eqs. (B.22) and (B.23) have been used in the last step. The purpose of the creation and annihilation operators is to make solving the Schrödinger equation easier.

In treating just the harmonic Hamiltonian one can write, for a specific eigenstate,  $H_2 |\psi_{f_0(\boldsymbol{\kappa})}\rangle = E |\psi_{f_0(\boldsymbol{\kappa})}\rangle$  and operate on both sides with  $\langle \psi_{f_0(\boldsymbol{\kappa})} |$  to find a series of  $3nN$  independent equations specified by

$$\begin{aligned} \langle \psi_{f_0(\boldsymbol{\kappa})} | \sum_{\boldsymbol{\kappa}_1, \nu_1}^{N, 3n} \hbar\omega(\boldsymbol{\kappa}_1) \left[ A^*(\boldsymbol{\kappa}_1) A(\boldsymbol{\kappa}_1) + \frac{1}{2} \right] | \psi_{f_0(\boldsymbol{\kappa})} \rangle &= \langle \psi_{f_0(\boldsymbol{\kappa})} | \sum_{\boldsymbol{\kappa}_1, \nu_1}^{N, 3n} E(\boldsymbol{\kappa}_1) | \psi_{f_0(\boldsymbol{\kappa})} \rangle \\ \sum_{\boldsymbol{\kappa}, \nu}^{N, 3n} \hbar\omega(\boldsymbol{\kappa}) \left[ \langle \psi_{f_0(\boldsymbol{\kappa})} | A^*(\boldsymbol{\kappa}) A(\boldsymbol{\kappa}) | \psi_{f_0(\boldsymbol{\kappa})} \rangle + \frac{1}{2} \langle \psi_{f_0(\boldsymbol{\kappa})} | \psi_{f_0(\boldsymbol{\kappa})} \rangle \right] &= \sum_{\boldsymbol{\kappa}, \nu}^{N, 3n} E(\boldsymbol{\kappa}) \langle \psi_{f_0(\boldsymbol{\kappa})} | \psi_{f_0(\boldsymbol{\kappa})} \rangle. \end{aligned} \quad (\text{B.28})$$

The term  $\langle \psi_{f_0(\boldsymbol{\kappa})} | A^*(\boldsymbol{\kappa}) A(\boldsymbol{\kappa}) | \psi_{f_0(\boldsymbol{\kappa})} \rangle$  can be evaluated by using the properties of the creation and annihilation operators listed as Eqs. (B.24) and (B.25). Operating on the ket vector in two steps gives  $f_0^{1/2}(\boldsymbol{\kappa}) \langle \psi_{f_0(\boldsymbol{\kappa})} | A^*(\boldsymbol{\kappa}) | \psi_{f_0(\boldsymbol{\kappa})-1} \rangle = f_0(\boldsymbol{\kappa}) \langle \psi_{f_0(\boldsymbol{\kappa})} | \psi_{f_0(\boldsymbol{\kappa})} \rangle$ . The eigenvalues are orthonormal so Eq. (B.28) becomes  $3nN$  independent equations, all of the form  $E(\boldsymbol{\kappa}) = \hbar\omega(\boldsymbol{\kappa}) [f_0(\boldsymbol{\kappa}) + \frac{1}{2}]$ , which gives the energy of each oscillator.

## B.2 Anharmonic lattice dynamics

With the harmonic portion of the Hamiltonian solved, the anharmonic terms can now be considered. The goal is to transform Eqs. (B.3b) and (B.3c) directly into equations dependent upon the phonon creation and annihilation operators. To do so, first recognize that Eqs. (B.5a) and (B.26a) can be combined to give

$$u_{(\nu)}^{(\kappa)} = \left[ \frac{\hbar}{2Nm_b} \right]^{\frac{1}{2}} \sum_{\kappa, \nu}^{N, 3n} \omega^{-\frac{1}{2}}(\nu) \tilde{e}(\nu \ b) \exp[i\kappa \cdot \mathbf{r}_0^{(l)}] [A(\nu) + A^*(\nu)], \quad (\text{B.29})$$

where  $\tilde{e}(\nu \ b) = e(\nu \ b) \exp[i\kappa \cdot \mathbf{r}_b^{(0)}]$  is just the eigenvector adjusted by a phase shift. By definition all of the identities for  $e(\nu \ b)$ , namely Eqs. (B.13), (B.14), and (B.16), are also valid for  $\tilde{e}(\nu \ b)$ . With the aid of Eq. (B.29),  $H_3$  and  $H_4$  can be written as

$$H_3 = \frac{N}{3!} \left[ \frac{\hbar}{2N} \right]^{\frac{3}{2}} \sum_{\kappa_1, \nu_1}^{N, 3n} \sum_{\kappa_2, \nu_2}^{N, 3n} \sum_{\kappa_3, \nu_3}^{N, 3n} \Phi(\kappa_1 \ \kappa_2 \ \kappa_3) [A(\nu_1) + A^*(\nu_1)] [A(\nu_2) + A^*(\nu_2)] [A(\nu_3) + A^*(\nu_3)], \quad (\text{B.30a})$$

$$H_4 = \frac{N}{4!} \left[ \frac{\hbar}{2N} \right]^2 \sum_{\kappa_1, \nu_1}^{N, 3n} \sum_{\kappa_2, \nu_2}^{N, 3n} \sum_{\kappa_3, \nu_3}^{N, 3n} \sum_{\kappa_4, \nu_4}^{N, 3n} \Phi(\kappa_1 \ \kappa_2 \ \kappa_3 \ \kappa_4) \times [A(\nu_1) + A^*(\nu_1)] [A(\nu_2) + A^*(\nu_2)] [A(\nu_3) + A^*(\nu_3)] [A(\nu_4) + A^*(\nu_4)], \quad (\text{B.30b})$$

where

$$\begin{aligned} \Phi(\kappa_1 \ \kappa_2 \ \dots \ \kappa_i) &= \sum_{\alpha_1, b_1}^{3, n} \sum_{\alpha_2, b_2, l_2}^{3, n, N} \dots \sum_{\alpha_i, b_i, l_i}^{3, n, N} \delta_{\mathbf{K}}(\kappa_1 + \kappa_2 + \dots + \kappa_i) \frac{\partial^i \Phi}{\partial r_{\alpha_1}^{(0)} \partial r_{\alpha_2}^{(l_2)} \dots \partial \mathbf{r}_{\alpha_i}^{(l_i)}} \Big|_o \\ &\times \frac{\tilde{e}(\kappa_1 \ b_1) \tilde{e}(\kappa_2 \ b_2) \dots \tilde{e}(\kappa_i \ b_i)}{\sqrt{m_{b_1} \omega(\nu_1) m_{b_2} \omega(\nu_2) \dots m_{b_i} \omega(\nu_i)}} \exp[i\kappa_2 \cdot \mathbf{r}_0^{(l_2)}] \dots \exp[i\kappa_i \cdot \mathbf{r}_0^{(l_i)}] \end{aligned} \quad (\text{B.31})$$

where the same argument used in Eq. (B.7) to eliminate the summation over  $l_1$  is employed and  $\mathbf{r}_0^{(0)} = \mathbf{0}$  is prescribed to eliminate the first exponential term. Note that  $\Phi(\kappa_1 \ \kappa_2 \ \dots \ \kappa_i)$  is equal to  $\Phi^*(\kappa_1 \ \kappa_2 \ \dots \ \kappa_i)$  and is symmetric under exchange of variable pairs,  $\kappa_1 \leftrightarrow \kappa_2, \ \kappa_2 \leftrightarrow \kappa_i$ , etc.

Since it is known how to treat the harmonic Hamiltonian and its associated annihilation and creation operators, it is desirable to extend these properties to higher order terms in the Hamiltonian and its operators. The Hamiltonian has already been written as Eq. (B.2). Similarly, let a general creation operator of order  $i$  be written as

$$\tilde{A}_i^*(\boldsymbol{\kappa}) = A_2^*(\boldsymbol{\kappa}) + A_3^*(\boldsymbol{\kappa}) + \cdots + A_{i+2}^*(\boldsymbol{\kappa}), \quad (\text{B.32})$$

where  $A_2^*(\boldsymbol{\kappa})$  is the zeroth-order harmonic creation operator defined by Eq. (B.21b).

Take the phonon frequencies to be of the form

$$\Omega_i(\boldsymbol{\kappa}) = \omega_2(\boldsymbol{\kappa}) + \omega_3(\boldsymbol{\kappa}) + \cdots + \omega_{i+2}(\boldsymbol{\kappa}), \quad (\text{B.33})$$

where  $\omega_2(\boldsymbol{\kappa})$  is the harmonic frequency. These creation operators and frequencies mirror the higher order terms in the Hamiltonian therefore one expects that  $\omega_{i-1}(\boldsymbol{\kappa}) \gg \omega_i(\boldsymbol{\kappa})$  and  $\langle \psi_{f_0(\boldsymbol{\kappa})+1} | A_{i-1}^*(\boldsymbol{\kappa}) | \psi_{f_0(\boldsymbol{\kappa})} \rangle \gg \langle \psi_{f_0(\boldsymbol{\kappa})+1} | A_i^*(\boldsymbol{\kappa}) | \psi_{f_0(\boldsymbol{\kappa})} \rangle$ . In general, consider  $A_i^*(\boldsymbol{\kappa})$  and  $\omega_i(\boldsymbol{\kappa})$  to be of order  $\lambda^i$ , where  $\lambda$  is some small parameter. The operators are also required to obey relations analogous to Eqs. (B.22) and (B.23), namely

$$[\tilde{A}_i(\boldsymbol{\kappa}_1), \tilde{A}_i^*(\boldsymbol{\kappa}_2)] = \delta_{\mathbf{K}}(\boldsymbol{\kappa}_1 - \boldsymbol{\kappa}_2) \delta_{\nu_1 \nu_2} + O(\lambda^{i+1}), \quad (\text{B.34})$$

$$[\tilde{A}_i(\boldsymbol{\kappa}_1), \tilde{A}_i(\boldsymbol{\kappa}_2)] = [\tilde{A}_i^*(\boldsymbol{\kappa}_1), \tilde{A}_i^*(\boldsymbol{\kappa}_2)] = O(\lambda^{i+1}). \quad (\text{B.35})$$

The above relations require that the eigenfunctions are orthonormal and accurate to order  $\lambda^i$ .

The end goal is to compute the corrections to the frequencies without first having to explicitly solve the Schrödinger equation. Consider the commutator relation

$$\begin{aligned} [H_2, A_2^*(\boldsymbol{\kappa})] | \psi_{f_0(\boldsymbol{\kappa})} \rangle &= [H_2 A_2^*(\boldsymbol{\kappa}) - A_2^*(\boldsymbol{\kappa}) H_2] | \psi_{f_0(\boldsymbol{\kappa})} \rangle \\ &= [f_0(\boldsymbol{\kappa})+1]^{\frac{1}{2}} [E_{f_0(\boldsymbol{\kappa})+1} - E_{f_0(\boldsymbol{\kappa})}] | \psi_{f_0(\boldsymbol{\kappa})+1} \rangle = \hbar \omega_2(\boldsymbol{\kappa}) A_2^*(\boldsymbol{\kappa}) | \psi_{f_0(\boldsymbol{\kappa})} \rangle, \end{aligned} \quad (\text{B.36})$$

where  $E_{f_0(\nu)}$  is the total energy associated with eigenstate  $|\psi_{f_0(\nu)}\rangle$  and is equal to  $\sum_{\kappa,\nu}^{N,3n} \hbar\omega(\nu) f_0(\nu)$ . If both sides are operated upon with  $\langle\psi_{f_0(\nu)+1}|$ , one obtains  $[f_0(\nu) + 1]^{\frac{1}{2}} \hbar\omega_2(\nu)$  and produces the desirable result of providing the frequency without an explicit need to know the eigenfunctions. It would be advantageous for a similar relation to hold in regards to the commutator of the  $i^{\text{th}}$ -order Hamiltonian and creation operator. Therefore, corrections to the creation operator are chosen such that

$$[\tilde{H}_i, \tilde{A}_i^*(\nu)] |\psi_{i,f_0(\nu)}\rangle = \hbar\Omega_i(\nu) \tilde{A}_i^*(\nu) |\psi_{i,f_0(\nu)}\rangle + O(\lambda^{i+1}), \quad (\text{B.37})$$

where  $|\psi_{i,f_0(\nu)}\rangle$  is the combinations of eigenfunctions, accurate to order  $\lambda^i$ , that describes an eigenstate of the system. Assume that the frequency and creation operator to order  $\lambda^i$  have been determined. Then to determine the next terms in the series one can write

$$[\tilde{H}_{i+1}, \tilde{A}_{i+1}^*(\nu)] |\psi_{i+1,f_0(\nu)}\rangle = \hbar [\Omega_i(\nu) + \omega_{i+1}(\nu)] [\tilde{A}_i^*(\nu) + A_{i+1}^*(\nu)] |\psi_{i+1,f_0(\nu)}\rangle + O(\lambda^{i+2}). \quad (\text{B.38})$$

At this step only the terms of order  $\lambda^i$  are undetermined since all lower order terms have been found previously. Now,

$$\begin{aligned} & [H_2, A_{i-1}^*(\nu)] + [H_3, A_{i-2}^*(\nu)] + \cdots + [H_{i-1}, A_2^*(\nu)] \\ &= \hbar\omega_2(\nu) A_{i-1}^*(\nu) + \hbar\omega_3(\nu) A_{i-2}^*(\nu) + \cdots + \hbar\omega_{i-1}(\nu) A_2^*(\nu). \end{aligned} \quad (\text{B.39})$$

Operate on Eq. (B.39) from the left and right with  $\langle\psi_{i+1,f_0(\nu)+1}|$  and  $|\psi_{i+1,f_0(\nu)}\rangle$ .

With some rearranging one obtains, for the frequency of interest, the equation

$$\begin{aligned} [f_0(\nu) + 1]^{\frac{1}{2}} \hbar\omega_{i-1}(\nu) &= \langle\psi_{i+1,f_0(\nu)+1}| [H_3, A_{i-2}^*(\nu)] + [H_4, A_{i-3}^*(\nu)] + \cdots + [H_{i-1}, A_2^*(\nu)] \\ &\quad - \hbar\omega_3(\nu) A_{i-2}^*(\nu) - \hbar\omega_4(\nu) A_{i-3}^*(\nu) - \cdots - \hbar\omega_{i-2}(\nu) A_3^*(\nu) |\psi_{i+1,f_0(\nu)}\rangle, \end{aligned} \quad (\text{B.40})$$

where the terms involving  $A_{i-1}^*(\boldsymbol{\kappa})$  have canceled. Equation (B.40) can be used recursively to find the frequency to any order. Notice that the creation operators to one order less than the desired frequency are required, however, explicit expressions for the eigenstates are not.

Equation (B.40) can now be used to compute the correction to the harmonic frequencies. Beginning with the first-order correction, Eq. (B.40) is used to write

$$[f_0(\boldsymbol{\kappa}) + 1]^{\frac{1}{2}} \hbar \omega_3(\boldsymbol{\kappa}) = \left\langle \psi_{1,f_0(\boldsymbol{\kappa})+1} \left| [H_3, A_2^*(\boldsymbol{\kappa})] \right| \psi_{1,f_0(\boldsymbol{\kappa})} \right\rangle. \quad (\text{B.41})$$

Upon substitution of Eq. (B.30a) for  $H_3$  the commutator is found to be

$$\frac{N}{3!} \left[ \frac{\hbar}{2N} \right]^{\frac{3}{2}} \left[ \sum_{\boldsymbol{\kappa}_1, \nu_1}^{N,3n} \sum_{\boldsymbol{\kappa}_2, \nu_2}^{N,3n} \sum_{\boldsymbol{\kappa}_3, \nu_3}^{N,3n} \Phi(\boldsymbol{\kappa}_1 \boldsymbol{\kappa}_2 \boldsymbol{\kappa}_3) [A_2(\boldsymbol{\kappa}_1) + A_2^*(\boldsymbol{\kappa}_1)] [A_2(\boldsymbol{\kappa}_2) + A_2^*(\boldsymbol{\kappa}_2)] [A_2(\boldsymbol{\kappa}_3) + A_2^*(\boldsymbol{\kappa}_3)], A_2^*(\boldsymbol{\kappa}) \right]. \quad (\text{B.42})$$

From Eqs. (B.22) and (B.23) one sees that Eq. (B.42) can be non-zero only if  $\boldsymbol{\kappa}_{1,2,or3} = \boldsymbol{\kappa}$  and  $\nu_{1,2,or3} = \nu$  or  $-\boldsymbol{\kappa}_{1,2,or3} = \boldsymbol{\kappa}$  and  $\nu_{1,2,or3} = \nu$ . Consider the cases where  $\boldsymbol{\kappa}_3 = \boldsymbol{\kappa}$  or  $\boldsymbol{\kappa}_3 = -\boldsymbol{\kappa}$  and  $\nu_3 = \nu$ . Equation (B.42) becomes

$$3 \frac{N}{3!} \left[ \frac{\hbar}{2N} \right]^{\frac{3}{2}} \sum_{\boldsymbol{\kappa}_1, \nu_1}^{N,3n} \sum_{\boldsymbol{\kappa}_2, \nu_2}^{N,3n} \Phi(\boldsymbol{\kappa}_1 \boldsymbol{\kappa}_2 \boldsymbol{\kappa}) [A_2(\boldsymbol{\kappa}_1) + A_2^*(\boldsymbol{\kappa}_1)] [A_2(\boldsymbol{\kappa}_2) + A_2^*(\boldsymbol{\kappa}_2)] [A_2(\boldsymbol{\kappa}) + A_2^*(\boldsymbol{\kappa})], A_2^*(\boldsymbol{\kappa})], \quad (\text{B.43})$$

where the factor of three comes from the fact that specifying  $\boldsymbol{\kappa}_3 = \boldsymbol{\kappa}$  and  $\nu_3 = \nu$  is equivalent to specifying  $\boldsymbol{\kappa}_1 = \boldsymbol{\kappa}$  and  $\nu_1 = \nu$  or  $\boldsymbol{\kappa}_2 = \boldsymbol{\kappa}$  and  $\nu_2 = \nu$ . The remaining commutator in Eq. (B.43) evaluates to unity and

$$[H_3, A_2^*(\boldsymbol{\kappa})] = 3 \frac{N}{3!} \left[ \frac{\hbar}{2N} \right]^{\frac{3}{2}} \sum_{\boldsymbol{\kappa}_1, \nu_1}^{N,3n} \sum_{\boldsymbol{\kappa}_2, \nu_2}^{N,3n} \Phi(\boldsymbol{\kappa}_1 \boldsymbol{\kappa}_2 \boldsymbol{\kappa}) [A_2(\boldsymbol{\kappa}_1) + A_2^*(\boldsymbol{\kappa}_1)] [A_2(\boldsymbol{\kappa}_2) + A_2^*(\boldsymbol{\kappa}_2)]. \quad (\text{B.44})$$

Upon substituting this expression into Eq. (B.41) one finds that there is no combination of operators acting on the eigenstate that turn  $|\psi_{1,f_0(\boldsymbol{\kappa})}\rangle$  into  $|\psi_{1,f_0(\boldsymbol{\kappa})+1}\rangle$ . Therefore all terms on the right hand side are zero and the first order corrections to the frequencies are zero.

The second order frequency corrections are to be found by

$$[f_0(\boldsymbol{\kappa}) + 1]^{\frac{1}{2}} \hbar \omega_4(\boldsymbol{\kappa}) = \left\langle \psi_{2,f_0(\boldsymbol{\kappa})+1} \left| [H_3, A_3^*(\boldsymbol{\kappa})] + [H_4, A_2^*(\boldsymbol{\kappa})] - \hbar \omega_3(\boldsymbol{\kappa}) \right| \psi_{2,f_0(\boldsymbol{\kappa})} \right\rangle, \quad (\text{B.45})$$

which, again, follows from Eq. (B.40). Having just found that  $\omega_3(\boldsymbol{\kappa}) = 0$ , the first-order correction to the creation operator,  $A_3^*(\boldsymbol{\kappa})$ , needs to be determined before Eq. (B.45) can be evaluated. Equation (B.37) is used to state that the new operator should satisfy

$$[H_2 + H_3, A_2^*(\boldsymbol{\kappa}) + A_3^*(\boldsymbol{\kappa})] = \hbar \omega_2(\boldsymbol{\kappa}) [A_2^*(\boldsymbol{\kappa}) + A_3^*(\boldsymbol{\kappa})] + O(\lambda^2), \quad (\text{B.46})$$

where, once again, the fact that  $\omega_3(\boldsymbol{\kappa}) = 0$  has been used. Considering only the non-zero first order terms, Eq. (B.46) is recast as

$$[H_2, A_3^*(\boldsymbol{\kappa})] + [H_3, A_2^*(\boldsymbol{\kappa})] = [\hbar \omega_2(\boldsymbol{\kappa}) \pm i\hbar\epsilon] A_3^*(\boldsymbol{\kappa}), \quad (\text{B.47})$$

where  $\epsilon$  is an infinitesimally small positive value, introduced to avoid degeneracies.

Later,  $\epsilon$  will be removed by taking the limit  $\epsilon \rightarrow 0$ . Equation (B.47) suggests that  $A_3^*(\boldsymbol{\kappa})$  should have the same form as  $[H_3, A_2^*(\boldsymbol{\kappa})]$  so let

$$\begin{aligned} A_3^*(\boldsymbol{\kappa}) = & \frac{N}{3!} \left[ \frac{\hbar}{2N} \right]^{\frac{3}{2}} \sum_{\boldsymbol{\kappa}, \nu}^{N, 3n} \sum_{\boldsymbol{\kappa}_1, \nu_1}^{N, 3n} \sum_{\boldsymbol{\kappa}_2, \nu_2}^{N, 3n} \Phi_{(\nu \nu_1 \nu_2)}^{(\boldsymbol{\kappa} \boldsymbol{\kappa}_1 \boldsymbol{\kappa}_2)} [\alpha_{(\nu \nu_1 \nu_2)}^{(\boldsymbol{\kappa} \boldsymbol{\kappa}_1 \boldsymbol{\kappa}_2)} A_2(\boldsymbol{\kappa}_1) A_2(\boldsymbol{\kappa}_2) + \beta_{(\nu \nu_1 \nu_2)}^{(\boldsymbol{\kappa} \boldsymbol{\kappa}_1 \boldsymbol{\kappa}_2)} A_2(\boldsymbol{\kappa}_1) A_2^*(\boldsymbol{\kappa}_2) \\ & + \eta_{(\nu \nu_1 \nu_2)}^{(\boldsymbol{\kappa} \boldsymbol{\kappa}_1 \boldsymbol{\kappa}_2)} A_2^*(\boldsymbol{\kappa}_1) A_2(\boldsymbol{\kappa}_2) + \zeta_{(\nu \nu_1 \nu_2)}^{(\boldsymbol{\kappa} \boldsymbol{\kappa}_1 \boldsymbol{\kappa}_2)} A_2^*(\boldsymbol{\kappa}_1) A_2^*(\boldsymbol{\kappa}_2)], \end{aligned} \quad (\text{B.48})$$

where  $\alpha_{(\nu \nu_1 \nu_2)}^{(\boldsymbol{\kappa} \boldsymbol{\kappa}_1 \boldsymbol{\kappa}_2)}$ ,  $\beta_{(\nu \nu_1 \nu_2)}^{(\boldsymbol{\kappa} \boldsymbol{\kappa}_1 \boldsymbol{\kappa}_2)}$ ,  $\eta_{(\nu \nu_1 \nu_2)}^{(\boldsymbol{\kappa} \boldsymbol{\kappa}_1 \boldsymbol{\kappa}_2)}$ , and  $\zeta_{(\nu \nu_1 \nu_2)}^{(\boldsymbol{\kappa} \boldsymbol{\kappa}_1 \boldsymbol{\kappa}_2)}$  are coefficients that must be determined. Equation (B.48) is used to evaluate the commutator relation,

$$\begin{aligned} [H_2, A_3^*(\boldsymbol{\kappa})] = & \frac{N}{3!} \left[ \frac{\hbar}{2N} \right]^{\frac{3}{2}} \sum_{\boldsymbol{\kappa}_1, \nu_1}^{N, 3n} \sum_{\boldsymbol{\kappa}_2, \nu_2}^{N, 3n} \Phi_{(\nu \nu_1 \nu_2)}^{(\boldsymbol{\kappa} \boldsymbol{\kappa}_1 \boldsymbol{\kappa}_2)} [\hbar \alpha_{(\nu \nu_1 \nu_2)}^{(\boldsymbol{\kappa} \boldsymbol{\kappa}_1 \boldsymbol{\kappa}_2)} (-\omega_2(\boldsymbol{\kappa}_1) - \omega_2(\boldsymbol{\kappa}_2)) A_2(\boldsymbol{\kappa}_1) A_2(\boldsymbol{\kappa}_2) \\ & + \hbar \beta_{(\nu \nu_1 \nu_2)}^{(\boldsymbol{\kappa} \boldsymbol{\kappa}_1 \boldsymbol{\kappa}_2)} (-\omega_2(\boldsymbol{\kappa}_1) + \omega_2(\boldsymbol{\kappa}_2)) A_2(\boldsymbol{\kappa}_1) A_2^*(\boldsymbol{\kappa}_2) + \hbar \eta_{(\nu \nu_1 \nu_2)}^{(\boldsymbol{\kappa} \boldsymbol{\kappa}_1 \boldsymbol{\kappa}_2)} (\omega_2(\boldsymbol{\kappa}_1) - \omega_2(\boldsymbol{\kappa}_2)) A_2^*(\boldsymbol{\kappa}_1) A_2(\boldsymbol{\kappa}_2) \\ & + \hbar \zeta_{(\nu \nu_1 \nu_2)}^{(\boldsymbol{\kappa} \boldsymbol{\kappa}_1 \boldsymbol{\kappa}_2)} (\omega_2(\boldsymbol{\kappa}_1) + \omega_2(\boldsymbol{\kappa}_2)) A_2^*(\boldsymbol{\kappa}_1) A_2^*(\boldsymbol{\kappa}_2)]. \end{aligned} \quad (\text{B.49})$$

Now use Eqs. (B.44), (B.48), and (B.49) by inserting the expressions for  $[H_3, A_2^*(\kappa)]$ ,  $A_3^*(\nu)$ , and  $[H_2, A_3^*(\kappa)]$  into Eq. (B.47) to find

$$\begin{aligned}
\frac{N}{3!} \left[ \frac{\hbar}{2N} \right]^{\frac{3}{2}} \sum_{\kappa_1, \nu_1}^{N, 3n} \sum_{\kappa_2, \nu_2}^{N, 3n} \Phi(\kappa_{\nu_1 \nu_2}^{\kappa_1 \kappa_2}) \{ [3 - \hbar \alpha(\kappa_{\nu_1 \nu_2}^{\kappa_1 \kappa_2}) (\omega_2(\kappa_{\nu_1}) + \omega_2(\kappa_2) \pm i\epsilon) A_2(\kappa_1) A_2(\kappa_2)] \\
+ [3 - \hbar \beta(\kappa_{\nu_1 \nu_2}^{\kappa_1 \kappa_2}) (\omega_2(\kappa_{\nu_1}) - \omega_2(\kappa_2) \pm i\epsilon) A_2(\kappa_1) A_2(\kappa_2)] \\
+ [3 - \hbar \eta(\kappa_{\nu_1 \nu_2}^{\kappa_1 \kappa_2}) (\omega_2(\kappa_{\nu_1}) + \omega_2(\kappa_2) \pm i\epsilon) A_2(\kappa_1) A_2(\kappa_2)] \\
+ [3 - \hbar \zeta(\kappa_{\nu_1 \nu_2}^{\kappa_1 \kappa_2}) (\omega_2(\kappa_{\nu_1}) - \omega_2(\kappa_2) \pm i\epsilon) A_2(\kappa_1) A_2(\kappa_2)] \} = 0.
\end{aligned} \tag{B.50}$$

Equation (B.50) must be zero when operating on any eigenstate. Thus, the coefficients on all creation and annihilation operators are zero and

$$\alpha(\kappa_{\nu_1 \nu_2}^{\kappa_1 \kappa_2}) = \frac{3}{\hbar} (\omega_2(\kappa_{\nu_1}) + \omega_2(\kappa_2) \pm i\epsilon)^{-1} \tag{B.51a}$$

$$\beta(\kappa_{\nu_1 \nu_2}^{\kappa_1 \kappa_2}) = \frac{3}{\hbar} (\omega_2(\kappa_{\nu_1}) - \omega_2(\kappa_2) \pm i\epsilon)^{-1} \tag{B.51b}$$

$$\eta(\kappa_{\nu_1 \nu_2}^{\kappa_1 \kappa_2}) = \frac{3}{\hbar} (\omega_2(\kappa_{\nu_1}) + \omega_2(\kappa_2) \pm i\epsilon)^{-1} \tag{B.51c}$$

$$\zeta(\kappa_{\nu_1 \nu_2}^{\kappa_1 \kappa_2}) = \frac{3}{\hbar} (\omega_2(\kappa_{\nu_1}) - \omega_2(\kappa_2) \pm i\epsilon)^{-1} \tag{B.51d}$$

Now that  $A_3^*(\nu)$  is determined, the terms in Eq. (B.45) can be evaluated. First, consider  $[H_4, A_2^*(\kappa)]$ , which by the same arguments used to obtain Eq. (B.44) is

$$\begin{aligned}
& [H_4, A_2^*(\kappa)] \\
&= 4 \frac{N}{4!} \left[ \frac{\hbar}{2N} \right]^2 \sum_{\kappa_1, \nu_1}^{N, 3n} \sum_{\kappa_2, \nu_2}^{N, 3n} \sum_{\kappa_3, \nu_3}^{N, 3n} \Phi(\kappa_{\nu_1 \nu_2 \nu_3}^{\kappa_1 \kappa_2 \kappa_3}) [A_2(\kappa_1) + A_2^*(\kappa_1)] [A_2(\kappa_2) + A_2^*(\kappa_2)] [A_2(\kappa_3) + A_2^*(\kappa_3)].
\end{aligned} \tag{B.52}$$

Multiplying out the creation and annihilation operators yields eight triplets of operators. Each triplet of operators must transform  $|\psi_{2, f_0(\kappa)}\rangle$  into  $|\psi_{2, f_0(\kappa)+1}\rangle$  otherwise its contribution to Eq. (B.45) is zero. The only way for a product of three creation



and annihilation operators to satisfy this condition is for the product to contain the terms  $A_2^*(\kappa)$ ,  $A_2^*(\kappa')$ , and  $A_2(\kappa')$  in any order. The contributing terms are

$$\begin{aligned}
& \left\langle \psi_{2,f_0(\kappa)_+1} \left| [H_4, A_2^*(\kappa)] \right| \psi_{2,f_0(\kappa)} \right\rangle \\
&= 4 \frac{N}{4!} \left[ \frac{\hbar}{2N} \right]^2 \left\langle \psi_{2,f_0(\kappa)_+1} \left| \sum_{\kappa', \nu'}^{N, 3n} \left\{ \Phi(\kappa \kappa' - \kappa - \kappa')_{\nu \nu' \nu \nu'} [A_2(\kappa') A_2^*(\kappa) A_2^*(\kappa') + A_2^*(\kappa') A_2^*(\kappa) A_2(\kappa')] \right. \right. \right. \\
&\quad \left. \Phi(\kappa \kappa' - \kappa' - \kappa)_{\nu \nu' \nu' \nu} [A_2(\kappa') A_2^*(\kappa') A_2^*(\kappa) + A_2^*(\kappa') A_2(\kappa') A_2^*(\kappa)] \right. \\
&\quad \left. \left. \Phi(\kappa - \kappa \kappa' - \kappa')_{\nu \nu \nu' \nu'} [A_2^*(\kappa) A_2(\kappa') A_2^*(\kappa') + A_2^*(\kappa) A_2^*(\kappa') A_2(\kappa')] \right\} \right| \psi_{2,f_0(\kappa)} \right\rangle, \quad (\text{B.53})
\end{aligned}$$

where in the last line, for example, the substitutions  $\kappa_1 = -\kappa$  and  $\kappa_2 = -\kappa_3 = \kappa'$  are used. Operating on the eigenstate with these triplets one finds

$$\begin{aligned}
& \left\langle \psi_{2,f_0(\kappa)_+1} \left| [H_4, A_2^*(\kappa)] \right| \psi_{2,f_0(\kappa)} \right\rangle = 4 \frac{N}{4!} \left[ \frac{\hbar}{2N} \right]^2 [f_0(\kappa) + 1]^{\frac{1}{2}} \\
& \times \left\{ \sum_{\kappa', \nu' \neq \kappa, \nu} \Phi(\kappa \kappa' - \kappa - \kappa')_{\nu \nu' \nu \nu'} [2(f_0(\kappa') + 1) + f_0(\kappa)] + \sum_{\kappa', \nu' \neq -\kappa, \nu} \Phi(\kappa \kappa' - \kappa - \kappa')_{\nu \nu' \nu \nu'} [(f_0(\kappa') + 1) + 2f_0(\kappa)] \right. \\
& \quad \left. + 2\Phi(\kappa \kappa - \kappa - \kappa)_{\nu \nu \nu \nu} [(f_0(\kappa) + 2) + (f_0(\kappa) + 1) + f_0(\kappa)] \right\}, \quad (\text{B.54})
\end{aligned}$$

where  $\kappa', \nu' \neq \kappa, \nu$  denotes that the sum is over all values of  $\kappa'$  and  $\nu'$  such that  $\kappa' \neq \kappa$  and  $\nu' \neq \nu$ . Equation (B.54) is arrived at by using the fact that  $\Phi(\kappa_1 \kappa_2 \kappa_3 \kappa_4)_{\nu_1 \nu_2 \nu_3 \nu_4}$  is symmetric under exchange of variables. Regrouping the terms to allow the sums to run over all wave vectors and dispersion branches one finds

$$\begin{aligned}
& \left\langle \psi_{2,f_0(\kappa)_+1} \left| [H_4, A_2^*(\kappa)] \right| \psi_{2,f_0(\kappa)} \right\rangle = 4 \frac{N}{4!} \left[ \frac{\hbar}{2N} \right]^2 [f_0(\kappa) + 1]^{\frac{1}{2}} \\
& \quad \times \left\{ \sum_{\kappa', \nu'}^{N, 3n} \Phi(\kappa \kappa' - \kappa - \kappa')_{\nu \nu' \nu \nu'} [2f_0(\kappa') + 1] + 2\Phi(\kappa \kappa - \kappa - \kappa)_{\nu \nu \nu \nu} \right\}. \quad (\text{B.55})
\end{aligned}$$

The rightmost term can safely be neglected since it is a single value while the sum is over  $3nN$  values. Note that  $\Phi(\kappa \kappa' - \kappa - \kappa')_{\nu \nu' \nu \nu'}$  contains the delta function which is always satisfied since  $\delta_{\mathbf{K}}(\kappa + \kappa' - \kappa - \kappa') = \delta_{\mathbf{K}}(0) = 1$ .

Now consider  $\left\langle \psi_{2,f_0(\kappa_\nu)+1} \left| [H_3, A_3^*(\kappa_\nu)] \right| \psi_{2,f_0(\kappa_\nu)} \right\rangle$ . The commutators contain the products of five creation and annihilation operators. Since these operators are required to transform the eigenstate  $\left| \psi_{2,f_0(\kappa_\nu)} \right\rangle$  into  $\left| \psi_{2,f_0(\kappa_\nu)+1} \right\rangle$ , only the products that contain three creation and two annihilation operators need to be considered. Using the expressions for  $H_3$  and  $A_3^*(\kappa_\nu)$  and dropping irrelevant terms one can find

$$\begin{aligned}
& \left\langle \psi_{2,f_0(\kappa_\nu)+1} \left| [H_3, A_3^*(\kappa_\nu)] \right| \psi_{2,f_0(\kappa_\nu)} \right\rangle = \\
& \frac{\hbar^3}{288N} \left\langle \psi_{2,f_0(\kappa_\nu)+1} \left| \sum_{\kappa_1, \nu_1}^{N,3n} \sum_{\kappa_2, \nu_2}^{N,3n} \sum_{\kappa_3, \nu_3}^{N,3n} \sum_{\kappa', \nu'}^{N,3n} \sum_{\kappa'', \nu''}^{N,3n} \Phi(\kappa_1 \kappa_2 \kappa_3) \Phi(\kappa \kappa' \kappa'') \right. \right. \\
& \times \left\{ \zeta(\kappa \kappa' \kappa'') [A_2(\kappa_1) A_2(\kappa_2) A_2^*(\kappa_3) + A_2(\kappa_1) A_2^*(\kappa_2) A_2(\kappa_3) + A_2^*(\kappa_1) A_2(\kappa_2) A_2(\kappa'')] , A_2^*(\kappa') A_2^*(\kappa'')] \right. \\
& - \alpha(\kappa \kappa' \kappa'') [A_2^*(\kappa_1) A_2^*(\kappa_2) A_2^*(\kappa_3) , A_2(\kappa') A_2(\kappa'')] \\
& + [A_2(\kappa_1) A_2^*(\kappa_2) A_2^*(\kappa_3) + A_2^*(\kappa_1) A_2(\kappa_2) A_2^*(\kappa_3) + A_2^*(\kappa_1) A_2^*(\kappa_2) A_2(\kappa_3) , \\
& \left. \left. \eta(\kappa \kappa' \kappa'') A_2^*(\kappa') A_2(\kappa'') - \beta(\kappa \kappa' \kappa'') A_2(\kappa') A_2^*(\kappa'')] \right\} \left| \psi_{2,f_0(\kappa_\nu)} \right\rangle . \tag{B.56}
\end{aligned}$$

Equation (B.56) needs to be evaluated for all possible combinations of wave vectors and dispersion branches that increases the occupation number,  $f_0(\kappa_\nu)$ , by one, leaving the others unchanged. This is the same procedure used to go from Eq. (B.53) to Eq. (B.54). The only difference here is that both the expression to evaluate and the result are far more complicated. Here the result is presented without details to be

$$\begin{aligned}
& \left\langle \psi_{2,f_0(\kappa_\nu)+1} \left| [H_3, A_3^*(\kappa_\nu)] \right| \psi_{2,f_0(\kappa_\nu)} \right\rangle = [f_0(\kappa_\nu) + 1]^{\frac{1}{2}} \frac{\hbar^3}{48N} \sum_{\kappa', \nu'}^{N,3n} \sum_{\kappa'', \nu''}^{N,3n} \Phi(\kappa \kappa' \kappa'') \Phi(\kappa - \kappa' - \kappa'') \\
& \times \left\{ [\zeta(\kappa \kappa' \kappa'') - \alpha(\kappa \kappa' \kappa'')] [f_0(\kappa') + f_0(\kappa'') + 1] + [\beta(\kappa \kappa' \kappa'') - \eta(\kappa \kappa' \kappa'')] [f_0(\kappa') - f_0(\kappa'')] \right\} \\
& + \frac{\hbar^3}{24N} \sum_{\kappa', \nu'}^{N,3n} \sum_{\nu''}^{3n} \Phi(\kappa - \kappa \ 0) \Phi(\kappa' - \kappa' \ 0) [\eta(\kappa \kappa \ 0) - \zeta(\kappa \ \nu \ \nu'')] [2f_0(\kappa_\nu) + 1] , \tag{B.57}
\end{aligned}$$

which has been simplified by neglecting terms where the sums run over less than two wave vectors. The neglect of these terms can be justified by recalling that  $\Phi(\kappa \kappa' \kappa'')$

contains  $\delta_{\mathbf{K}}(\boldsymbol{\kappa} + \boldsymbol{\kappa}' + \boldsymbol{\kappa}'')$ , which for each pair of wave vectors  $\boldsymbol{\kappa}$  and  $\boldsymbol{\kappa}'$  constrains  $\boldsymbol{\kappa}''$  to a single value. Because of this, the sums in Eq. (B.57) run over only  $3nN \times 3n$  nonzero terms. The neglected sums contain the terms like  $\delta_{\mathbf{K}}(\boldsymbol{\kappa} - \boldsymbol{\kappa} + \boldsymbol{\kappa}')$  or  $\delta_{\mathbf{K}}(\boldsymbol{\kappa} + \boldsymbol{\kappa} + \boldsymbol{\kappa})$ , which can only contribute  $3n$  or  $1$  term to Eq. (B.57).

The final step in the derivation is to take the limit  $\epsilon \rightarrow 0$  in Eq. (B.57). Each term in the right hand side of Eq. (B.57) is of the form  $\sum_{\sigma} \frac{f_{\sigma}}{\omega_{\sigma} \pm i\epsilon}$ , where  $\boldsymbol{\kappa}'$ ,  $\nu'$ ,  $\boldsymbol{\kappa}''$ , and  $\nu''$  are represented by the single variable  $\sigma$ ,  $f_{\sigma}$  is any function of  $\sigma$ , and  $\omega_{\sigma} \pm i\epsilon$  is the denominator of  $\alpha$ ,  $\beta$ ,  $\eta$ , or  $\zeta$ . Take the limit to arrive at

$$\lim_{\epsilon \rightarrow 0^+} \sum_{\sigma} \frac{f_{\sigma}}{\omega_{\sigma} \pm i\epsilon} = \lim_{\epsilon \rightarrow 0^+} \sum_{\sigma} f_{\sigma} \left[ \frac{\omega_{\sigma}}{\omega_{\sigma}^2 + \epsilon^2} \mp i \frac{\epsilon}{\omega_{\sigma}^2 + \epsilon^2} \right] = f_{\sigma} \sum_{\sigma} \left[ \frac{1}{\omega_{\sigma}} \mp i\pi \delta(\omega_{\sigma}) \right], \quad (\text{B.58})$$

where the Dirac delta function follows from one of its definitions,  $\delta(\omega_{\sigma}) = \lim_{\epsilon \rightarrow 0^+} \frac{\epsilon/\pi}{\omega_{\sigma}^2 + \epsilon^2}$ , and has the property that

$$\int_{-\infty}^{\infty} g(x) \delta(x - a) dx = g(a) \quad (\text{B.59})$$

for any function  $g(x)$ . If there are enough points in the first Brillouin zone,  $\omega_{\sigma}$  will essentially range over a continuum of energies,  $a \leq \omega_{\sigma} \leq b$ , and the summation in Eq. (B.58) can be approximated by an integral. Doing so, it is found that

$$\begin{aligned} f_{\sigma} \sum_{\sigma} \frac{1}{\omega_{\sigma}} &\rightarrow \frac{1}{D} \int_a^b \frac{f_{\sigma}}{\omega_{\sigma}} d\omega_{\sigma} = \frac{1}{D} \lim_{\gamma \rightarrow 0^+} \left[ \int_a^{0-\gamma} \frac{f_{\sigma}}{\omega_{\sigma}} d\omega_{\sigma} + \int_{0+\gamma}^b \frac{f_{\sigma}}{\omega_{\sigma}} d\omega_{\sigma} \right] \\ &= \frac{1}{D} \int_a^b \frac{f_{\sigma}}{(\omega_{\sigma})_p} d\omega_{\sigma} \rightarrow f_{\sigma} \sum_{\sigma} \frac{1}{(\omega_{\sigma})_p}, \end{aligned} \quad (\text{B.60})$$

where  $D = (b - a)/(3nN)$  is the average spacing between  $\omega_{\sigma}$  values and  $(x)_p$  denotes the Cauchy principal value, defined by

$$\int_a^b (g(x))_p dx = \lim_{\gamma \rightarrow 0^+} \left[ \int_a^{c-\gamma} g(x) dx + \int_{c+\gamma}^b g(x) dx \right] \quad (\text{B.61})$$

for  $a < c < b$ . Using this result,

$$\lim_{\epsilon \rightarrow 0^+} \sum_{\sigma} \frac{f_{\sigma}}{\omega_{\sigma} \pm i\epsilon} = \sum_{\sigma} f_{\sigma} \left[ \frac{1}{(\omega_{\sigma})_p} \mp i\pi \delta(\omega_{\sigma}) \right]. \quad (\text{B.62})$$

Equation (B.62) can be applied to each term in Eq. (B.57) to yield a real and imaginary part of the frequency correction.

The corrections to the harmonic frequencies accurate to second order can now be specified. By taking the limit as  $\epsilon \rightarrow 0$  of Eq. (B.57) and using the result with Eqs. (B.45) and (B.55) the frequency shift and linewidth can be written as

$$\begin{aligned}
\Delta(\kappa) = & \frac{\hbar}{16N} \sum_{\kappa', \nu'}^{N, 3n} \sum_{\kappa'', \nu''}^{N, 3n} |\Phi(\kappa_{\nu} \kappa'_{\nu'} \kappa''_{\nu''})|^2 \left\{ [f_0(\kappa'_{\nu'}) + f_0(\kappa''_{\nu''}) + 1] \left[ (\omega(\kappa_{\nu}) - \omega(\kappa'_{\nu'}) - \omega(\kappa''_{\nu''}))_p^{-1} - (\omega(\kappa_{\nu}) + \omega(\kappa'_{\nu'}) + \omega(\kappa''_{\nu''}))_p^{-1} \right] \right. \\
& + [f_0(\kappa'_{\nu'}) - f_0(\kappa''_{\nu''})] \left[ (\omega(\kappa_{\nu}) + \omega(\kappa'_{\nu'}) - \omega(\kappa''_{\nu''}))_p^{-1} - (\omega(\kappa_{\nu}) - \omega(\kappa'_{\nu'}) + \omega(\kappa''_{\nu''}))_p^{-1} \right] \Big\} \\
& + \frac{\hbar}{8N} \sum_{\kappa', \nu'}^{N, 3n} \sum_{\nu''}^{3n} \Phi(\kappa_{\nu} - \kappa'_{\nu'} \mathbf{0}_{\nu''}) \Phi(\kappa'_{\nu'} - \kappa''_{\nu''} \mathbf{0}_{\nu''}) [2f_0(\kappa'_{\nu'}) + 1] (\omega(\mathbf{0}_{\nu''}))_p^{-1} \\
& + \frac{\hbar}{8N} \sum_{\kappa', \nu'}^{N, 3n} \Phi(\kappa_{\nu} \kappa'_{\nu'} - \kappa_{\nu} - \kappa'_{\nu'}) [2f_0(\kappa'_{\nu'}) + 1] \quad (B.63)
\end{aligned}$$

$$\begin{aligned}
\Gamma(\kappa) = & \frac{\pi \hbar}{16N} \sum_{\kappa', \nu'}^{N, 3n} \sum_{\kappa'', \nu''}^{N, 3n} |\Phi(\kappa_{\nu} \kappa'_{\nu'} \kappa''_{\nu''})|^2 \left\{ [f_0(\kappa'_{\nu'}) + f_0(\kappa''_{\nu''}) + 1] [\delta(\omega(\kappa_{\nu}) - \omega(\kappa'_{\nu'}) - \omega(\kappa''_{\nu''})) - \delta(\omega(\kappa_{\nu}) + \omega(\kappa'_{\nu'}) + \omega(\kappa''_{\nu''}))] \right. \\
& + [f_0(\kappa'_{\nu'}) - f_0(\kappa''_{\nu''})] [\delta(\omega(\kappa_{\nu}) + \omega(\kappa'_{\nu'}) - \omega(\kappa''_{\nu''})) - \delta(\omega(\kappa_{\nu}) - \omega(\kappa'_{\nu'}) + \omega(\kappa''_{\nu''}))] \Big\} \\
& + \frac{\pi \hbar}{8N} \sum_{\kappa', \nu'}^{N, 3n} \sum_{\nu''}^{3n} \Phi(\kappa_{\nu} - \kappa'_{\nu'} \mathbf{0}_{\nu''}) \Phi(\kappa'_{\nu'} - \kappa''_{\nu''} \mathbf{0}_{\nu''}) [2f_0(\kappa'_{\nu'}) + 1] \delta(\omega(\mathbf{0}_{\nu''})) \quad (B.64)
\end{aligned}$$

where the subscript on the harmonic frequencies,  $\omega_2(\kappa)$ , has been dropped. The sums in  $\Delta(\kappa)$  and  $\Gamma(\kappa)$  do not include the zone-center acoustic phonons since these phonons correspond to bulk translation of the lattice and cannot interact with other phonons.

The frequency shift and linewidth given by Eqs. (B.63) and (B.64) are the second-order corrections to the harmonic frequency. A phonon with wave vector  $\kappa$  and dispersion branch  $\nu$ , perturbed from equilibrium is described by  $q(\kappa) = q_T(\kappa) + q_{SS}(\kappa)$ , where

$q_{SS}(\boldsymbol{\kappa})$  and  $q_T(\boldsymbol{\kappa})$  are the steady-state (equilibrium) and transient solutions. These take the forms

$$q_{SS}(\boldsymbol{\kappa}) = C_1 \exp[i(\omega(\boldsymbol{\kappa}) + \Delta(\boldsymbol{\kappa}))t] + C_2 \exp[-i(\omega(\boldsymbol{\kappa}) + \Delta(\boldsymbol{\kappa}))t] \quad (\text{B.65a})$$

$$q_T(\boldsymbol{\kappa}) = C_3 \exp[-\Gamma(\boldsymbol{\kappa})t] \{ \exp[i(\omega(\boldsymbol{\kappa}) + \Delta(\boldsymbol{\kappa}))t] + C_4 \exp[-i(\omega(\boldsymbol{\kappa}) + \Delta(\boldsymbol{\kappa}))t] \} \quad (\text{B.65b})$$

where the  $C$ 's are real constants. The transient term describes a dampened excitation in the phonon amplitude. The primary concern is with the decay of the energy carried by each phonon. From Eq. (B.18) one sees that the transient phonon energy is given by  $2E_T(\boldsymbol{\kappa}) = \omega^2(\boldsymbol{\kappa}) q_T^*(\boldsymbol{\kappa}) q_T(\boldsymbol{\kappa}) + \dot{q}_T^*(\boldsymbol{\kappa}) \dot{q}_T(\boldsymbol{\kappa})$ . Finally, the expected phonon lifetime (relaxation time),

$$\tau(\boldsymbol{\kappa}) = \frac{\int_0^\infty t E_T(\boldsymbol{\kappa}) dt}{\int_0^\infty E_T(\boldsymbol{\kappa}) dt}, \quad (\text{B.66})$$

is found to be related to the linewidth by

$$\tau(\boldsymbol{\kappa}) = [2\Gamma(\boldsymbol{\kappa})]^{-1}. \quad (\text{B.67})$$

As described in Section 2.3.2, Eqs. (B.63) and (B.64) for the frequency shift and linewidth are evaluated by using

$$\frac{1}{(\omega)_p} \approx \frac{\omega}{\omega^2 + \epsilon^2} \quad (\text{B.68})$$

and

$$\delta(\omega) \approx \frac{1}{\pi} \frac{\epsilon}{\omega^2 + \epsilon^2} \quad (\text{B.69})$$

to approximate the Cauchy principal value and Dirac delta function. The forms of Eqs. (B.68) and (B.69) can be justified by observing that these equations appear in Eq. (B.58). In order to obtain the Cauchy principal value and Dirac delta function, the limit of  $\epsilon \rightarrow 0^+$  is taken for Eqs. (B.68) and (B.69). The parameter  $\epsilon$  is introduced in Eq. (B.47) as a way to avoid degeneracies. Because  $\epsilon$  is introduced in this manner,

the parameter must be taken to zero to eliminate it at some later stage. However, by writing Eq. (B.29) in a more accurate way, one can avoid the use of  $\epsilon$  altogether.

Equation (B.29) is derived from Eqs. (B.5a) and (B.26a) which are valid under the harmonic approximation. Using the results of anharmonic lattice dynamics, Eq. (B.29) can be rewritten more accurately as

$$u(\boldsymbol{\kappa}) = \left[ \frac{\hbar}{2Nm_b} \right]^{\frac{1}{2}} \sum_{\boldsymbol{\kappa}, \nu}^{N, 3n} [\omega(\boldsymbol{\kappa}) + \Delta(\boldsymbol{\kappa}) \pm i\Gamma(\boldsymbol{\kappa})]^{-\frac{1}{2}} \tilde{e}(\boldsymbol{\kappa} \mid \boldsymbol{\kappa}) \exp[i\boldsymbol{\kappa} \cdot \mathbf{r}_0^{(l)}] \left[ \tilde{A}_3(\boldsymbol{\kappa}) + \tilde{A}_3^*(\boldsymbol{\kappa}) \right]. \quad (\text{B.70})$$

Using Eq. (B.70) to express  $H_3$  and  $H_4$  in terms of the creation and annihilation operators eliminates the need to introduce  $\epsilon$ . From this more accurate analysis, one finds that

$$\epsilon = \Gamma(\boldsymbol{\kappa}) + \Gamma(\boldsymbol{\kappa}') + \Gamma(\boldsymbol{\kappa}'') , \quad (\text{B.71})$$

where the wave vectors and dispersion branches denote the three phonons involved in the interactions in Eqs. (B.63) and (B.64).

## APPENDIX C

### Boundary scattering in thin films

The effect of boundary scattering on phonon transport is discussed by Ziman [27] and Srivastava [46]. In developing a framework for analysis, they both assume isotropic phonon properties and that the phonon-phonon and phonon-boundary scattering mechanisms are independent [*i.e.*, they apply the Matthiesen rule, Eq. (4.4)]. Neither assumption is made in the following derivation.

Begin with the Boltzmann transport equation for an individual phonon mode,

$$\mathbf{v}_g \cdot \nabla f = \left. \frac{\partial f}{\partial t} \right|_{coll}, \quad (\text{C.1})$$

where the dependence on the wave vector and dispersion branch [*i.e.*,  $(\mathbf{g})$ ] is omitted for clarity. The total phonon distribution function,  $f$ , is

$$f = f_0 + \epsilon, \quad (\text{C.2})$$

where  $\epsilon$  is the deviation from the equilibrium distribution,  $f_0$ . The relaxation time approximation allows Eq. (C.1) to be written as

$$\left. \frac{\partial f}{\partial t} \right|_{coll} = \frac{f_0 - f}{\tau_{p-p}}. \quad (\text{C.3})$$

Combining Eqs. (C.1), (C.2), and (C.3) yields

$$v_{g,x} \frac{\partial T}{\partial x} \frac{\partial f_0}{\partial T} + v_{g,z} \frac{\partial \epsilon}{\partial z} = \frac{-\epsilon}{\tau_{p-p}}, \quad (\text{C.4})$$

where the temperature gradient is taken to be along the  $x$  direction and the boundaries are perpendicular to the  $z$  direction, as shown in Fig. 4.1. In deriving Eq. (C.4), one can set  $\partial f_0/\partial y = \partial f_0/\partial z = 0$  because there is no temperature variation in the  $y$  and  $z$  directions. It is possible to set  $\partial \epsilon/\partial y = 0$  due to the absence of boundaries along the  $y$ -direction. In addition, it is assumed that  $\partial \epsilon/\partial x$  is small in comparison to the other terms.

The solution to Eq. (C.4) is

$$\epsilon(z) = C \exp\left(-\frac{z}{v_{g,z}\tau_{p-p}}\right) - \frac{\tau_{p-p}}{\tau_0}, \quad (\text{C.5})$$

where  $C$  is a mode-dependent constant and

$$\tau_0 = \left[v_{g,x} \frac{\partial T}{\partial x} \frac{\partial f_0}{\partial T}\right]^{-1}. \quad (\text{C.6})$$

Phonons traveling toward a boundary are assumed to be either specularly reflected with probability  $p$  or scattered into the equilibrium distribution (*i.e.*,  $\epsilon = 0$ ) with probability  $1 - p$ . The boundary conditions take the form:

$$\epsilon^+(z = -L_z/2) = p\epsilon^-(z = -L_z/2) \quad (\text{C.7})$$

and

$$\epsilon^-(z = L_z/2) = p\epsilon^+(z = L_z/2), \quad (\text{C.8})$$

where the superscript  $+$  denotes a phonon traveling toward the top surface (located at  $z = L_z/2$ ) while the superscript  $-$  denotes a phonon traveling toward the bottom surface (at  $z = -L_z/2$ ). In Eqs. (C.7) and (C.8), the incident and reflected phonons are equivalent except that  $\kappa_z^+ = -\kappa_z^-$  and  $v_{g,z}^+ = -v_{g,z}^- = |v_{g,z}|$  (*i.e.*, the scattering event is elastic).

Applying the boundary conditions to Eq. (C.5) yields

$$\epsilon^\pm(z) = \exp\left(\frac{-L_z \mp 2z}{2|v_{g,z}|\tau_{p-p}}\right) \left[\frac{\tau_{p-p}}{\tau_0} + p\epsilon^\mp(\mp L_z/2)\right] - \frac{\tau_{p-p}}{\tau_0}. \quad (\text{C.9})$$



Successive elimination of  $\epsilon^-(-L_z/2)$  and  $\epsilon^+(L_z/2)$  gives

$$\epsilon^\pm(z) = \frac{\tau_{p-p}}{\tau_0} \exp\left(\frac{-L_z \mp 2z}{2|v_{g,z}|\tau_{p-p}}\right) \frac{1-p}{1-p\exp(-\delta)} - \frac{\tau_{p-p}}{\tau_0}, \quad (\text{C.10})$$

where  $\delta \equiv L_z/(|v_{g,z}|\tau_{p-p})$ . The heat flux in the  $x$  direction is

$$q_x = \sum_{\kappa,\nu} \left[ \frac{\hbar\omega}{V} \frac{v_{g,x}}{L_z} \int_{-L_z/2}^{L_z/2} \epsilon(z) dz \right] = - \sum_{\kappa,\nu} \frac{\hbar\omega}{V} v_{g,x} \frac{\tau_{p-p}}{\tau_0} F, \quad (\text{C.11})$$

where

$$F \equiv 1 - \frac{1-p}{\delta} \frac{1 - \exp(-\delta)}{1 - p\exp(-\delta)}. \quad (\text{C.12})$$

The thermal conductivity in the  $x$  direction is then

$$k = \frac{-q_x}{\partial T / \partial x} = \sum_{\kappa,\nu} c_{ph} v_{g,x}^2 \tau_{p-p} F. \quad (\text{C.13})$$

Fuchs [107] and Sondheimer [108] derived a similar expression for  $F$  using the Boltzmann transport equation applied to electrons under the isotropic approximation. Additional manipulations, beyond the derivation presented here, are required to incorporate the isotropic approximation. In this Author's opinion, the more general and simpler expression for  $F$ , presented here, is easier to interpret and implement.